

SPURREKONSTRUKTION IN VORWÄRTSRICHTUNG
MIT DEM SILIZIUM-VERTEXDETEKTOR DES
CDF-EXPERIMENTS IN RUN II

Zur Erlangung des akademischen Grades eines
DOKTORS DER NATURWISSENSCHAFTEN
von der Fakultät für Physik der
Universität Karlsruhe(TH)

genehmigte

Dissertation

von

Dipl. Phys. Thorsten Scheidle
aus Mosbach

Tag der mündlichen Prüfung: 16. Februar 2007

Referent: Prof. Dr. M. Feindt, Institut für Experimentelle Kernphysik

Korreferent: Prof. Dr. G. Quast, Institut für Experimentelle Kernphysik

Deutsche Zusammenfassung

Das Standardmodell der Teilchenphysik ist zur Zeit die Theorie, die die fundamentalen Teilchen der Materie und ihre Wechselwirkungen am besten beschreibt. Eine Möglichkeit, die Vorhersagen der Theorie zu überprüfen und ihre freien Parameter zu bestimmen, ist, Kollisionsexperimente an großen Teilchenbeschleunigern durchzuführen. Einige Teilchen können nur in Kollisionen mit sehr hoher Schwerpunktsenergie erzeugt werden, weswegen die Beschleunigerenergie immer weiter erhöht wird. Bis zur Inbetriebnahme des *Large Hadron Collider* (LHC) am CERN ist das *Tevatron* am Fermilab der Beschleuniger mit der höchsten Schwerpunktsenergie, $\sqrt{s} = 1.96$ TeV. Dort befinden sich die beiden Detektorsysteme CDF und DØ, welche um die Kollisionpunkte des Proton- und Antiproton-Strahls des Tevatrons aufgebaut sind.

Zu Beginn meiner Arbeit wurde für die meisten physikalischen Analysen bei CDF nur der zentrale Detektorteil genutzt. Die Spurrekonstruktion außerhalb dieses Bereiches, der sogenannte Vorwärtsbereich, war nicht sehr effizient, hat aber großes Potential, da in vielen Kollisionen die erzeugten Teilchen auch in diese Richtung fliegen.

Das Ziel meiner Arbeit war es, die Spurrekonstruktion zu verbessern und die Effizienz im Vorwärtsbereich so zu erhöhen, dass dieser Bereich für Physikanalysen verwendet werden kann.

Der CDF-Detektor ist aus vielen verschiedenen Sub-Detektoren aufgebaut, die spezifische Aufgaben erfüllen und deren Kombination die Messung von unterschiedlichen Eigenschaften der Teilchen ermöglicht.

Ein zentraler Teil ist die Spurrekonstruktion geladener Teilchen. Am CDF-Experiment wird das Spurrekonstruktionssystem von einem Silizium-Vertex-Detektor und einer Driftkammer gebildet. Das Volumen des Spurrekonstruktionssystems wird von einem starken homogenen Magnetfeld durchdrungen, welches die Teilchen ablenkt und auf eine Helixbahn zwingt. Durch die Wechselwirkung der geladenen Teilchen mit der Detektormaterie wird diese ionisiert, was durch sensitive Elektronik gemessen werden kann. Um eine Teilchenspur verfolgen zu können, ohne diese zu sehr zu beeinflussen, sollte die abgegebene Energiemenge der Teilchen bei jeder Materialionisation klein sein. Dies wird erreicht indem man dünne Schichten eines Halbleiterdetektors in unterschiedlichen Lagen oder eine mit Gas gefüllte, von dünnen Messdrähten durchzogene Spurkammer für

die Messung verwendet. Die Messungen in den einzelnen Schichten oder auf den einzelnen Drähten müssen erst zu einer Gesamtmessung der Spur kombiniert werden. Die Abstände der Messpunkte einer Spur können bis zu einigen Zentimetern betragen, wobei die Ortsauflösung des Messpunktes an sich bei einigen Mikrometern liegt. Da viele Teilchen gleichzeitig durch den Detektor fliegen, ist eine genaue Zuordnung der Messpunkte zu einer Spur schwierig, was die Spurrekonstruktion zu einer anspruchsvollen kombinatorischen Aufgabe macht. Ich habe mich in meiner Arbeit auf die Spurrekonstruktion im Silizium-Vertex-Detektor des CDF-Experimentes konzentriert, der eine hohe Ortsauflösung der Messpunkte bietet und insbesondere für die Rekonstruktion von Produktions- und Zerfallsvertices essentiell ist.

Die Region, die nicht mehr vom zylinderförmigen Teil des *zentralen* Detektors überdeckt wird, wird *Vorwärtsbereich* genannt, ohne zwischen Proton- und Antiprotonrichtung zu unterscheiden. Teilchen mit kleiner Masse werden vor allem in Strahlrichtung erzeugt. Aber auch Teilchen aus dem Zerfall schwerer zentral erzeugter Teilchen können vorwärts gerichtet sein. Zum Beispiel zeigt die Polarwinkelverteilung der Elektronen aus dem Z^0 -Boson-Zerfall am Tevatron ebensoviele Ereignisse im zentralen Teil des Detektors wie im Vorwärtsbereich. Daher ist eine effiziente Spurrekonstruktion in allen Bereichen des Detektors wichtig.

Die Driftkammer deckt den zentralen Bereich ab, der einen Winkel von $40^\circ < \theta < 140^\circ$ umfasst, wobei θ der Winkel bezüglich der Protonstrahlrichtung ist. Der Aufbau des Silizium-Vertex-Detektors sollte eine Spurrekonstruktion bis zu einem Winkel $15^\circ < \theta < 165^\circ$ ermöglichen. Eine Studie zu Beginn meiner Arbeit fand jedoch eine Spurrekonstruktionseffizienz von lediglich $\approx 10\%$ im Winkelbereich um 15° (165°). Aus diesem Grund wurde bis jetzt bei allen physikalischen Analysen, welche rekonstruierte Spuren voraussetzen, nur der zentrale Bereich berücksichtigt. Eine Erweiterung des bei einer Analyse verwendeten Akzeptanzbereiches erhöht die Sensitivität von Analysen, weswegen ich mein Hauptaugenmerk auf den Vorwärtsbereich gerichtet habe.

Die Spurrekonstruktion benutzt die Punktmessungen im Silizium-Vertex-Detektor, um die Flugbahn eines Teilchens zu bestimmen. Diese Messungen sind aber oft mit Signalen aus dem elektrischen Rauschen der Ausleseelektronik vermischt, weswegen nicht alle Messungen einem Teilchendurchgang durch die Messlage entsprechen.

Mein erster Schritt war eine Studie dieser Punktmessungen, um ein Kriterium für die Unterdrückung der Fehlmessungen zu erarbeiten. Es zeigten sich mehrere Effekte, die in zwei Kategorien eingeordnet werden können.

Die erste Kategorie beinhaltet Fehlmessungen auf Grund von fehlenden Messinformationen. In manchen Bereichen wird vom Detektor keine Information mehr geliefert, da ein Teil der Auslekette unterbrochen ist oder der Sensor an dieser

Stelle defekt ist. Somit ist die Abdeckung des Detektorbereichs nicht mehr in allen Messlagen vollständig, was bei der Spurrekonstruktion berücksichtigt werden muss. Hierzu habe ich einen neuen Algorithmus entwickelt, der Spuren anhand einer geringeren Anzahl an Messungen rekonstruieren kann, als die vorhandenen Strategien.

Die zweite Kategorie beinhaltet Signale aus dem Rauschen der Messelektronik. Um nicht jegliches Rauschen als Signal aufzunehmen, wird von der Ausleseelektronik ein Schwellenwert für die Messung gefordert. Dieser Schwellenwert wird dynamisch bestimmt und an manchen Stellen viel zu niedrig festgelegt, was zur Aufnahme von Ladungsfluktuationen als Signal führt. An einigen Stellen wird das über 100fache der normalen Messhäufigkeit erreicht, da diese Detektorstelle beinahe ständig Signale liefert. Eine Studie dieser Messungen zeigt, dass sie fast ausschließlich nur aus einem einzigen Auslestreifen bestehen. Zusätzlich sind diese Streifen in der Kalibration schon als rauschempfindlich erkannt worden und dementsprechend markiert. Durch die Selektion anhand des kombinierten Qualitätskriteriums beider Eigenschaften können 93,5% dieser Signale als Rauschen identifiziert werden. Die verbleibenden 6,5% beinhalten wahre Messungen eines Teilchendurchgangs und Rauschen, das aber wie im restlichen Detektor nicht mehr eindeutig von Teilchensignalen unterschieden werden kann. In manchen Fällen ist das Teilchensignal einem Rauschen überlagert, wodurch die Messung verfälscht wird.

Die Steigerung der Qualität und Reinheit der Messungen des Silizium-Vertex-Detektors wirkt sich positiv auf die Rekonstruktion der Spur aus.

Die Spurrekonstruktion am CDF-Experiment wird in mehreren Stufen durchgeführt. Zuerst werden die Spuren aus den Messungen in der Driftkammer rekonstruiert, da dort die Dichte der Messungen durch die große Distanz zum Kollisionspunkt am geringsten ist.

In der nächsten Stufe werden diese Spuren dann in den Silizium-Detektor extrapoliert, um dessen Messungen der Spur hinzuzufügen. Da der Algorithmus in der weiter außen liegenden Driftkammer beginnt und nach innen verläuft, wird er *Outside-In* genannt. Diese Strategie basiert auf Spuren der Driftkammer und kann somit nur im Zentralbereich des Detektors angewendet werden.

Als nächstes werden anhand des sogenannten *Silicon-StandAlone* Algorithmus aus den noch nicht verwendeten Messungen Spuren im Silizium-Detektor rekonstruiert. Meine Verbesserungen innerhalb des Algorithmus und das Einbeziehen der korrekten Strahlposition an den Kollisionspunkten führen zu einer Effizienzsteigerung von 150% im Winkelbereich um 15° (165°).

In den Winkelbereichen des Detektors, in denen nur wenige Messungen existieren, kann die *Silicon-StandAlone* Strategie nicht effektiv Spuren rekonstruieren, da hierzu mindestens zwei Messungen in allen drei Dimensionen gefunden werden müssen. Um die Lücken in der Abdeckung der Messlagen des Silizium-Detektors zu berücksichtigen, habe ich einen weiteren Algorithmus eingeführt, den sogenannten *Silicon-Forward* Algorithmus. Da diese Strategie nur eine dreidimensio-

nale Messung eines Teilchendurchgangs voraussetzt, können auch Spuren rekonstruiert werden, die nicht die Mindestanzahl von zwei dreidimensionalen Messungen des Silicon-StandAlone Algorithmus erfüllen. Diese Strategie wird im Silizium-Vertex-Detektor eingesetzt, um die Effizienz im Vorwärtsbereich zu erhöhen. Die Kombination der beiden letzten Strategien ermöglicht es 50% der Spuren im Winkelbereich um 15° (165°) zu rekonstruieren, was im Vergleich zum Beginn meiner Arbeit einer Steigerung von 400% entspricht.

Zuletzt werden noch die Spuren aus dem Silizium-Vertex-Detektor in die Driftkammer extrapoliert, um dort zusätzlich noch Messpunkte hinzuzufügen. Dieser Algorithmus kann aber nur im Abdeckungsbereich der Driftkammer angewendet werden und wird *Inside-Out* Strategie genannt.

Mit den neuen Strategien ist eine Spurrekonstruktion mit mindestens 50% Effizienz bis zu einem Winkel von $15^\circ < \theta < 165^\circ$ möglich.

Alle Strategien sind, wie sie in der Arbeit vorgestellt werden, in der offiziellen Rekonstruktionssoftware des CDF-Experimentes enthalten und werden im nächsten Rekonstruktionszyklus der Rohdaten verwendet.

Die Effizienzsteigerung der Spurrekonstruktion kann direkt im Zerfallskanal des Z^0 -Bosons nach e^+e^- und $\mu^+\mu^-$ gezeigt werden. Hierzu wird die Elektronenpaar¹- bzw. Myonpaar-Masse in Ereignissen rekonstruiert, in denen die beiden hoch energetischen Leptonen vom gleichen Vertex kommen und unterschiedlich geladen sind. Um meine neuen Strategien mit einzubeziehen, habe ich die Ereignisse aus den Datensätzen des CDF-Experimentes von Februar 2002 bis Februar 2006, welche einer integrierten Luminosität von 955 pb^{-1} entsprechen, neu rekonstruiert. Die Datenereignisse werden anhand eines zentralen Elektrons oder Myons selektiert und die Winkelverteilung des anderen Elektrons bzw. Myons studiert. Die Spuren der Elektronen bzw. Myonen werden von den unterschiedlichen Spurrekonstruktionsstrategien gefunden. Die Massenverteilung kann anhand der verwendeten Spurrekonstruktionsalgorithmen separiert werden, wobei $\approx 40\%$ der rekonstruierten Ereignisse mit Hilfe der neu entwickelten Strategien nachgewiesen wurden.

Die Elektronpaar-Massenverteilung zeigt ein Signal bei der Masse des Z^0 -Bosons von $91,19 \text{ GeV}/c^2$, was darauf hinweist, dass die Energie- und Impulsrekonstruktion der Elektronen stimmig ist. Die Elektronen werden anhand einer Spur und der Energie im elektromagnetischen Kalorimeter rekonstruiert, wobei die Energieauflösung von der Kalorimetrauflösung bestimmt wird, die in diesem Energiebereich gegenüber der Impulsauflösung der Spur dominiert. Daher sind in den Massenverteilungen, die anhand der Spurrekonstruktionsstrategien unterteilt wurden, die Massenaufösungen sehr ähnlich.

Die Rekonstruktion der Myonen benutzt keine Kalorimeter-Messungen. Die Auf-

¹Da bei hohen Energien Elektronen und Positronen bis auf die Ladung identische Eigenschaften haben, werden beide Teilchen als Elektron bezeichnet. Analog wird auch bei Myonen nicht zwischen μ^+ und μ^- unterschieden.

lösung der Myonpaar-Massenverteilung hängt deswegen vorwiegend von der transversalen Impulsaufösung σ_{p_t} der Spuren ab. Aufgrund ihrer Länge haben die Spuren der Outside-In Strategie die beste Auflösung mit $\sigma_{p_t}/p_t^2 \approx 0,15 \text{ \% (GeV/c)}^{-1}$. Die beiden Strategien, die nur Messungen des Silizium-Vertex-Detektors verwenden, haben aufgrund der um einiges kürzeren transversalen Spurlänge beide eine schlechtere Auflösung, Silicon-StandAlone mit $\sigma_{p_t}/p_t^2 \approx 0,4 \text{ \% (GeV/c)}^{-1}$ und Silicon-Forward mit $\sigma_{p_t}/p_t^2 \approx 0,5 \text{ \% (GeV/c)}^{-1}$. Diese unterschiedlichen Auflösungen machen sich in der unterschiedlichen Breite der Massenverteilung bemerkbar. Die Massenverteilung des Myonpaares zeigt auch hier ein Signal bei der Masse des Z^0 Bosons, wodurch wiederum bestätigt wird, dass die Impulsrekonstruktion der Spuren einen korrekten Wert ergibt.

Die neu eingeführten Qualitätskriterien für die Messungen des Silizium-Vertex-Detektors haben deren Reinheit erhöht, wovon alle Spurrekonstruktionsstrategien profitieren. Die beiden neuen Spurrekonstruktionsstrategien steigern die Effizienz im Vorwärtsbereich des Detektors wesentlich, teils um bis zu 400%. Hierdurch kann der zur Verfügung stehende Spurrekonstruktionsbereich vergrößert werden, wovon viele physikalische Analysen profitieren können, die Spurrinformationen benötigen. Beispielsweise hat eine Studie mit simulierten Ereignissen gezeigt, dass die Akzeptanz für $b\bar{b}$ -Paare durch die Hinzunahme des Vorwärtsbereiches deutlich gesteigert werden kann. Hierfür wurde ein zentral erzeugtes b -Quark verlangt, wobei in 40% der Ereignisse das andere b -Quark im Winkelbereich von $40^\circ < \theta < 140^\circ$ zu finden war. Das zweite Quark liegt bei 70% der simulierten Ereignisse in dem erweiterten Winkelbereich $15^\circ < \theta < 165^\circ$, der durch die neuen Algorithmen zugänglich wird. Dies entspricht fast einer Verdoppelung der rekonstruierten Ereignisse.

FORWARD TRACKING WITH THE SILICON VERTEX
DETECTOR AT THE CDF EXPERIMENT IN RUN II

Zur Erlangung des akademischen Grades eines
DOKTORS DER NATURWISSENSCHAFTEN
von der Fakultät für Physik der
Universität Karlsruhe(TH)

genehmigte

Dissertation

von

Dipl. Phys. Thorsten Scheidle
aus Mosbach

Tag der mündlichen Prüfung: 16. Februar 2007

Referent: Prof. Dr. M. Feindt, Institut für Experimentelle Kernphysik

Korreferent: Prof. Dr. G. Quast, Institut für Experimentelle Kernphysik

Contents

1	Introduction	3
1.1	Reconstruction of particle tracks	3
1.2	Electroweak theory of the Z^0 boson	7
1.3	Angular distribution of decay particles	9
2	The CDF Experiment	11
2.1	The Tevatron	12
2.1.1	Accelerator chain	13
2.1.2	Performance	13
2.2	The Collider Detector at Fermilab in RUN II	15
2.2.1	The tracking system	18
2.2.2	L00 sub-detector	19
2.2.3	SVX II sub-detector	20
2.2.4	ISL sub-detector	21
2.2.5	Drift chamber (COT)	21
2.2.6	Calorimeters	22
2.2.7	Muon chambers	23
2.3	Data acquisition and monitoring	23
2.3.1	Trigger	23
2.3.2	Online Monitoring	25
2.4	Software environment and track reconstruction packages	28
3	Measurements with the silicon detector	29
3.1	Basics of the measurements with a silicon sensor	29
3.1.1	Fundamentals of semiconductors	29

3.1.2	Silicon strip sensor	32
3.2	CDF silicon hardware overview	33
3.2.1	Silicon sensor module	33
3.2.2	Small Angle Stereo and Z90 layers	37
3.2.3	Position and identification of sensors	38
3.3	Reconstruction of hits	41
3.3.1	Silicon strips used in the hit reconstruction	42
3.3.2	Reconstruction of clusters	42
3.3.3	Reconstruction of hits	43
3.3.4	Determination of the global position of hits	46
3.4	Study of the hit quality	47
3.4.1	Comparison of hit quality between measured and simulated data	47
3.4.2	Study of the strip occupancy distributions	50
3.4.3	Reduction of fake hits	51
3.4.4	Determination of the CDF II silicon detector functionality	56
4	Track reconstruction	63
4.1	Basics of track reconstruction	64
4.1.1	Parametrization of a track	64
4.1.2	Track fitting	65
4.1.3	Material description	70
4.2	Tracking strategies	73
4.2.1	Outside In Tracking	75
4.2.2	Silicon StandAlone Tracking	77
4.2.3	Silicon Forward Tracking	80
4.2.4	Inside Out Tracking	83
4.3	Performance of the strategies	84
4.3.1	Combinatorics of the seed tracks	84
4.3.2	Time performance of the silicon tracking	87
4.3.3	Track reconstruction efficiency in the simulation	90
4.3.4	Summary	90

5	Performance of the Forward Tracking using CDF data	93
5.1	Used data samples	93
5.1.1	Event selection	96
5.1.2	Electron data sample	96
5.1.3	Muon data sample	99
5.2	Efficiency of forward tracking	101
5.2.1	Phoenix Electrons	101
5.2.2	Track reconstruction efficiency in di-electron events . . .	101
5.3	Reconstruction of leptonic Z^0 boson decays	103
5.3.1	Z^0 boson decay into electrons	105
5.3.2	Z^0 boson decay into muons	109
5.4	Summary	113
6	Conclusion	115
A	Silicon hits	117
A.1	Studies of silicon hits and strips	117
A.2	Map of working halfadders	122
B	Fit layers	128
C	SiPatternRecModule tcl-switches	131
	Bibliography	135

List of Figures

1.1	Event display of the tracking system	5
1.2	Efficiency of track reconstruction in forward direction	6
1.3	Feynman diagram of Z^0 boson decay into leptons	8
1.4	Angular distribution of Z^0 boson decays into electrons	8
1.5	Fraction of $b\bar{b}$ events in forward direction	9
1.6	η distribution of the lepton in the process $q\bar{q} \rightarrow HW \rightarrow b\bar{b}l\nu$	10
2.1	Aerial shot of the Fermilab	11
2.2	Fermilab accelerator complex for RUN II	12
2.3	Peak luminosity per store	14
2.4	Integrated luminosity	14
2.5	Isometric view of CDF detector in RUN II	15
2.6	Definition of the coordinate system at CDF II	16
2.7	Elevation view of one half of the CDF II detector	17
2.8	Longitudinal view of one quarter of the CDF II tracking system	18
2.9	Picture of the mounted L00	19
2.10	Schematic plan view of L00	19
2.11	Resolution of d_0 in L00	19
2.12	Picture of SVX II	20
2.13	Schematic plan view of SVX II	20
2.14	Picture of the ISL	21
2.15	Schematic view of the ISL	21
2.16	Block diagram of the CDF II data flow	24
2.17	Block diagram of the CDF hardware trigger system	26
2.18	Overall design of the consumer framework	27
3.1	Schematic view of a pn-junction	31

3.2	Graph of the Bethe-Bloch formula	31
3.3	Schematic view of a silicon strip sensor	32
3.4	Picture of a silicon module	34
3.5	Readout chip SVX3D	35
3.6	Readout electronic in LAYER 1	35
3.7	Multiplexing in LAYER 2	36
3.8	Zigzag bonding of the 3 silicon wafers in LAYER 7	36
3.9	Z90 layer	37
3.10	SAS layer	37
3.11	Transverse cross view of L00 and SVX II	38
3.12	Longitudinal view of the barrel structure	38
3.13	Silicon cluster reconstruction	43
3.14	Clusters of two particles with overlapping charge deposit	43
3.15	Definition of the geometrical parameters on a halfadder	46
3.16	Fraction of 3D-Hits per halfadder	48
3.17	Fraction of 3D-Hits added to tracks per halfadder	49
3.18	Occupancy of sensor (layer 3, bulkhead 5, wedge 2, side p)	50
3.19	Comparison of the occupancy of sensor (layer 7, bulkhead 0, wedge 4)	52
3.20	Correction shown by the occupancy of sensor (layer 6, bulkhead 2, wedge 16, side p)	53
3.21	Calibration data of sensor (layer 6, bulkhead 2, wedge 16, side p)	54
3.22	Occupancy of sensor (layer 3, bulkhead 0, wedge 7, side p)	56
3.23	Occupancy of sensor (layer 7, bulkhead 1, wedge 25, side n)	57
3.24	Simulation with working 3D sensors in SASlayers	58
3.25	Map of working 3D sensors in SAS layers	59
3.26	ISL cooling lines blocked with glue	61
3.27	Broken bond of z/stereo wires	61
4.1	Illustration of a piecewise particle helix in material	64
4.2	Perigee parametrization of a track	66
4.3	Beam offset in x-y and r-z plane	67
4.4	Local parametrization of a track	70
4.5	Kalman Fitter: Forward Fit	71

4.6	Kalman Fitter: Backward Fit	71
4.7	Schematic view of the SiliMap material description	72
4.8	Hit search along a reference trajectory	76
4.9	Construction of the reference trajectory in $r\phi$ by SISA	79
4.10	Construction of the reference trajectory in rz by SISA	79
4.11	Construction of the reference trajectory in rz by FWD	82
4.12	Number of tracks and seed candidates per event of the silicon-only tracking	86
4.13	CPU time for silicon-only tracking	88
4.14	Tracking efficiency of simulated data	91
5.1	Schematic view of the phoenix electron reconstruction	102
5.2	Track efficiency of electrons in forward direction	104
5.3	Di-electron mass distribution for each tracking strategy	106
5.4	Di-electron mass distribution	107
5.5	η distribution of the reconstructed di-electron mass	108
5.6	Di-muon mass distribution for each tracking strategy	110
5.7	Di-muon mass distribution	111
5.8	η distribution of the reconstructed di-muon mass	112
A.1	Occupancy of the sensors on p side in LAYER 0 - LAYER 3	118
A.2	Occupancy of the sensors on p side in LAYER 4 - LAYER 7	119
A.3	Occupancy of the sensors on n side in LAYER 0 - LAYER 3	120
A.4	Occupancy of the sensors on n side in LAYER 4 - LAYER 7	121
A.5	Map of working ϕ sides in Z90 layers	123
A.6	Map of working stereo sides in Z90 layers	124
A.7	Map of working ϕ sides in SAS layers	125
A.8	Map of working stereo sides in SAS layers	126
A.9	Map of working 3D sensors in SAS layers	127

List of Tables

1.1	Electroweak properties of the fundamental particles	7
2.1	Overview of the CDF calorimeter properties and segmentation .	22
2.2	Design parameters of the CDF II muon detectors	23
3.1	Overview of the silicon layers	39
3.2	Mechanical dimensions of the silicon detector	40
3.3	Resolution of silicon hits and strips depending on the layer . . .	44
3.4	Distribution of hitsize in simulated data	45
3.5	Distribution of hitsize in data	45
3.6	Distribution of hitsize in corrected data	55
3.7	Distribution of hitsize on tracks	55
4.1	Average number of tracks and seed candidates of the silicon-only strategies	85
4.2	CPU time consumption of the silicon-only strategies	89
4.3	CPU time consumption per event	89
5.1	Used data samples with corresponding run range	95
5.2	The baseline cuts for central electrons	98
5.3	The baseline cuts for plug electrons	99
5.4	The baseline cuts for central muons	100
5.5	The baseline cuts for forward muons	100
5.6	Fit results of the di-lepton mass	113
B.1	Fit layers	130

Preface

The Standard Model of particle physics describes the fundamental particles of matter and their interactions. In order to test the Standard Model, determine free parameters and search for new particles beyond the Standard Model, large accelerator complexes produce particle collisions which are recorded by large detectors. Until the start of the Large Hadron Collider at CERN, the Tevatron accelerator at Fermilab provides particle collisions with the highest center-of-mass energy of $\sqrt{s} = 1.96$ TeV. The two multipurpose detector systems CDF and DØ record the collisions.

A multipurpose detector system is built of several specialized sub-detectors to measure different particle properties. A particle which passes the detector deposits energy by interacting with the detector material. A silicon strip detector and a wire drift chamber detect charged particles close to the collision point. The energy loss in these systems is relatively small, instead many different small energy depositions are produced by one passing particle. These so-called hits can be combined to a track, indicating the path of the particle. A homogeneous magnetic field surrounding the tracking system forces a charged particle to a helix path which allows a momentum measurement by measuring the curvature. The reconstruction of particle tracks is a non-trivial task. First all position measurements belonging to a particle along a hypothetical helix have to be found and then all position information has to be combined to a reconstructed track and its parameters.

I focused my work on the track reconstruction in the silicon detector which provides a good position resolution of the measurements. Combined with the position of the silicon detector next to the beam, the resolution of the tracks enables a good vertex reconstruction and constitutes the basis for lifetime and particle-antiparticle oscillation measurements as well as *b*-jet-tagging.

The particles generated in collisions at hadron colliders are usually boosted into the beam direction. Therefore an efficient track reconstruction in the forward region is a prerequisite for many physics analyses. When I started my work at CDF all track-based analyses only used the central part of the detector due to a highly efficient track reconstruction in that region. In forward direction

the existing algorithm was not efficient. The aim of my work was to utilize the entire detector range designed for track reconstruction. From an improvement in track reconstruction and an increase of the usable detector range all track-based analyses will benefit.

The measurements in the silicon detector are the basis for the track reconstruction of my thesis. For a better understanding of the silicon detector, a detailed description of the hardware properties is given in chapter 3. The positions of a passing particle, the so-called hits, have to be reconstructed from the signals of the detector before they can be used. To ensure a high reconstruction efficiency with a good quality of the measurements, I have studied the hit properties and their distribution in the detector. A result of my studies is the development of selection criteria for good quality hits. In order to improve the track reconstruction which bases on the hits, electronic and other noise have to be suppressed.

The track reconstruction in the silicon detector is performed in several strategies with different tasks. In chapter 4, I present my improved Silicon StandAlone strategy and my newly developed Silicon Forward strategy. Both algorithms reconstruct tracks from silicon measurements only and provide a track reconstruction into the forward direction of the detector. In order to be used in the official offline reconstruction software of CDF II, the strategies have to be optimized in efficiency and run-time consumption. The performance of the strategies is validated in studies with several different data sets.

In the last chapter I applied these new tracking strategies to Z^0 boson searches in the di-electron and di-muon decay channel. The di-electron events are used to calculate the track reconstruction efficiency in forward direction on measured data at CDF II. The increase in the number of reconstructed $Z^0 \rightarrow e^+e^-$ and $Z^0 \rightarrow \mu^+\mu^-$ events illustrates the gain for the track-based physics analyses.

Chapter 1

Introduction

The electronic signals provided by a multipurpose detector like CDF II have to be combined and interpreted in a reconstruction program in order to obtain information about the physical parameters of particles produced in a given event. Each detector component has its own task and therefore different properties of a particle can be determined. One of the fundamental objects which are reconstructed is the track of a particle in the detector. Track reconstruction is also simply called *tracking*.

1.1 Reconstruction of particle tracks

The track parameter of a particle provides information about its properties. Usually a magnetic field saturates the tracking volume and therefore the track of a charged particle is bent to a helix. The curvature of the helix depends on the transverse momentum of the particle with respect to the magnetic field direction \vec{B} .

A track of a charged particle is measured by the readout electronics of the tracking detectors. However the track information is not provided as a continuous measurement of a trajectory. Only single interaction positions of the charged particle with the detector material can be measured. Such a signal of an interaction position is called *hit*. All position information belonging to one particle track has to be detected, identified and selected from all other measurements. The resolution of the position measurement of a silicon strip detector is of the order of μm and the distance between two measurements of one particle is of the order of cm. Therefore finding the next measurement along a particle track is a non-trivial task due to the missing connection between the hits. The position measurements along a hypothetical helix have to be found and separated from other signals observed in the detector either from other tracks or electronic noise. Because of the task of hit selection in the silicon detector, the track reconstruction is also called *Silicon Pattern Recognition*.

In figures 1.2 a), c) and e) examples of the CDF II event display with the position measurements in the drift chamber and the silicon detector are shown. The large number of hits clarifies the non-trivial task of the combination of these single measurements to a track. Figures 1.2 b), d) and f) show the same event with the reconstructed tracks.

In order to provide the track parameters, position measurements have to be fitted to a reference helix. The fit algorithm has to match the requirements of the tracking strategy.

The process of track reconstruction starts with the measurements of the tracking detectors and in the end provides a list of tracks with their parameters including references to the hits.

The events at hadron colliders can be boosted into beam direction. Therefore the momentum and energy distribution in the transverse plane (p_t, E_t) are usually used to specify the properties of the particles in the detector. The rapidity (y) is a non-linear transformation of the longitudinal particle motion:

$$y = \frac{1}{2} \ln \left(\frac{E + p_z}{E - p_z} \right),$$

where E is the energy of the particle and p_z the momentum in beam direction. In the Taylor expansion of the term, higher orders of m/p can be neglected for particles with a low mass ($m \ll p$):

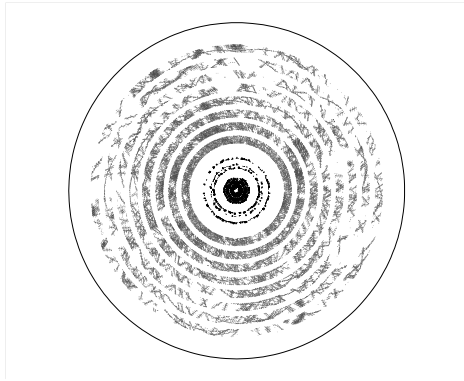
$$\begin{aligned} y &= \frac{1}{2} \ln \left(\frac{\cos^2 \theta/2 + m^2/4p^2 + \dots}{\sin^2 \theta/2 + m^2/4p^2 + \dots} \right) \\ &\approx -\ln \tan \theta/2 =: \eta, \end{aligned}$$

where θ is the polar angle between the particle and the beam axis ($\cos \theta = p_z/p$). η is called pseudorapidity. Because the particle density is uniformly distributed in η it is commonly used at hadron colliders instead of the polar angle θ .

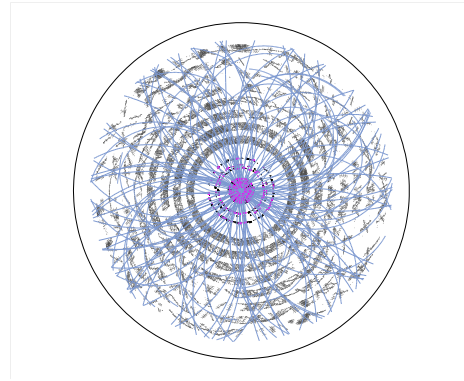
The barrel structure of the central part of the CDF II detector covers the range $|\eta| < 1.0$ which corresponds to a polar angle $40^\circ < \theta < 140^\circ$. In this thesis that range will be called *central* and particles with $|\eta| > 1.0$ are in the *forward* range. The track reconstruction in the central region has an efficiency larger than 90%. The silicon detector was designed to enable tracking with an efficiency of over 90% up to $|\eta| < 2.0$, see figure 1.2 a). When I started my work the existing track reconstruction strategies could not provide this expected design efficiency, which can be seen in figure 1.2 b). Only 10% of the measured electrons in the calorimeter at $|\eta| = 2.0$ could be matched with a reconstructed track. There was a large potential for improvement of the track reconstruction. This thesis presents the significant improvement which was achieved by both modifying the existing algorithms and implementing a new tracking strategy.

The track reconstruction efficiency in figure 1.2 b) was studied on measured data. A clear event signature was required to define the tracks of the event

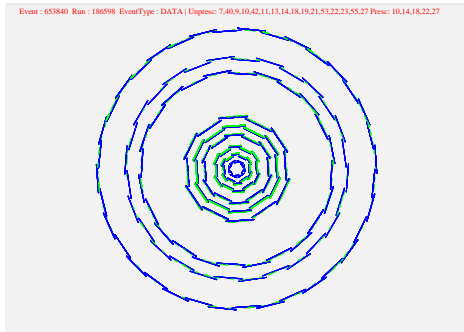
1.1. RECONSTRUCTION OF PARTICLE TRACKS



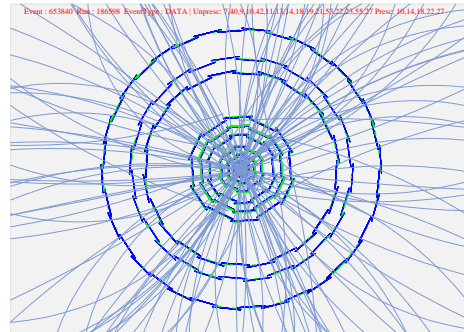
a) measurements in the drift chamber



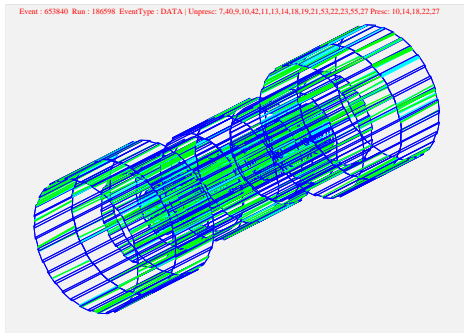
b) drift chamber with reconstructed tracks



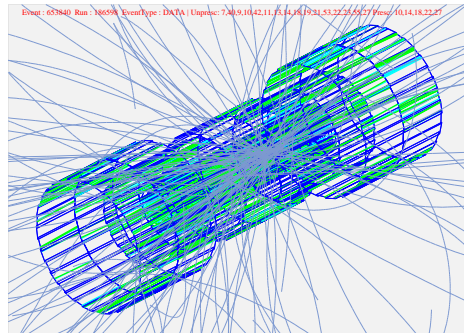
c) measurements in the silicon detector



d) silicon detector with reconstructed tracks



e) diagonal view of the measurements in the silicon detector



f) diagonal view of the silicon detector with reconstructed tracks

Figure 1.1: The event display shows the measurements of the event 653840 in run 186598 taken with the CDF II detector. In a) the measurements of the drift chamber and in c) and e) the measurements of the silicon detector are shown. The tracking uses the position measurements to reconstruct the particle trajectories. In this typical event with the large amount of possible combinations of measurements, the track reconstruction is obviously a non-trivial task. In the event display b), d) and f) the result of the track reconstruction is illustrated.

which have to be reconstructed by the tracking strategies. The selected events require at least two high-momentum electrons of opposite charge. One electron in the central region triggers the event and the second electron in the forward region is reconstructed by calorimeter information. If a track of the tracking strategies can be matched to a calorimeter measurement in the forward direction, this track is defined as a found electron-track. The ratio of the number of those tracks to the number of all calorimeter measurements determines the efficiency of the tracking.

The track reconstruction strategies can be studied well by investigating the Z^0 boson, the neutral interaction particle of the electroweak theory. The properties of the Z^0 boson are well known and many precise analyses have measured its mass and branching ratios. The final state of the leptonic Z^0 boson decay is a dilepton event which is also the signature of the events used for the determination of the tracking efficiency. Therefore the invariant mass of both electrons have to be consistent within the mass window of the Z^0 boson [$70 \text{ GeV}/c^2, 110 \text{ GeV}/c^2$]. The clear signature of the Z^0 boson decay into e^+e^- and $\mu^+\mu^-$ will also be used in this thesis to determine the tracking efficiency in forward direction. Therefore a short overview of the electroweak theory and the Z^0 boson is given.

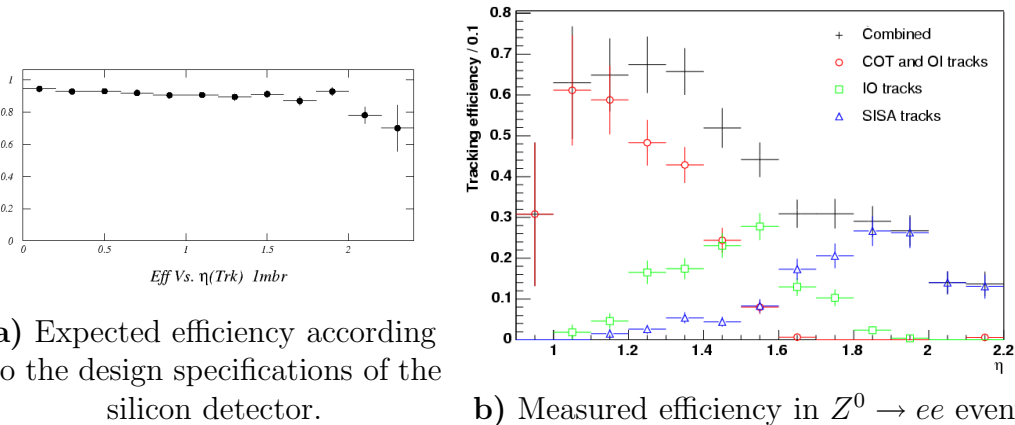


Figure 1.2: Efficiency of track reconstruction in forward direction. The plot a) was the expected efficiency of the technical design report for the CDF II experiment. In b) the measured efficiency is shown before the improvements of this work are applied.

1.2 Electroweak theory of the Z^0 boson

The *Standard Model* (SM) of the electroweak interaction, developed by Glashow, Weinberg and Salam is a combination of the electromagnetic and weak interaction to a single interaction with $SU(2) \times U(1)$ gauge symmetry. The fundamental particles of the Standard Model are the quarks and leptons. Leptons interact only electroweakly while quarks also interact strongly, as described by Quantum ChromoDynamics (QCD). In the electroweak theory, the particles are arranged in left-handed doublets (L) and right-handed singlets (R) and can be ordered by mass into three families.

The interactions are mediated by gauge bosons with the triplet of eigenstates W^i ($i = 1,2,3$) of $SU(2)$ and the singlet eigenstate B of $U(1)$. The triplet \mathbf{W} couples to the weak isospin T_3 and B couples to the weak hypercharge Y . In Table 1.1 the fundamental particles and their properties are listed.

	fermion family			T_3	Y	Q	C
	I	II	III				
leptons	$\begin{pmatrix} \nu_e \\ e \end{pmatrix}_L$	$\begin{pmatrix} \nu_\mu \\ \mu \end{pmatrix}_L$	$\begin{pmatrix} \nu_\tau \\ \tau \end{pmatrix}_L$	$+\frac{1}{2}$	$-\frac{1}{2}$	0	0
	e_R	μ_R	τ_R	$-\frac{1}{2}$	$-\frac{1}{2}$	-1	0
				0	-1	-1	0
quarks	$\begin{pmatrix} u \\ d' \end{pmatrix}_L$	$\begin{pmatrix} c \\ s' \end{pmatrix}_L$	$\begin{pmatrix} t \\ b' \end{pmatrix}_L$	$+\frac{1}{2}$	$+\frac{1}{6}$	$+\frac{2}{3}$	r,g,b
				$-\frac{1}{2}$	$+\frac{1}{6}$	$-\frac{1}{3}$	r,g,b
	u_R	c_R	t_R	0	$+\frac{2}{3}$	$+\frac{2}{3}$	r,g,b
	d_R	s_R	b_R	0	$-\frac{1}{3}$	$-\frac{1}{3}$	r,g,b

Table 1.1: The structure and the properties of leptons and quarks in the Standard Model are visualized by their quantum numbers T_3 and Y . The indices L and R denote left-handed and right-handed fermions. The prime at the left handed down-type quarks indicates that they are mixtures of the different quark mass eigenstates. The color C is an additional quantum number for quarks and can be one of the arbitrarily chosen colors red, green and blue.

The observable bosons are a mixture of \mathbf{W} and B and can be described as:

$$\begin{aligned}
 \text{massive charged fields : } W^\pm &= (W^1 \mp iW^2)/\sqrt{2} \\
 \text{massive neutral fields : } Z^0 &= -B \sin \theta_W + W^3 \cos \theta_W \\
 \text{massless photon : } A &= B \cos \theta_W + W^3 \sin \theta_W
 \end{aligned}$$

where θ_W is the Weinberg mixing angle. The gauge bosons couple to the fermions via a *vector* and an *axial-vector* coupling.

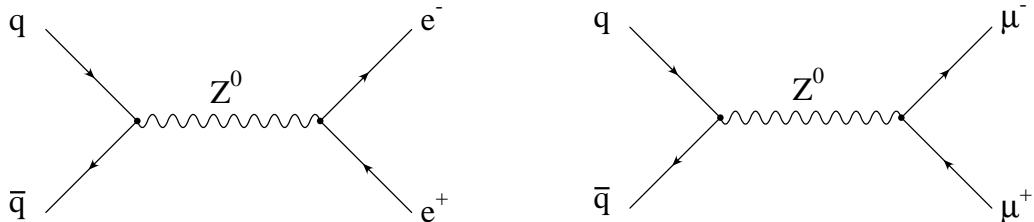


Figure 1.3: Feynman diagrams of $q\bar{q} \rightarrow Z^0 \rightarrow e^+e^-$ or $\mu^+\mu^-$, produced at hadron colliders, decaying into electrons and muons. The characteristics of these decays are two high- p_t leptons of opposite charge.

The massive neutral boson of the electroweak interaction is the Z^0 boson with a mass of (91.1876 ± 0.0021) GeV/ c^2 [1]. At the Tevatron it can be produced by $q\bar{q}$ annihilation. The Z^0 boson decays to leptons of all three families with the same probability. However only the electron and muon decay channel have a clear signature in the detector compared to the final state consisting of taus. The signatures of di-electron or di-muon events provide a clear criterion for the selection of Z^0 boson candidates which can be identified as a resonance in the invariant e^+e^- or $\mu^+\mu^-$ mass spectrum. The Feynman graphs of these two processes in leading order are shown in figure 1.3.

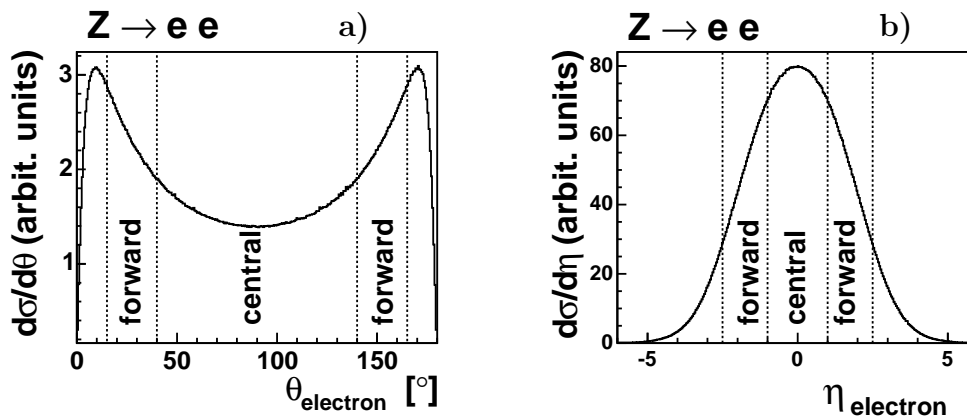


Figure 1.4: The angular distribution of Z^0 boson decays into electrons as simulated with the compHEP program [2]. The production mechanism of the Z^0 boson was set to proton-antiproton collisions with a center-of-mass energy of 1.96 TeV to simulate the conditions of the CDF II experiment at the Tevatron accelerator. The angular distribution of the electrons in a) shows approximately the same number of electrons in forward direction as in the central region. In b) the same events are shown as a distribution of η .

1.3 Angular distribution of decay particles

A calculation of the production cross section of the Z^0 boson is used to simulate the distribution of the polar angular of the final state electrons. In figure 1.4 a) the θ distribution shows the boost of the final state electrons in forward direction. In figure 1.4 b) the same distribution is presented as a function of η . In both figures the definition of central and forward region are displayed.

The central region contains approximately the same number of simulated events as the forward region, which covers the possible tracking range up to $|\eta| = 2.5$. Therefore an improvement of the efficiency of the tracking strategies in the forward region will increase the number of reconstructible decay particles considerably.

The Z^0 boson decay is not the only example of a decay process which will benefit from an improvement of the forward tracking. The result of a study of the angular distribution of the $b\bar{b}$ pair production at CDF II [3] is shown in figure 1.5. A central b -quark can be combined with a second b -quark which passes the η cut. The number of those events compared to the number of all $b\bar{b}$ events is used to estimate the increase of the number of reconstructible $b\bar{b}$ events. Only 40% of all simulated events are within a range $|\eta| < 1$. If one b -quark could be reconstructed in the range up to $|\eta| < 2$ over 70% of the simulated events would pass the cuts.

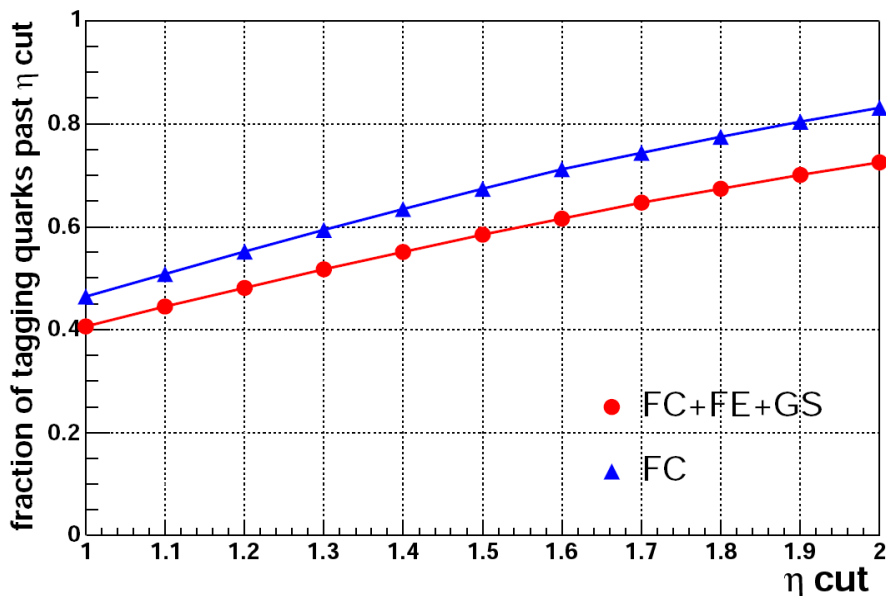


Figure 1.5: Fraction of the simulated $b\bar{b}$ events with a central b -quark and a second b -quark passing the η cut on the x-axis. The two graphs are for different simulation models. [3]

The event reconstruction of all processes with decay particles in forward direction can be improved by a higher track reconstruction efficiency. In figure 1.6 the η distribution of the lepton in the simulated $q\bar{q} \rightarrow HW \rightarrow b\bar{b}l\nu$ process is shown. The electrons in the forward region are reconstructed by calorimeter information which is not possible for a muon. Forward muons can only be reconstructed from tracks. An improvement in the forward track reconstruction will also increase the number of muons and therefore the sensitivity to a Higgs signal.

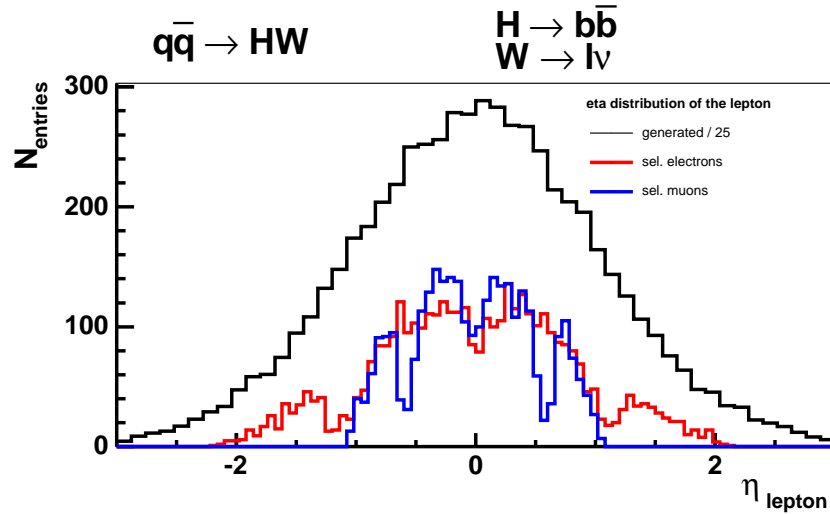


Figure 1.6: η distribution of the lepton in $q\bar{q} \rightarrow HW \rightarrow b\bar{b}l\nu$. The black graph is the generated η distribution of the leptons from the W decay, which is scaled by a factor 0.04. The red (blue) distribution shows the selected electrons (muons) after the reconstruction. In the electron channel the forward region can be reconstructed from calorimeter information. The muon reconstruction in forward direction depends solely on tracks, and thus can not be reconstructed with the old tracking strategies.

Chapter 2

The CDF Experiment

The experimental setup of the accelerator chain of the proton-antiproton collider *Tevatron* at the Fermi National Accelerator Laboratory (Fermilab or FNAL) and the CDF experiment (*Collider Detector at Fermilab*) are described in this chapter. Fermilab is located in Batavia approximately 60 km west of Chicago, Illinois, USA. More than 2,500 scientists from 25 countries use Fermilab's facilities to carry out research in particle physics. In figure 2.1 an aerial shot of the Fermilab is shown.

An overview of the several detector components are presented in this chapter. A detailed description of the different sub-detectors of CDF II and the RUN II physics program are summarized in the CDF II Technical Design Report [4].



Figure 2.1: Aerial shot of the Fermilab. The gray circle in front is the outer maintenance road of the Main Injector, the rear circle is the inner maintenance road of the Tevatron.

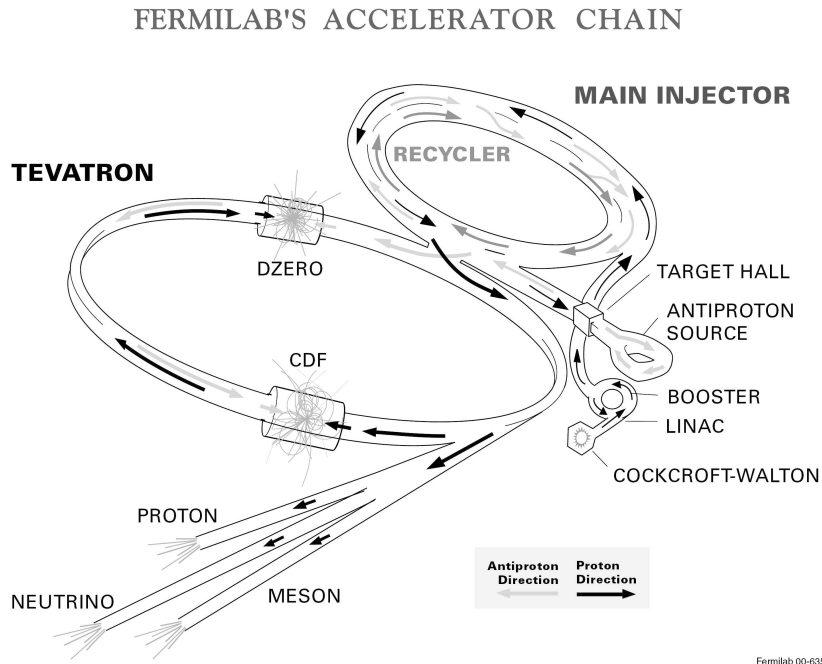


Figure 2.2: Fermilab accelerator complex for RUN II .

2.1 The Tevatron

The Tevatron accelerator is a symmetric proton and antiproton collider ring at Fermilab. First $p\bar{p}$ -collisions have been detected in 1985. This phase of operation was called RUN I and lasted until 1996 at a center-of-mass energy of $\sqrt{s} = 1.8$ TeV. Some of the physics highlights of the analyses of the data taken during that time are the first experimental top quark evidence provided by CDF [5] and a high accuracy measurement of its mass $m_t = 176.1 \pm 6.6$ GeV/ c^2 [6], precision electroweak measurements as for example the mass of the W boson $m_W = 80.433 \pm 0.079$ GeV/ c^2 [7] and the determination of the average lifetime for several B mesons [8].

The second phase of Tevatron, the ongoing RUN II, started in 2001 with an upgraded accelerator. The pursuing physics goals of the RUN II are the measurement of the $B_s^0 \bar{B}_s^0$ oscillation, discovery of the Higgs boson and Top-quark physics. Tevatron is now running at a center-of-mass energy of $\sqrt{s} = 1.96$ TeV and with a higher instantaneous luminosity than in RUN I. The *instantaneous luminosity* L is the product of the incident beam flux and the mean target density. The number of events of certain processes is calculated by $n = \sigma \int L dt$, where σ is the production cross section of the selected process at the given center-of-mass energy for proton-antiproton collisions. The *time-integrated luminosity* $\mathcal{L} = \int L dt$ is often called simply *luminosity*.

2.1.1 Accelerator chain

To accelerate the protons and antiprotons to their energy of 980 GeV a chain of several pre-accelerators is needed. Figure 2.2 gives a schematic view of this chain.

The first stage of acceleration is the *Cockcroft-Walton* pre-accelerator. Negatively charged hydrogen ions are produced with an energy of 750 keV and transferred into a 150 m long linear accelerator *Linac* which accelerates the ions to 400 MeV. In the next step, a carbon foil strips off the electrons and the protons enter the *Booster*. This is a synchrotron with a diameter of about 150 m in which protons are accelerated to 8 GeV. The last acceleration before the protons enter the Tevatron is taking place in the *Main Injector*.

The Main Injector is used for several tasks. Beside the acceleration of protons to 150 GeV, the energy of other protons are increased to 120 GeV in order to create antiprotons by collisions with a nickel target. Only in 2 of 10^5 collisions an antiproton can be acquired and is sped up to the same energy of 150 GeV by the Main Injector. As its name predicates the Main Injector also injects the protons and antiprotons into the Tevatron.

The final acceleration is achieved by the Tevatron, a collider with a circumference of about 6 kilometers. There, the protons and antiprotons obtain their final energy of 980 GeV each, which leads to the a center-of-mass energy for the two beams of 1.96 TeV. Further information of the accelerator properties and the design goals for RUN II are given in [9, 10].

2.1.2 Performance

The antiproton production is the new main limiting factor of the Tevatron-luminosity. The *Recycler* was installed in the Main Injector tunnel with the purpose to reuse the antiprotons from former collider cycles. This plan has been abandoned and today the Recycler is used for stacking and cooling of fresh antiprotons. Since July 2005 electron cooling of the antiprotons is performed, resulting a higher luminosity. The major limitations are identified and solved and the instantaneous luminosity is steadily increasing. The design goal up to $\mathcal{L} = 18 \cdot 10^{31} \text{ cm}^{-2} \text{ sec}$ [4] could be delivered by the Tevatron at the beginning of 2006. Figure 2.3 presents the instantaneous peak luminosities for RUN II since 2001. The integrated luminosity, recorded on tape, is around 1.8 fb^{-1} . Figure 2.4 displays the increase of the integrated luminosity delivered by the Tevatron and stored to tape at CDF since the start of RUN II.

2.1. THE TEVATRON

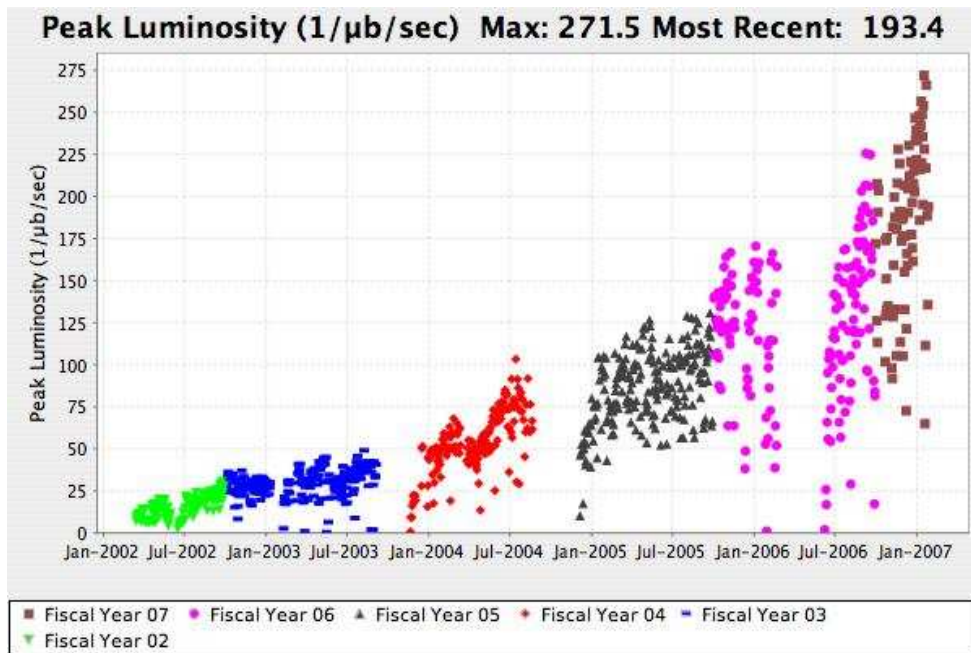


Figure 2.3: Instantaneous peak luminosity per store in $[\text{cm}^{-2}\text{s}^{-1}]$ since the start of RUN II [11].

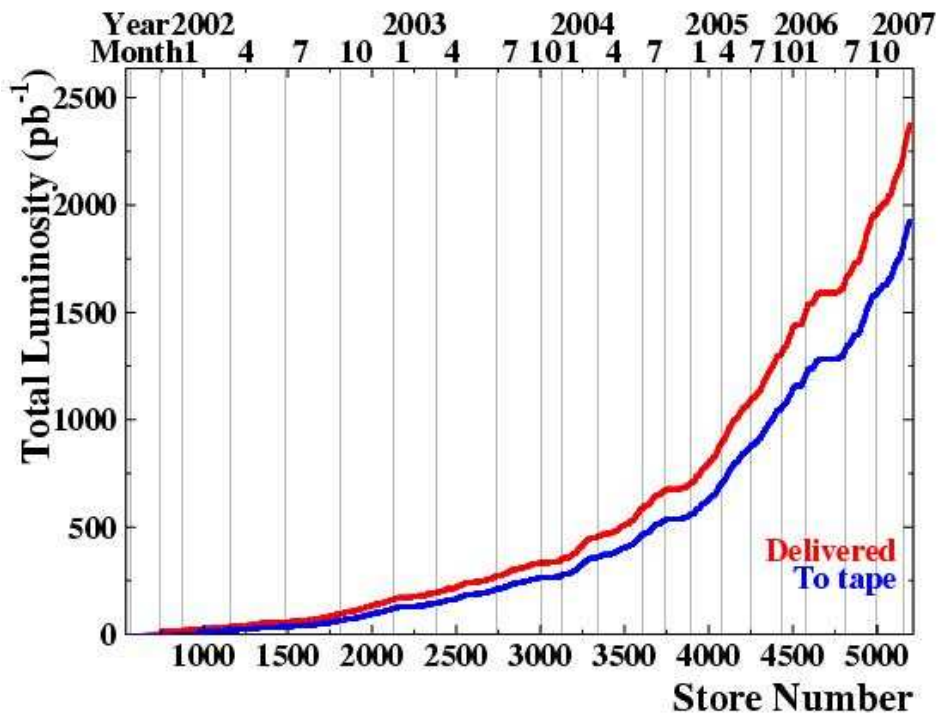


Figure 2.4: Delivered (upper red curve) and recorded (lower blue curve) integrated luminosity since the start of RUN II . The recorded luminosity is lower due to the detector dead time [12].

2.2 The Collider Detector at Fermilab in RUN II

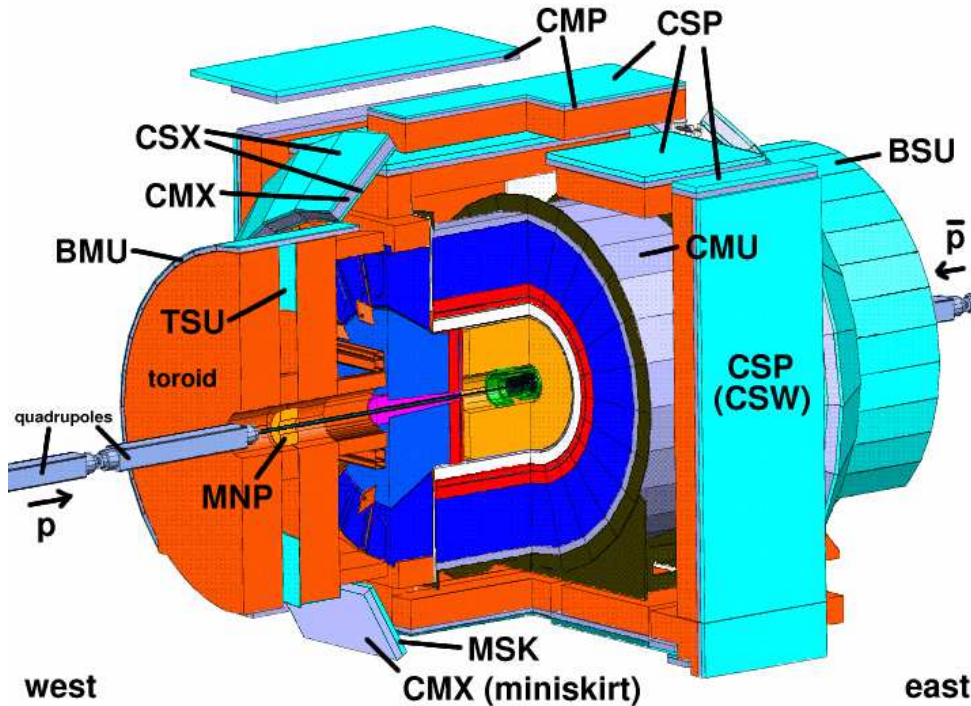


Figure 2.5: Isometric view of CDF detector in RUN II with the abbreviations of the different components of the muon system. The inner green and orange part represents the tracking system and the blue part the calorimeters.

The CDF experiment is a general multipurpose detector with the goal to track charged particles and measure the momentum and energy of charged and neutral particles.

The detector is built and maintained by a collaboration of more than 50 institutions from eleven countries. The only German institute within the collaboration is the *Institut für Experimentelle Kernphysik* at the University of Karlsruhe.

The detector has both azimuthal and forward-backward symmetry. The central region is arranged cylindrically around the interaction point. In the forward region, the detector components are arranged perpendicular to the beam orbit. Figure 2.5 shows an isometric view of CDF II and in figure 2.6 the CDF coordinate system is described.

Throughout this thesis longitudinal means parallel to the proton beam and transverse means perpendicular to the proton beam.

Global coordinate system:

- the proton beam defines the z axis, pointing east at the location of the CDF detector
- x is defined by the Tevatron radius, pointing outward
- y is defined to form a right-handed coordinate system, pointing upward

CDF II is using the following cylindrical coordinate system:

- the radius r is relative to the center of the beampipe
- the azimuthal angle ϕ is defined relative to the x axis
- z

Additional coordinate definitions

- the polar angle θ is relative to the z axis
- pseudorapidity: $\eta = -\ln(\tan\frac{\theta}{2})$

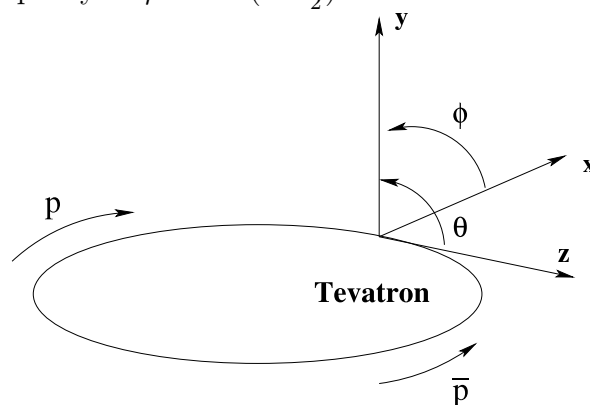


Figure 2.6: Definition of the coordinate system at CDF II.

2.2. THE COLLIDER DETECTOR AT FERMILAB IN RUN II

The design of the different detector components is driven by the RUN II high luminosity, the Tevatron short bunch spacing of 396 ns, and by the physics requirement of b decay vertex identification within collimated high- p_T jets. Figure 2.7 shows an elevation view of one half of the CDF II detector. In the following section, the different sub-detectors will be presented in more detail.

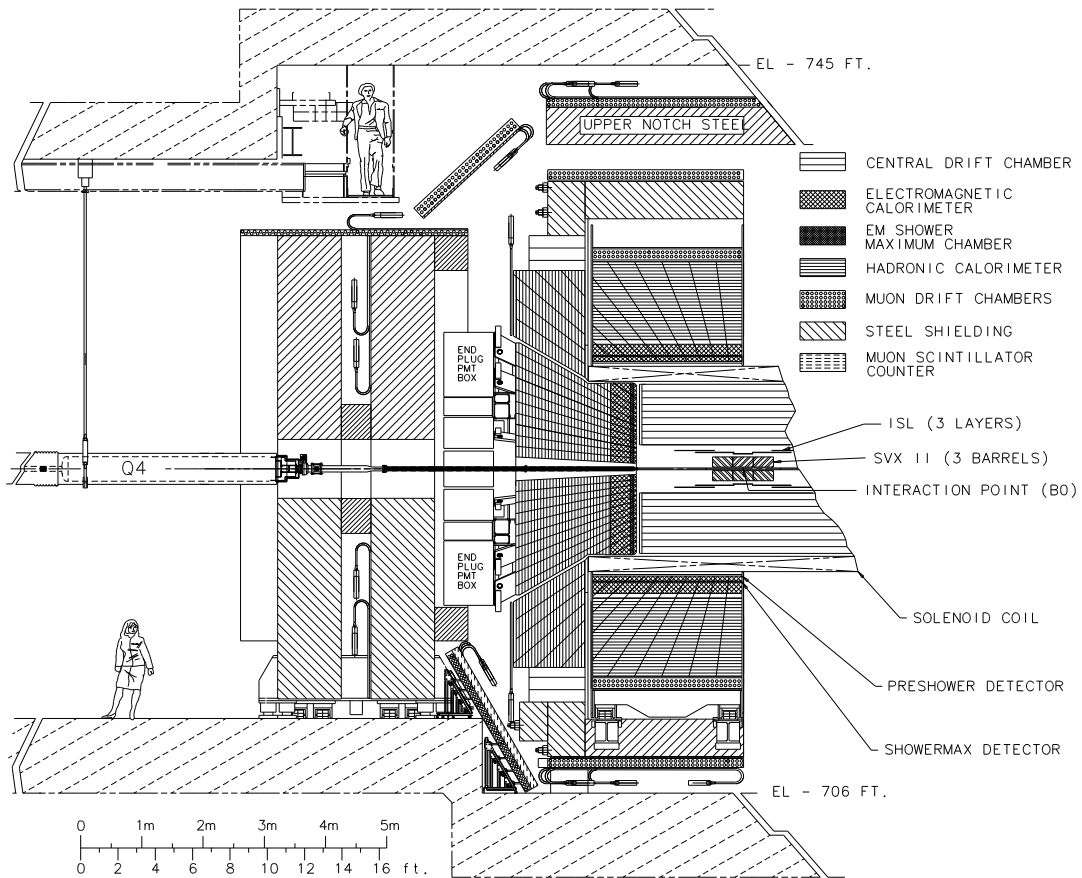


Figure 2.7: Elevation view of one half of the CDF II detector.

2.2.1 The tracking system

The Tracking System in RUN II is located close to the beampipe and is surrounded by a superconducting solenoid, 1.5 m in radius and 4.8 m in length. The 1.4 Tesla magnetic field parallel to the beam axis bends the track of a charged particle to a helix and enables a momentum measurement.

The tracking system consist of two different parts, the *Central Outer Tracker* (COT), an open drift chamber [13], and the *Silicon Vertex Detector*, a silicon strip detector. The silicon detector itself consists of three sub-detectors: the *Silicon VerteX detector of RUN II* (SVX II) [14], the *Intermediate Silicon Layers* (ISL) [15] and the L00, a single sided strip sensor mounted directly on the beampipe. A schematic overview is shown in figure 2.8.

All these sub-detectors are arranged in eight cylindrically layers around the beampipe (LAYER 0- LAYER 7). In figure 2.10 and 2.13, the schematic views of L00 and SVX II can be seen. Sections 2.2.2-2.2.4 give a short overview of the silicon sub-detectors and in section 3.2 a detailed description is presented. Table 3.1 and 3.2 contain the properties of all layers and silicon detector components.

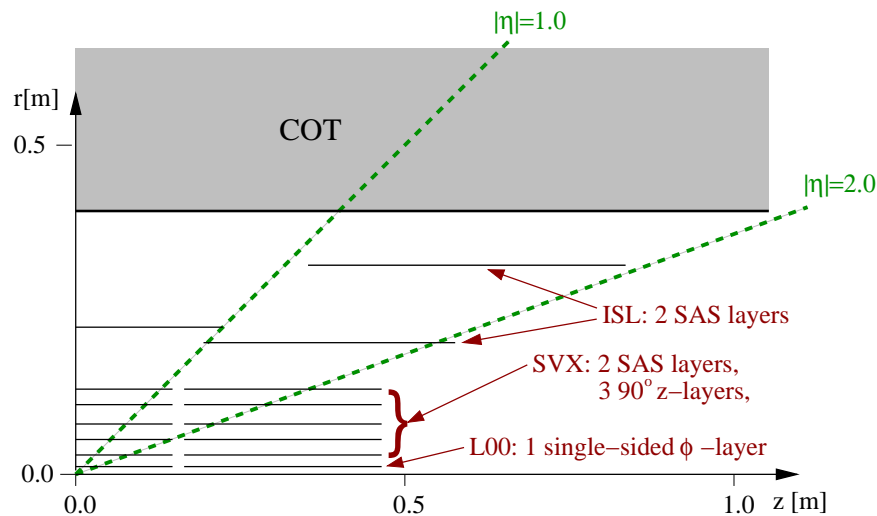


Figure 2.8: Longitudinal view of one quarter of the CDF II tracking system. The layer structure of all three silicon sub-detectors can be seen.

2.2.2 L00 sub-detector



Figure 2.9: Picture of the mounted L00

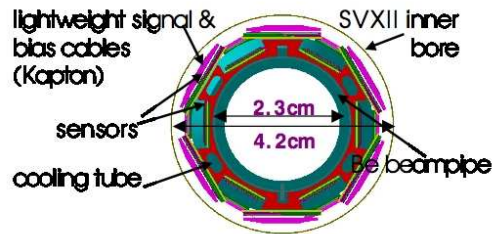


Figure 2.10: Schematic plan view of L00 and the beam pipe. L00 consists of 12 wedges on 2 alternate radii with overlapping edges.

L00 is a single sided silicon strip detector, mounted directly on the beam pipe. It is part of the upgrade for RUN II. The name L00 was chosen for this sub-detector because the name L0 was already used for the first layer in the SVX. To prevent gaps, the silicon sensors are arranged in two overlapping sub-layers at radii $r = 1.35$ cm and $r = 1.62$ cm. The $r\phi$ segment covered by one sensor, is called wedge. The sensors in the six inner wedges are different to the six outer ones, they are smaller and have only half of the strips on them, which can be seen in figure 2.10. Figure 2.9 shows a picture of the mounted L00. Due to the position directly on the beam pipe, it provides the closest possible ϕ -measurement to the $p\bar{p}$ -intersection point and improves the track resolution, see figure 2.11.

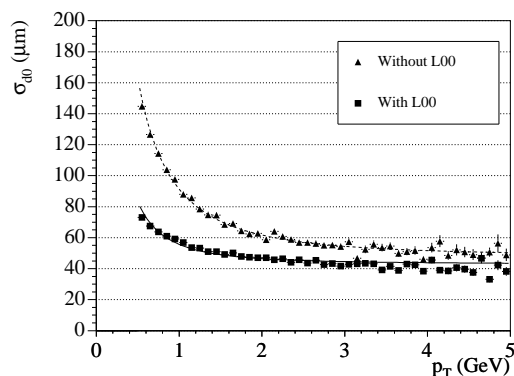


Figure 2.11: The resolution of the impact parameter d_0 is presented. Using the measurements of L00, the track resolution of the impact parameter d_0 improves. The impact parameter is the distance of closest approach of the track helix to the beam axis measured in the plane perpendicular to the beam. A precise measurement of d_0 is a prerequisite for a good lifetime measurement.

2.2.3 SVX II sub-detector

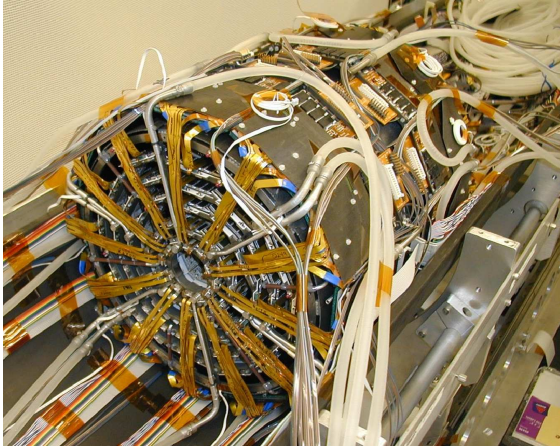


Figure 2.12: Picture of SVX II .

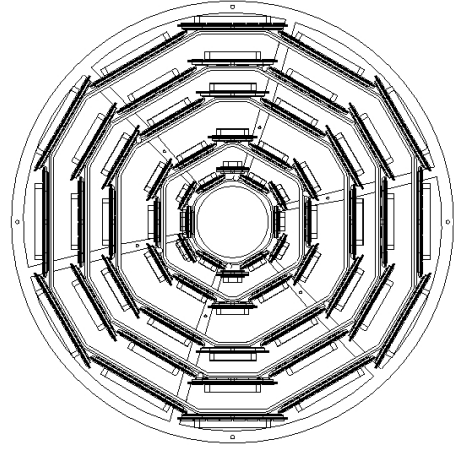


Figure 2.13: Schematic plan view of SVX II . It consists of double sided strip detectors arranged in five layers with twelve wedges each.

The SVX II, *Silicon Vertex detector RUN II*, is built of five layers (LAYER 1-LAYER 5) of double sided silicon strip sensors. The inner side measures the ϕ position. The back side of LAYER 1, LAYER 2 and LAYER 4 are rotated by 90° to provide best possible z information and are called Z90 layers. The strips of LAYER 3 and LAYER 5 form a small angle of 1.2° with respect to the ϕ side and are called *Small Angle Stereo* layers (SAS). Figure 2.12 shows a picture of the SVX II and figure 2.13 shows a schematic plan view. SVX II covers the region in $|z| < 0.43$ m on both sides of the interaction point and with the radii from 2.5 to 10.7 cm this results in a pseudorapidity coverage of $|\eta| < 2$. The silicon detector provides good pattern recognition and a 3D vertex reconstruction with an impact parameter resolution $\sigma_\phi < 30 \mu\text{m}$ and $\sigma_{z_0} < 70 \mu\text{m}$ for central tracks [4].

An overview of the properties of all layers is presented in the summary tables 3.1 and 3.2.

2.2.4 ISL sub-detector

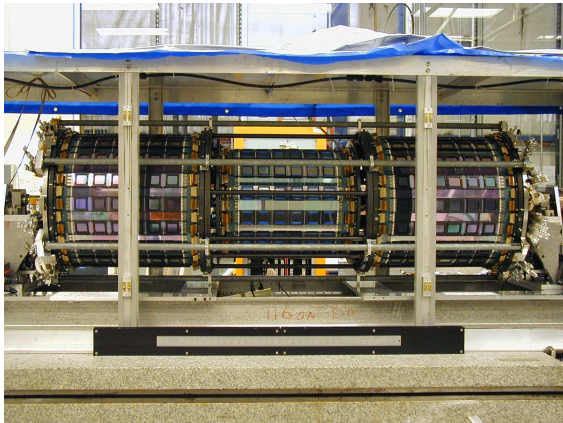


Figure 2.14: Picture of the ISL.

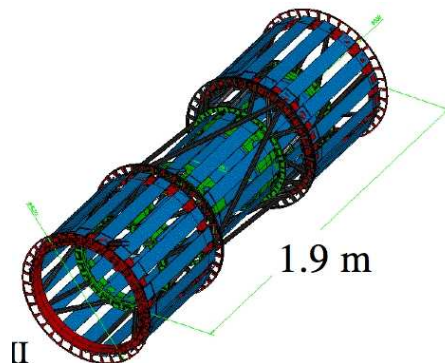


Figure 2.15: Schematic view of the ISL.

The ISL is also a part of the RUN II upgrade of the Silicon Vertex Detector and consists of two SAS layers. In figure 2.14 a picture of the ISL and in figure 2.15 a schematic view is shown.

The geometry of the ISL is a little bit different compared to the SVX II, especially LAYER 6, the inner layer of the ISL. The radius of the central region $r = 22.29$ cm is larger than the radius of the forward region $r = 20.21$ cm. The z coverage is $|z| < 0.61$ m due to longer sensors and shifted forward barrels.

The central region of LAYER 7, the outer layer, is not instrumented. The z coverage is $0.43 \text{ m} < |z| < 0.95$ m due to even longer sensors and shifted forward barrels.

With the radii from 20 to 29 cm and a total length up to 190 cm, the ISL covers also the range $|\eta| < 2$. This is shown in figure 2.8.

2.2.5 Drift chamber (COT)

The COT is a 3.1 m long cylindrical open wire drift chamber and provides tracking at large radii. It is built of 96 measurement layers organized into twelve alternating superlayers with axial and $\pm 2^\circ$ stereo measurements. The COT covers the radial range from 40 cm to 137 cm and all COT layers are in the range of $|\eta| \leq 1.0$.

The hit position resolution is approximately $140 \mu\text{m}$. This allows for a momentum resolution of particles of $\sigma_{p_T}/p_T^2 = 0.15\%$ $(\text{GeV}/c)^{-1}$. Due to the high luminosity and the short bunch spacing, the COT is designed to operate with a maximum drift time of 100 ns [4].

Although it has a much poorer position resolution compared to the *Silicon Vertex Detector*, it provides a much better momentum resolution due to the larger

radial extension and a higher purity due to lower track density than in the silicon detector. To enable a good spatial resolution of the tracks, the information of COT and the SVX II are combined.

2.2.6 Calorimeters

The solenoid and tracking system is surrounded by calorimeters, designed to measure the energy of particles by fully absorbing all particles except muons and neutrinos. There are, altogether, five calorimeter systems: the *Central ElectroMagnetic calorimeter* (CEM), the *Central HAdron calorimeter* (CHA), the *end-Wall HAdron calorimeter* (WHA), the *end-Plug ElectroMagnetic calorimeter* (PEM) and the *end-Plug HAdron calorimeter* (PHA), covering 2π in azimuth and $|\eta| < 3.6$ in pseudo-rapidity, see figure 2.7. Each calorimeter module is divided into projective towers, pointing to the nominal interaction point.

The calorimeters are sampling calorimeters. The active medium is a scintillator, the absorber is lead in the electromagnetic calorimeter and iron in the hadronic calorimeter. The different energy resolutions for the several calorimeters and the segmentation of the single modules in the $|\eta| - |\phi|$ ranges are shown in table 2.1. The central calorimeter is described more detailed in references [16, 17, 18]. The forward calorimeter, so-called plug-calorimeter is presented in more detail in references [4, 19]

Calorimeter	$ \eta $ range	$ \Delta\eta $	$ \Delta\phi $	Energy resolution
CEM	$ \eta < 1.1$	≈ 0.1	15°	$13.5\%/\sqrt{E} \oplus 2\%$ [16]
PEM	$1.1 < \eta < 1.8$	≈ 0.1	7.5°	$16\%/\sqrt{E} \oplus 1\%$ [20]
	$1.8 < \eta < 2.1$	≈ 0.16	7.5°	
	$2.1 < \eta < 3.6$	0.2 - 0.6	15°	
CHA	$ \eta < 0.9$	≈ 0.1	15°	$75\%/\sqrt{E} \oplus 3\%$ [17]
WHA	$0.7 < \eta < 1.3$	≈ 0.1	15°	$75\%/\sqrt{E} \oplus 3\%$ [17]
PHA	$1.2 < \eta < 1.8$	≈ 0.1	7.5°	$74\%/\sqrt{E} \oplus 4\%$ [20]
	$1.8 < \eta < 2.1$	≈ 0.16	7.5°	
	$2.1 < \eta < 3.6$	0.2 - 0.6	15°	

Table 2.1: Overview of the CDF calorimeter properties and segmentation in RUN II. The resolution was measured using a test beam of electrons for electromagnetic calorimeters and using single pions for hadronic calorimeters. $\Delta\phi$ and $\Delta\eta$ are the segmentation in azimuth and pseudorapidity respectively. The energy E is given in GeV.

2.2.7 Muon chambers

CDF uses four systems of scintillators and drift tubes to detect muons [21]. The central calorimeter absorbs the hadrons before they reach the *Central MUon detection system* (CMU). The CMU consists of four layers of drift chambers located outside the central hadronic calorimeter. It covers the pseudorapidity range $|\eta| < 0.6$ and detects muons with transverse momenta greater than 1.4 GeV/ c . Behind the CMU there are 0.6 m of steel absorber and additional four layers of drift chambers behind the steel. This system is called *Central Muon uPgrade* (CMP) and also covers the range $|\eta| < 0.6$. In addition the pseudorapidity range of $0.6 < |\eta| < 1.0$ is covered by the *Central Muon eXtension* (CMX). The muon system of RUN II provides a full coverage of the azimuth angle. The forward muon system used in RUN I has been replaced by the *Barrel MUon system* (BMU) covering a range from $1.0 < |\eta| < 1.5$. Table 2.2 gives an overview of the different muon systems in RUN II.

	CMU	CMP	CMX	BMU
coverage	$ \eta < 0.6$	$ \eta < 0.6$	$0.6 < \eta < 1.0$	$1.0 < \eta < 1.5$
drift tubes	2304	1076	2208	1728
counters		269	324	864
min p_T	1.4 GeV/ c	2.0 GeV/ c	1.4 GeV/ c	1.4 - 2.0 GeV/ c

Table 2.2: Design parameters of the CDF II muon detectors.

2.3 Data acquisition and monitoring

The data taking is divided into so-called runs that extend from a few minutes up to several hours in which the beam and detector status are not changed.

2.3.1 Trigger

To select the most interesting physics events from the large number of minimum bias events, a very efficient trigger is needed. The CDF trigger is a three level system with each level providing a sufficient rate reduction for the processing of the next level [22] and so the collision rate of 1.7 MHz is reduced up to 100 Hz which are written to tape with their typical event size up to 300 kBytes. The total data flow is reduced up to 35 MBytes/s, the maximum writing speed of the tape mass storage. Figure 2.16 shows a diagram of the data flow, and the reduction at each stage.

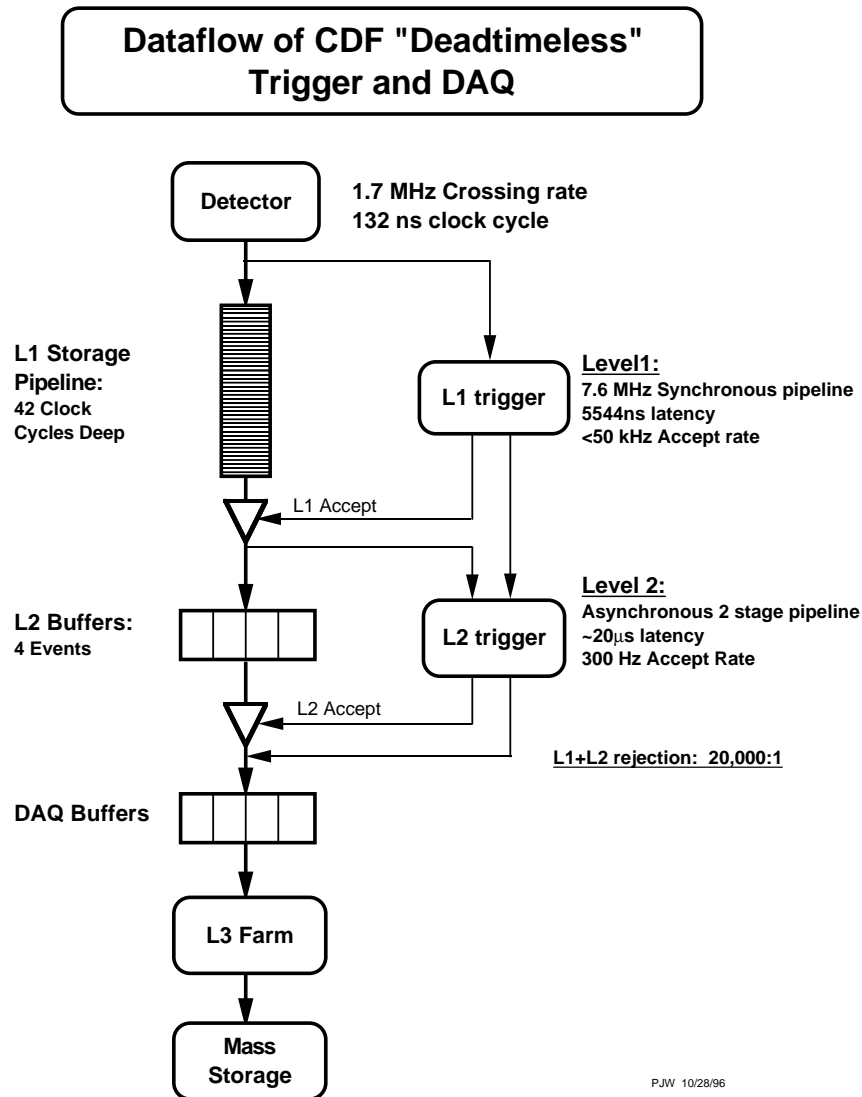


Figure 2.16: Block diagram of the CDF II data flow.

The first two trigger levels are hardware triggers and the third one is a software trigger running on a Linux PC farm.

The Level-1 trigger uses custom designed hardware to find physics objects based on a subset of the detector system. The hardware consists of three parallel synchronous processing streams, each one to identify different objects: calorimeter based objects, muons and tracks in the COT using the *eXtremely Fast Tracker* (XFT). The decision is done by simple counting these objects e.g. one electron with 12 GeV. If an event is accepted by the Level-1 trigger, the data is moved to one of the four on-board Level-2 buffers. The silicon information is not processed by the Level-1 trigger and is read out directly by the Level-2 trigger system if an event is accepted by the Level-1 trigger. The typical accept rate of the Level-1 trigger system is 30 kHz.

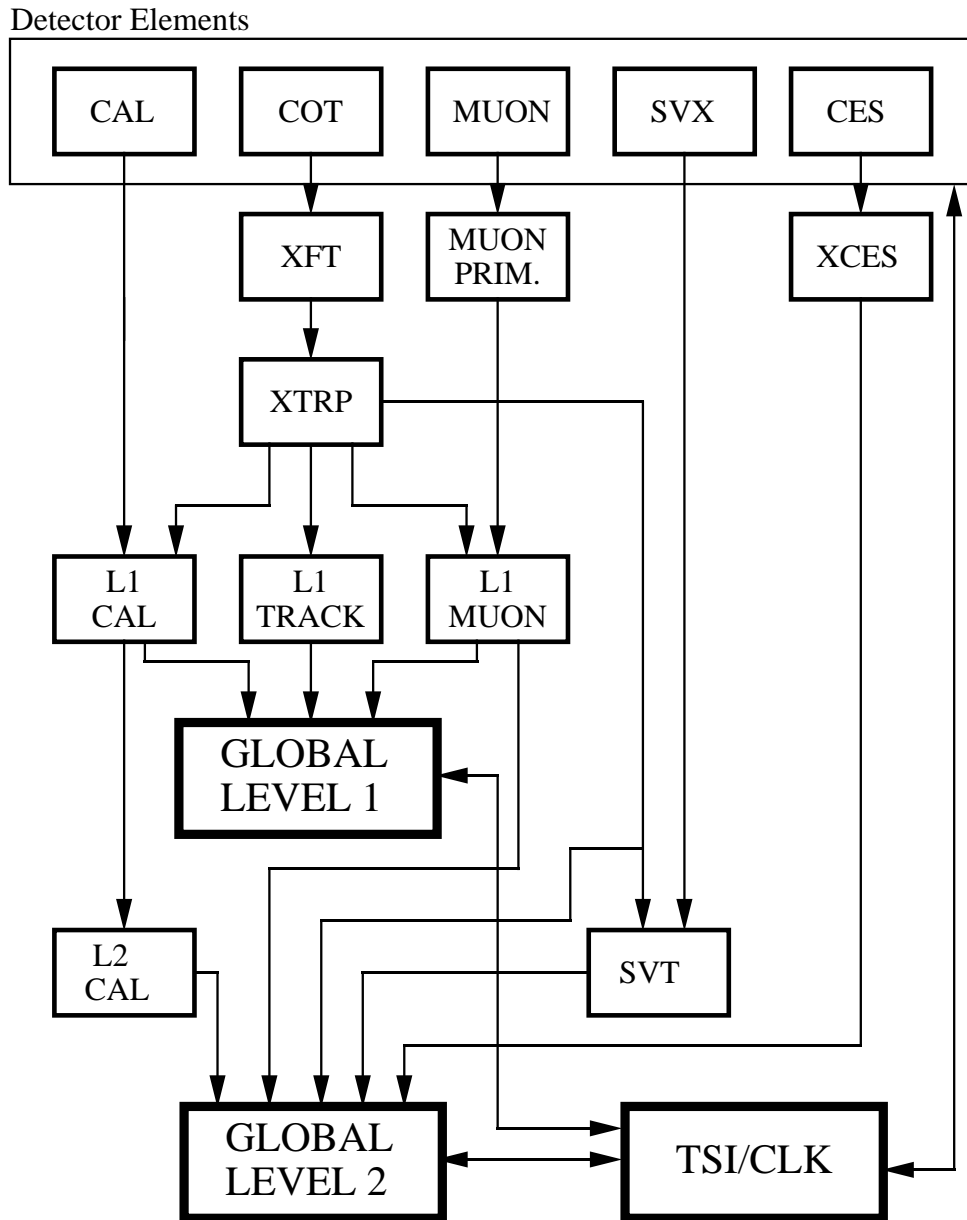
The Level-2 trigger does a limited event reconstruction also using a custom designed hardware. The hardware consists of several asynchronous subsystems, e.g. the hardware cluster-finder using calorimeter information. In addition, data from the *CEntral Shower maximum detector* (CES) can be used to improve the identification of electrons and photons. The most challenging addition for the Level-2 trigger is the *Silicon Vertex Tracker* [23], see figure 2.17. The SVT allows to select tracks with large impact parameter. This is the first system with a displaced vertex reconstruction on trigger level at a hadron collider. The Level-2 trigger accepts events with a rate up to 1kHz, which are transferred to the Level-3 processor farm [24].

The Level-3 trigger is a PC processor farm. The events are reconstructed and filtered, using the same algorithms which are also run in the “offline” reconstruction. The final events are written to permanent storage with approximately 100 Hz. To facilitate the handling of the huge amount of data collected with the CDF detector, events passing the Level-3 trigger, are currently classified into eight different streams. The triggers an event has passed decide to which stream this event belongs e.g. all events passing any of the highly energetic lepton triggers end up in “stream B”.

2.3.2 Online Monitoring

CDF consists of many different detector systems and types and is a complex multipurpose detector. Monitoring the data during data taking allows to quickly spot problems with one of the sub detectors, improving data efficiency and quality. For this purpose the so called *Consumer Framework* was developed based on the ROOT package. A schematic view of the framework is shown in figure 2.18. The *consumers* at CDF II [25] receive data from the *Data Acquisition* (DAQ). The most important feature is that the part which displays the monitored results is separate from the actual consumer programs.

RUN II TRIGGER SYSTEM



PJW 9/23/96

Figure 2.17: Block diagram of the CDF hardware trigger system in RUN II.

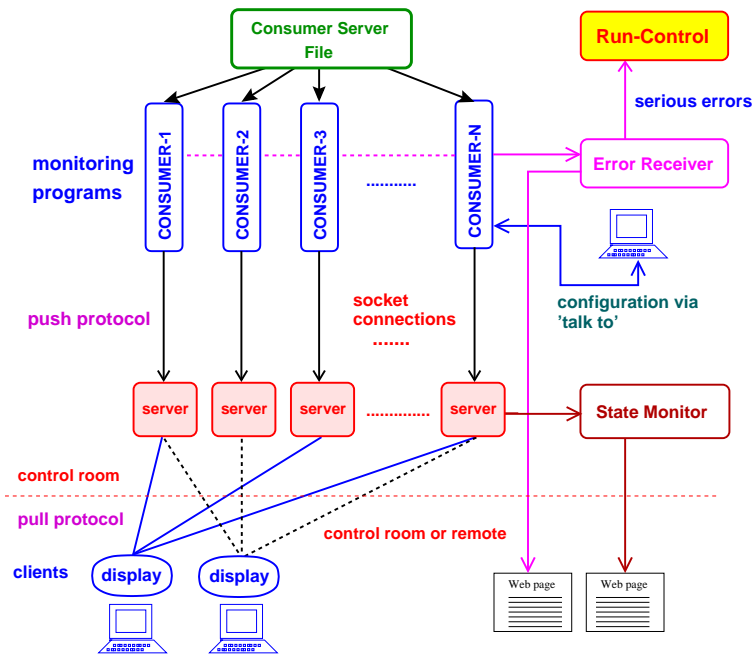


Figure 2.18: Overall design of the consumer framework.

The framework has three main components :

- *Consumers* :
modules which monitor and analyze objects in the event stream providing the connection to the rest of the CDF offline framework
- *Display Server / Display Viewer* :
a ROOT based program. The display viewer programs connect to the server as clients multiple display viewer programs can connect from anywhere in the world
- *Error Handler* :
receiving the error messages from the different consumers communicates with run-control so that the appropriate action can be taken (e.g. reset a SVX chip).

These tools enable the possibility to run the CDF experiment with a minimum of operators. A typical shift crew consists of a scientific coordinator, a specially trained Data Acquisition (DAQ) operator, a specially trained monitoring operator and a consumer operator who monitors online the quality of the data. In case of major problems, the shift crew can contact specific experts for each detector component. An operation manager coordinates all changes to the detector and a technician takes care of the high voltage, cryogenics and gas systems.

2.4 Software environment and track reconstruction packages

All data collected by CDF II is stored on digital mass storage and has to be reconstructed by software. The algorithms are implemented in the programming language C++ [26] and arranged in numerous packages. The object-orientated approach of C++ and its special concepts and paradigms are used to design the software packages efficiently [27, 28]. In this case, efficiency refers both to the ability to reconstruct all particle tracks and a good computing performance. All the high energy experiments in particle physics create a huge amount of data. To process all taken data the run-time performance has to be fast enough for trigger decisions in real time. Also the memory size of the programs with all the signal information from the detector and stored objects have to be limited.

All this has to be taken into account by the design of the reconstruction software. To find the best combination of the timing, memory and reconstruction efficiency is a non-trivial task and can not be done independently. For example the highest efficiency of track finding will be the reconstruction of every possible hit combination and a selection of the best one at the end. This is not possible in reasonable computing time and memory due to the very high combinatorics of the silicon measurements.

The implementation of the silicon track reconstruction is done in the *TrackingKal* package which is a part of the CDF II offline software [29]. The offline software is documented in [30, 31]. The *TrackingMods* package is an interface to the offline software and controls the silicon pattern recognition strategies with accessible interaction switches. The switches are listed in appendix C. The *TrackingSI* package communicates between *TrackingMods* and *TrackingKal*. The *TrackingKal* package [32] itself only contains a converter for data in- and output, the tracking strategies itself and the track fitter [33]. Also a lot of container and object classes are defined in this packages which inherit from each other. Special list containers are designed for fast access to the interesting contents which ease and quicken the pattern recognition software.

In the *TrackingKal* package of the CDF II offline software a Kalman Fitter is implemented. This fitting method is used during pattern recognition, for the final fit of reconstructed tracks and for refitting tracks in all track-based analyses. To optimize the computing performance all calculations are done analytically and an internal track parametrization is used to reflect the radius sorted assumption of the material density of the Silicon Vertex detector.

Chapter 3

Measurements with the silicon detector

In this chapter the silicon sub-detector and its hardware setup is explained in detail and the different prerequisites for track reconstruction are discussed. The reconstruction of particle tracks in the silicon detector is also called *silicon pattern recognition*. The track reconstruction is based on the position measurements of the interaction of charged particles with the silicon sensors. The reconstructed position of that particle interaction is called *hit*. The term hit will be used in this thesis representative for a reconstructed interaction position of a particle. The efficiency of silicon pattern recognition depends strongly on the hit reconstruction efficiency. For improvements of the track reconstruction strategies a better understanding of the silicon detector and its current performance is needed. For this task the hit quality is studied at the end of this chapter.

3.1 Basics of the measurements with a silicon sensor

The measurements in the silicon detector are the basis of the silicon track reconstruction. For a better understanding of these measurements a short overview about the process of obtaining measured signals is given.

3.1.1 Fundamentals of semiconductors

The fundamental silicon sensor structure is a pn-junction or diode. A schematic view of a pn-junction and its properties is shown in figure 3.1. Two extrinsic regions of oppositely doped silicon are brought together and the majority of carriers of charge (electrons in the n-doped region and holes in the p-doped region) recombine after diffusing into the other region. The region of the remaining

ionized donors and acceptors is called the space charge region *SCR*. An electric field is created in the SCR, which counteracts the diffusion. The potential drop is given by the difference of the intrinsic energy levels E_i^p, E_i^n in the neutral regions and is called built-in voltage V_{bi}

$$V_{bi} = \frac{1}{q_{el}}(E_i^p - E_i^n) = \frac{k_B T}{q_{el}} \ln \frac{N_A N_D}{n_i^2} \approx 0.5\text{V}, \quad (3.1)$$

where N_A and N_D are the densities of acceptors and donors and n_i is the mean occupation number. The maximum electric field E_{max} and the total width of the space charge region W_{SCR} [34] are given by:

$$E_{max} = \sqrt{\frac{2q_{el}}{\epsilon\epsilon_0} \frac{N_A N_D}{N_A + N_D} V_{bi}} \quad (3.2)$$

$$W_{SCR} = \sqrt{\frac{2\epsilon\epsilon_0(N_A + N_D)V_{bi}}{q_{el}N_A N_D}}. \quad (3.3)$$

With an external reverse voltage ($V_{bias} < 0$) which is called bias voltage the width of the space charge region can be extended to the entire thickness of the diode W_D . The full depletion voltage V_{fd} can be calculated by replacing V_{bi} in formula 3.3 with $(V_{bi} - V_{bias})$ and $N_{eff} = N_D - N_A$:

$$V_{fd} = \frac{q_{el}}{2\epsilon\epsilon_0} |N_{eff}| W_D^2. \quad (3.4)$$

To get a homogeneous doped space charge region a slightly doped bulk material with only a thin highly doped region of the opposite type is used. So the SCR covers mostly the homogeneous bulk and not the highly doped surface region, as can be seen in figure 3.3.

When a charged particle passes the silicon, it deposits a small amount of energy by ionizing the material. The energy deposition (dE) is given by the Bethe-Bloch formula [35], illustrated in figure 3.2:

$$\frac{dE}{dx} = C_{\frac{dE}{dx}} \cdot \frac{1}{\beta^2} \left(\ln \left(\frac{2m_e c^2 \beta^2 \gamma^2}{I_0} \right) - \beta^2 \right), \quad (3.5)$$

where $\beta = v/c$, $\gamma = 1/\sqrt{1 - v^2/c^2}$ are the relativistic properties of the particle, c is the speed of light, m_e is the electron mass, dx is the pathlength in the material and $C_{dE/dx}$ and I_0 are material properties. In the space charge region, the ionized electrons and holes are pulled to the corresponding sides by the electric field. This electric current can be measured. The collected charge is a measure of the energy deposit of the interacting particle. The combined information of amount and position of the total measured charge is called hit. Several hits can be combined to a particle track by pattern recognition.

3.1. BASICS OF THE MEASUREMENTS WITH A SILICON SENSOR

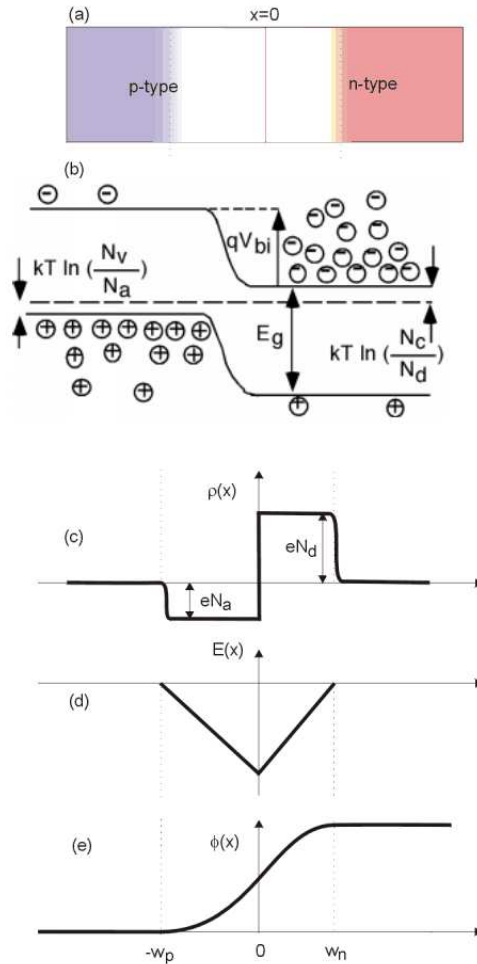


Figure 3.1:
pn-junction in thermal equilibrium.
a) Schematic view with depletion region
b) Energy band diagram with Fermi-energy
c) Space charge distribution
d) Electric field distribution
e) Potential variation with distance

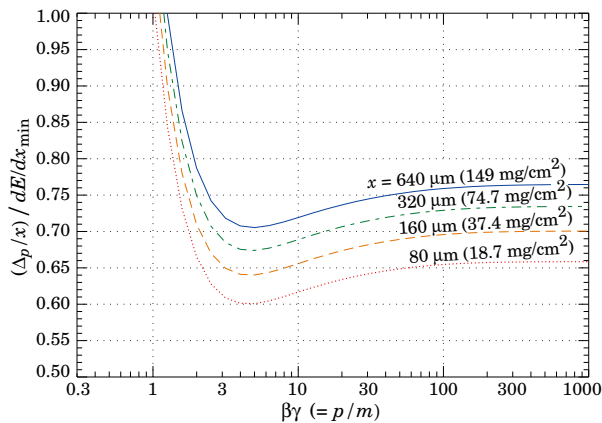


Figure 3.2: Graph of the Bethe-Bloch formula: Most probable energy deposit in silicon, scaled to the mean loss of a minimum ionizing particle, $388\text{eV}/\mu\text{m}$. [1]

3.1.2 Silicon strip sensor

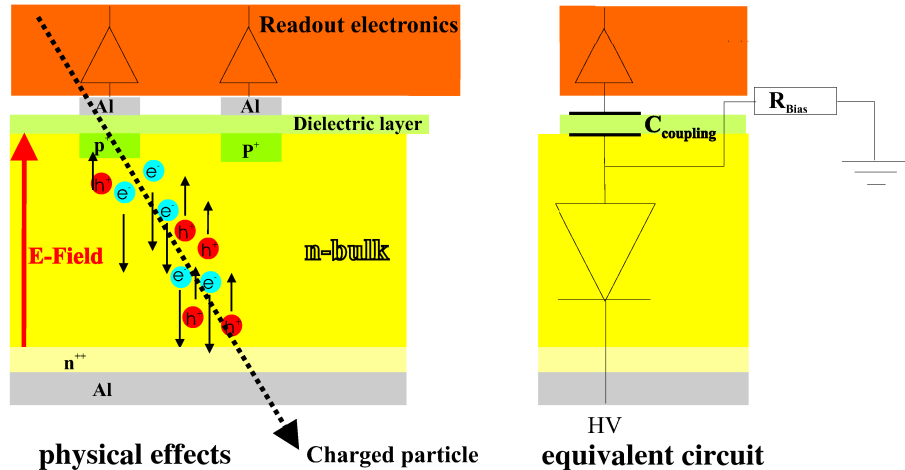


Figure 3.3: Schematic view of a silicon strip sensor. The highly doped p-region is built as strips on the slightly n-doped silicon bulk.

A silicon sensor without segmentation, which consists of the described pn-junction, can not give any position information within the silicon pad itself. To use such sensors for the measurement of the position of passing particles, the highly doped region is divided into strips and each strip is read out independently.

A typical silicon strip sensor uses a slightly n-doped silicon bulk with highly p-doped strips on one side. The distance between the center of two neighbor strips is called pitch. The highly n-doped region of the other side provides a good ohmic contact to the bias voltage connected via metal (aluminum). The readout electronic is connected to the p-doped strips via capacitive couplings over a non-conducting oxide layer. These channels provide a measurement of the charge from the ionization in the silicon along the strip. The position of the measured charge flow is determined by the strip position itself, which provides only a 1-dimensional information perpendicular to the strip orientation on the sensor.

Combining the 1-dimensional position of the strip with the position and orientation of the sensor a 2-dimensional position of a charged particle can be determined. The total energy deposition of a passing particle is mostly distributed over several strips. Therefore the correct interaction position of the particle with the silicon sensor has to be reconstructed by a so-called *clustering* algorithm, which combine all neighboring strip measurements to one single en-

ergy deposition. The measurements of silicon strip sensors do not provide the position of the passing particle directly.

A silicon sensor with a p-doped region divided into strips is called *single-sided silicon strip sensor* and provides a 2-dimensional position measurement of the passing particles. To enable the position measurement in three dimensions the n-doped region of the back side of the sensor is also divided into strips and this sensor is called *double-sided silicon strip sensor*. The strips of the back side are rotated to enable a measurement in the third dimension. The combination of the strip positions of both sides and the sensor position itself results in a position measurement of the energy deposition of the passing particle in all three dimensions. To provide the best position measurement resolution the strips on both sides are chosen to be perpendicular, the so-called Z90 sensors. A different type of double sided silicon sensors have a twisting angle of the strips on both sides of $\pm 1.2^\circ$ degree and are called *Small Angle Stereo sensors* (SAS).

Usually the strips of one side are parallel to the z -axis and provide a measurement in the $r\phi$ plane. The side of these strips is called ϕ side. The other side of a double-sided silicon sensor is called z side if the strips of both sides are perpendicular. The back side of the SAS sensors are called *stereo* side.

3.2 CDF silicon hardware overview

The silicon detector of CDF is built of three sub-detectors and consists of 8 different layers in total. The readout electronic is mostly the same and 7 out of the 8 layers provide a 3-dimensional position measurement by using double sided silicon strip sensors.

3.2.1 Silicon sensor module

A short overview of the silicon readout chain at CDF is given and the special properties of the used sensor modules are presented. A silicon sensor module is built of the sensor wafers which are bonded together with the readout hardware mounted on the end of one side.

Silicon sensor module with readout hardware

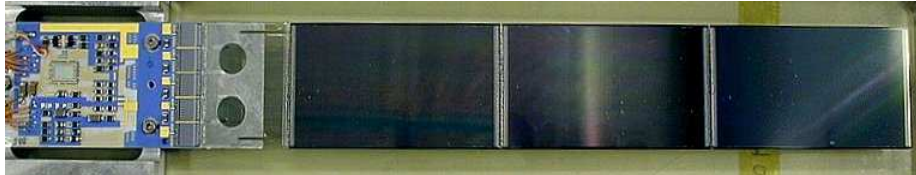


Figure 3.4: A picture of a silicon module with three bonded silicon wafers and the readout electronic.

The size of a silicon wafer is limited by the construction methods. As seen in figure 3.4, several sensors are bonded together to form a longer sensitive area. At one end an electronic hybrid is mounted with the readout chip and the bias voltage supply. Such a detector element is called ladder or half ladder. Each strip is connected to a readout channel. The channel number together with the half ladder identification provides the full position information of the signal. The CDF experiment uses the custom designed chip SVX3D for the silicon readout which is shown in figure 3.5. The chip consists of a 128 channel analog integrator as front-end and a digital back-end. The signal charge from the silicon strips is collected and digitized simultaneously which suppresses the dead-time of the chip. A dynamic pedestal subtraction can remove channels below a programmable threshold of the measured charge and reduce the data rate and readout time. The signal is already a pedestal subtracted *AnalogDigitalCount* (ADC). The silicon ladder is connected to the readout system via the portcards and junctioncards which delivers the information to the trigger system.

The width of the silicon sensors in each layer is different and therefore the number of strips and channels is different per sensor as well. In table 3.2 the number of chips and strips are listed for all layers. Both sides of the double-sided silicon sensors use the same kind of readout chips. For the Small Angle Stereo layers the ϕ side and the stereo side are very similar and on both sides the number of strips are the same. So the number of read out chips are the same for both sides.

The number of strips on the back side of the Z90 layers are more numerous compared to the ϕ sides. Several strips of the z side are read out together by only one channel. This is called multiplexing of the signal. The needed number of chips of the z side is reduced and is similar to the ϕ side. All numbers are listed in table 3.2.

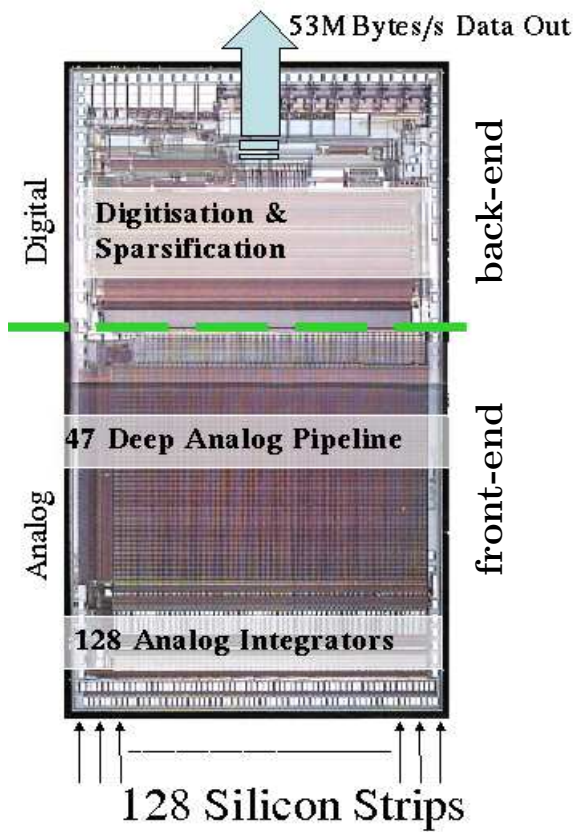


Figure 3.5: The Readout chip SVX3D is a custom designed chip for the silicon strip sensors of CDF II. It has a 128 channel analog integrator and a digital back-end.

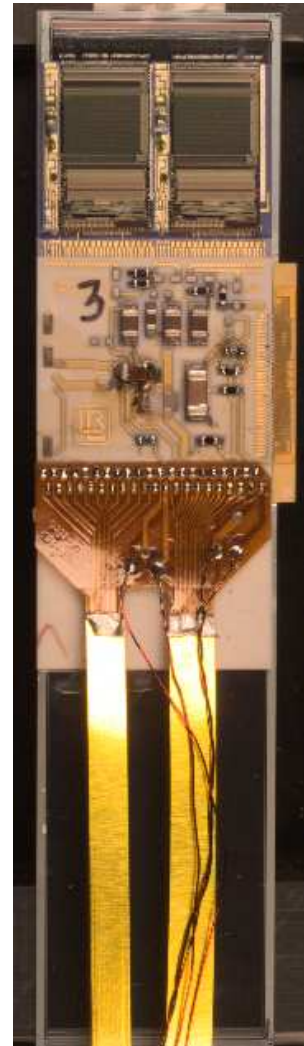


Figure 3.6: In LAYER 1 the 256 strips of the ϕ side are read out via 2 chips located at the outer end of the sensor. This is shown at the top of the picture.

Multiplexing

One readout channel of the z side in the Z90 layers delivers signal information from several strips of different segments of the wafer, see figures 3.7. In LAYER 1 four strips are read out together by one channel (quadruple multiplexing), in LAYER 2 via a triple multiplexing and in LAYER 4 via a double multiplexing. The real position of a reconstructed cluster of these strips is ambiguous because there is more than one possibility. Each of them is represented in a collection of hits by an extra hit at different positions but points to the same readout channel. The multiplexing-method is employed only on the z sides of the Z90 layers. In these layers the z resolution is reasonable for the track reconstruction later on. Only one of these ambiguous hits will be in a search road of the tracking and can be added to a particle track.

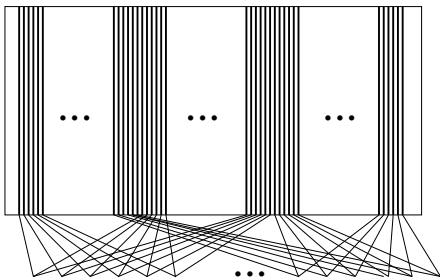


Figure 3.7: Example of the multiplexing of 3 strips in LAYER 2. On the z side three strips are read out via only one channel and so the origin strip of the signal is ambiguous.

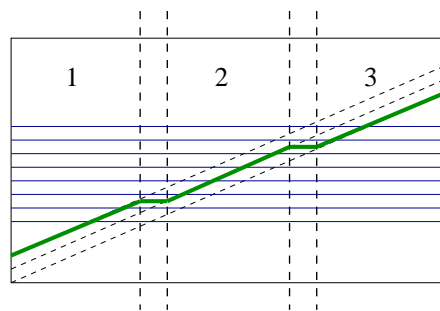


Figure 3.8: Zigzag bonding of the 3 silicon wafers in LAYER 7.

ZigZag bonding of Layer 7

The wafers of a halfadder are bonded together to build long strips over the entire length. The ϕ side, where the strips are orientated in z -direction, is bonded parallel in all layers. The stereo sides of LAYER 3, LAYER 5 and LAYER 6 are also bonded in the same way with the result of long straight strips over the entire halfadder.

For the three wafers in LAYER 7 this is done differently. The bonds are not parallel to the stereo strips itself but to the ϕ strips. This results in a stepwise shape of the stereo strips in this layer, see figure 3.8. Another difference of LAYER 7 is that the ϕ strips are on the n-side of the silicon semiconductor and the stereo strips are on the p-side. Due to the different drift velocity and drift directions of electrons and holes, this has to be taken into account for the hit center corrections.

3.2.2 Small Angle Stereo and Z90 layers

The two different types of double sided silicon sensors have different properties and are named after them. A schematic view of both types is given in figure 3.9 and 3.10. Both types have in common that the strips of one side are parallel to the z axis (parallel to the beam) and provide a $r\phi$ measurement.

The best resolution of the z measurement can be achieved by a twisting angle of 90° of the sensor back side. Layers which contain this sensor type are called Z90 layers. However the combination of the strips to one measurement is ambiguous. Figure 3.9 shows the nine possible combinations for three real hits. Without any other information the real position can not be distinguished from the fake ones. An additional ambiguity is introduced by the read out of several strips on the z side via only one channel. With this type of sensor a unique three dimensional information is not possible.

For a unique 3D measurement the SAS sensor is used. The SAS layers have the same number of strips on both sides of the sensor and so each strip is read out via one channel. Also a real particle position has only one possible strip crossing, see figure 3.10, and therefore the measurements of both sides can be combined to a unique 3 dimensional information. Only with the SAS layers a definite 3D-Hit can be reconstructed and so these layers are often called 3D layers. The z resolution of these sensors is about a factor of 50 ($\approx 1/\sin 1.2^\circ$) worse than the resolution of the Z90 layers, due to the flat crossing of the strips on both sides.

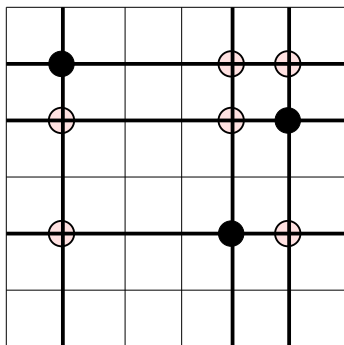


Figure 3.9: Schematic view of the Z90 layer. Three interaction positions result in nine possible combinations.

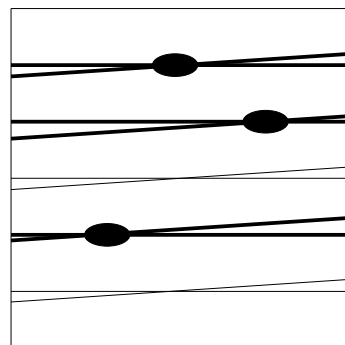


Figure 3.10: Schematic view of the SAS layer. The combination of the strips on both sides results in a clear position.

3.2.3 Position and identification of sensors

The global position of a measurement is the combination of the local information on the sensor, defined by the strip number, and the position of the wafer in the detector.

The center position and orientation of each silicon sensor is stored in a database. During maintenance or running, the exact position of the different detector parts can change. Therefore the detector components must be realigned periodically. The new position is stored to a database [36]. The smallest detector unit is the sensor with its readout electronic, the halfadder. Three quantities describe the position in the three dimensions of space.

Adapted to the cylindrical symmetry, the flat silicon sensors are built in several cylindrical layers, which corresponds to a radius information. To prevent gaps, one layer is built of two sublayers at different radii, an inner and outer one. Each flat sensor of a specific layer covers a ϕ segment of the full circumference, which is called wedge. The number of wedges depend on the layer and the sensor width. Figure 3.11 shows a transverse view of L00 and SVX II. The structure of the wedges and layers can be seen. Six halfadders are needed to cover $\approx 99\%$ of the interaction region. These are arranged in three barrels (east, center, west) with two segments each, see figure 3.12. One segment is called bulkhead. In the SVX II a halfadder consists of two, in the ISL of three wafers. The barrels are separated by a gap of about 1.5 cm in the SVX II. The east and west barrel of the ISL are shifted into higher $|\eta|$ range. LAYER 7 has no center barrel.

In this thesis, the offline naming is being used. So all the position information is split up into layer, wedge, bulkhead, side and strip number. The clustering in the reconstruction software uses this values to access the database and reconstruct a two dimensional hit position $r\phi$ plane or rz plane at the middle of the wafer.

An Overview of the silicon layers is given in table 3.1 and their specific mechanical dimensions can be found in table 3.2.

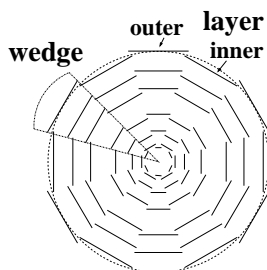


Figure 3.11:
Transverse cross view
of L00 and SVX II.

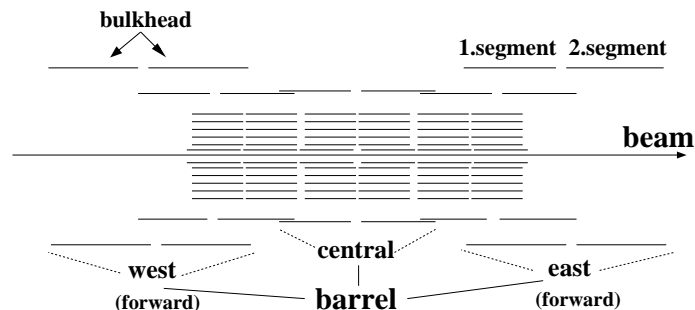


Figure 3.12:
Longitudinal view of the barrel structure.

3.2. CDF SILICON HARDWARE OVERVIEW

	canonical name	radius (cm)		readout coordinate	no. of wedges	no. of bulkheads	
L00	LAYER 0	inner	1.35	ϕ	12	6	
		outer	1.62				
SVX II	LAYER 1	inner	2.5325	$\phi, Z90$	12	6	
		outer	2.9825				
	LAYER 2	inner	4.1075	$\phi, Z90$	12	6	
		outer	4.5575				
	LAYER 3	inner	6.5075	ϕ, SAS	12	6	
		outer	6.9075				
	LAYER 4	inner	8.2075	$\phi, Z90$	12	6	
		outer	8.7075				
	LAYER 5	inner	10.1325	ϕ, SAS	12	6	
		outer	10.6825				
	ISL	LAYER 6	inner	19.71	ϕ, SAS	24	6
			outer	20.215			
central inner			22.585	ϕ, SAS	28		
central outer			23.09				
LAYER 7		inner	28.585	ϕ, SAS	36	4	
		outer	28.99				

Table 3.1: Overview of the silicon layers.

3.2. CDF SILICON HARDWARE OVERVIEW

properties	canonical layer name							ISL 6 & 7
	L00		SVX II					
	0 even	0 odd	1	2	3	4	5	
no. of ϕ strips	128	256	256	384	640	768	896	512
no. of ϕ chips	1	2	2	3	5	6	7	4
no. of z strips	-	-	4 x 256	3 x 384	640	2 x 512	896	512
no. of z chips	-	-	2	3	5	4	7	4
Vendor	SGS	H	H	H	M	H	M	H/M
no. of module	6	6	6	6	6	6	6	6/4
barrels	2	2	3	3	3	3	3	3/2
segments	3	3	2	2	2	2	2	2
no. of wafer (per module)	2	2	2	2	2	2	2	3
ϕ strip pitch (μm)	50	50	60	62	60	60	65	112
z strip pitch (μm)	-	-	141	125.5	60	141	65	112
total width (mm)	8.43	14.83	17.140	25.594	40.3	47.86	60.17	59.26
total length (mm)	156.9	156.9	148.7	148.7	148.7	148.7	148.7	207.3/ 224.5

Table 3.2: Mechanical dimensions of the silicon detector.
The vendors are *Hamamatsu* H, *Micron* M and *SGS-Thompson* SGS.

3.3 Reconstruction of hits

Before the silicon pattern recognition can start, the reconstruction of the silicon hits themselves has to be performed.

A passing particle deposits energy which can be measured via the charge of the ionized material. The silicon detector delivers these measurements strip by strip. To reconstruct the total energy deposit of the particle and the position of the interaction, the collected charge from all signal strips has to be combined. A sequence of consecutive strips, assumed to belonging to the same particle interaction, is called *Cluster* and contains only local position information. For the silicon pattern recognition the global position of a measurement is needed. Therefore the global position information is added to the cluster information and will be called *hit*. The *silicon hit reconstruction* is the basis for the *silicon track reconstruction* and is discussed in the following sections.

To compare the measured data with the expectation, collision events are simulated with Pythia and GEANT. For my study of the hit properties, for simulation the best available model of the energy depositions of a particle in the silicon sensor is used.

Simulation

For all simulations in this thesis the *Pythia* [37] event generator is used. This program is a so called *Monte Carlo generator* and can simulate $p\bar{p}$ collisions. The interactions of the particles with the detector material are simulated with *GEANT* [38], a material integrator which uses the CDF II detector description. The detector response of the material interactions is calculated with different, adequate models. The energy deposits in the silicon diffuse during the drift to the strips and for this process there exist several models. The fast geometric model only calculates the normal diffusion of the different charge carriers and adequately describes the cluster distributions for normal physics studies. The hit studies in this thesis are done with the much better *realistic physical* model, which needs more computing time but also takes additional effects like *Hall effect* or *Lorentz drift* into account. The distribution of the hitsize and the shape of their charge are modeled more accurately as well.

Another background comes from electrical noise in the real detector which is interpreted as signal. These hits are fake hits and are called *noise*. To simulate this, some hits are added randomly to the hit set.

To compare these simulated hits with measured hits the functionality of the current detector has to be taken into account. A database stores all information of the working and non-working (called dead) detector components. Using this information, all signals from broken parts are removed from the simulation. This is done for any detector status. So the simulation correspond to this specific

setup and is called *run dependent Monte Carlo simulation with realistic physical cluster model*.

In this thesis such simulated events are simply called *Monte Carlo* event or simulation. This name signifies their kind of production and will be used in this thesis for simulated collision events with the described production method and detector response.

3.3.1 Silicon strips used in the hit reconstruction

All measurements in the silicon detector are basically determined by strip information. Charged particles passing the silicon wafer, ionize the material and the charge flow is measured via the strips. All readout channels scan the strips for results above a certain threshold and integrate the charge flow to a digitized signal. The measured charge and the strip number are stored and for later reconstruction.

In the offline code the strip object contains the information of the strip-number and the local position on the silicon wafer. Also charge, quality and information about the neighboring strips is available. These are used to reconstruct the hit position by the clustering.

To determine the quality of a strip and its information, calibration runs are taken. The difference of these measurements to the expected ones is used to calculate the quality and can be used for later corrections. Some strips do not work anymore, they are called *dead*. If the occupancy of a strip is much lower than the average occupancy of all strips on a sensor, this strip are also called *dead*. Most of the time some other strips gives a measurable result, which passes the minimal required signal rate. These strips have a much higher occupancy than the average and are called *hot*. Strips with a occupancy, which is over a 100 times higher than the average will be called *very hot* in this thesis. All this information is collected in a database and is the base of a quality map of the silicon detector and its strips.

3.3.2 Reconstruction of clusters

The clustering is the first step of the reconstruction of an event in the silicon detector. Only in raw data the signal information is stored in a list of strips. The clustering algorithm iterates over all of them on the same wafer and combines them to a cluster, if they are next to each other. Figure 3.13 shows an example of typical clusters of passing particles. The position of the cluster is calculated by the mean weighted by charge of all strip positions between the two charge minima. Therefore the beginning of a cluster is a signal strip and the end is defined by the first no-signal strip. Clusters of only one strip are also possible by this definition. Usually clusters are separated by some strips sending no

signal, however two clusters also can overlap. This can happen, if two particles pass the detector close to each other. The clustering has to divide the long row of consecutive strips into two clusters, as seen in figure 3.14. The end of the first cluster and the beginning of the second is the strip with the lowest charge in the middle. The decision for dividing such charge deposits into separate clusters depends on their shape and on the fraction of the signal height between two neighboring strips. This is described in more detail in [39]. The position of a cluster is assumed to be the intersection point of the track of charged particles with the silicon sensor and is measured in local coordinates of the wafer. Depending on the side of the sensor and its type, there are two parameters for the position, the *long direction* and the *short direction*, as shown in 3.15. A perfectly aligned strip sensor only provides useful information in one dimension. Therefore a cluster only has a local one-dimensional position on the sensor.

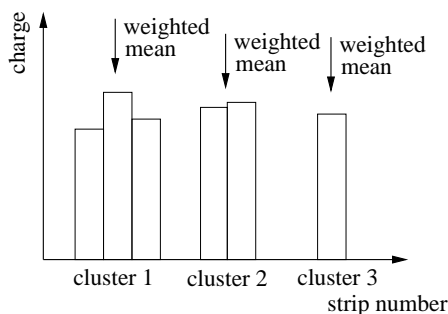


Figure 3.13: Typical shape of clusters with three, two and one strip.

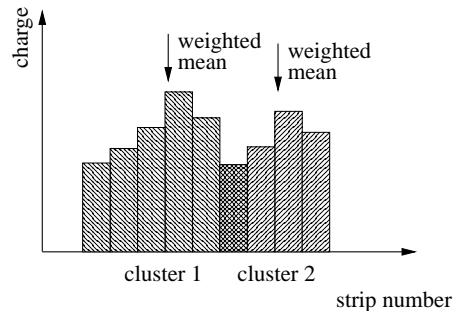


Figure 3.14: Clusters of two particles with overlapping charge deposit.

3.3.3 Reconstruction of hits

2D-Hit

For the silicon pattern recognition a global position of the measured interaction position is required. Therefore the hits are reconstructed from the local position information of a cluster and the position of the sensor in the detector. The hits provide a global position in the detector and contain all necessary information for physics analyses. These reconstructed silicon hits are defined as a synonym of the interaction positions of the particles with the sensors.

Together with orientation and global position of the silicon sensors, the local one dimensional measurement of the clusters can be transformed into a two dimensional information in the global coordinate system. So these hits will be known as 2D-Hit and have a definite position in the $r\phi$ plane or the rz plane, depending on the side of the sensor. The $r\phi$ hits are also called *axial* hits and the rz hits are also called *z* or *stereo* hits depending on the layer type.

3.3. RECONSTRUCTION OF HITS

detector	layer	type	hit resolution [μm]					
			1 strip		2 strips		> 2 strips	
			axial	stereo	axial	stereo	axial	stereo
L00	0	PHI	11	-	9	-	19	-
SVX II	1	Z90	13	31	11	26	23	54
	2	Z90	13	27	11	23	24	48
	3	SAS	13	13	11	11	23	23
	4	Z90	13	31	11	26	23	54
	5	SAS	14	14	12	12	25	25
ISL	6	SAS	24	24	21	21	43	43
	7	SAS	24	24	21	21	43	43

Table 3.3: Resolution of silicon hits and strips depending on the layer. Further details of test beam results can be found in [40].

3D-Hit

The $r\phi$ and rz hits on both sides of one sensor can be combined to a three dimensional position. These are the so-called 3D-Hits with a definite position in the detector. In principle it is possible in all layers but in the Z90 layers there are ambiguous possibilities and therefore no clear position can be determined. For the position in three dimensions, the ϕ position is taken from the ϕ hit and the radius is chosen to be between the radii of both original hits. The z position of the strip-crossing of all hit combinations on one SAS halfadder is calculated and if the result is in the range of the halfadder area, a 3D-Hit is reconstructed and stored in a separate hit list. From an $r\phi$ hit several 3D-Hits can be reconstructed due to many combinations with different stereo hits. These 3D-Hits have a global position in all three dimensions and contain all information of their originating axial and stereo hit.

3D-Hits are the highest level of *silicon hit reconstruction* and these objects contain the maximum available information. By construction these hits can only be found in the SAS layers: LAYER 3, LAYER 5, LAYER 6 and LAYER 7.

Resolution and hitsize

The resolution of the hit position depends on the number of strips used in the hit and their pitch d_{strip} . The pitch is the distance from the center of one strip to the center of the next. For a single strip the resolution of the position is $\sigma_{strip} \approx 1/\sqrt{12} \cdot d_{strip}$. The hit resolutions of the different layers are shown in table 3.3 and are separated by the number of strips in the cluster and each layer.

The number of strips in a hit is defined as the hitsize and can be used as a quality criterion.

The neighboring strips are uncorrelated in electric fluctuations on a strip. If a

3.3. RECONSTRUCTION OF HITS

detector	layer	type	fraction of hits [%]					
			1 strip		2 strips		> 2 strips	
			axial	stereo	axial	stereo	axial	stereo
L00	0	PHI	15.1	-	18.7	-	66.2	-
SAX II	1	Z90	8.8	13.9	17.8	19.0	73.4	67.1
	2	Z90	9.2	13.0	20.6	19.6	70.2	67.4
	3	SAS	12.6	9.0	22.9	21.4	65.5	69.6
	4	Z90	13.1	18.0	21.1	23.1	65.8	58.9
	5	SAS	18.1	11.5	24.1	23.5	57.8	65.0
ISL	6	SAS	15.2	19.8	25.5	25.0	59.3	55.2
	7	SAS	12.2	15.8	24.5	24.3	63.3	59.9

Table 3.4: Hit distribution with one, two and more strips in the different layers for realistic simulated data with physical clustering model and added noise.

detector	layer	type	fraction of hits [%]					
			1 strip		2 strips		> 2 strips	
			axial	stereo	axial	stereo	axial	stereo
L00	0	PHI	16.6	-	18.7	-	64.7	-
SVX II	1	Z90	8.9	13.9	17.8	18.9	73.3	67.2
	2	Z90	9.2	13.5	20.6	19.6	70.2	66.9
	3	SAS	13.0	9.6	22.9	21.4	64.1	69.0
	4	Z90	14.4	18.5	21.0	23.1	64.6	58.4
	5	SAS	21.9	13.8	24.1	23.5	54.0	62.7
ISL	6	SAS	19.2	20.3	24.0	25.0	56.8	54.7
	7	SAS	17.3	17.4	21.5	24.3	61.2	58.3

Table 3.5: Hit distribution of one, two and more strips in the different layers for data. The outer layers LAYER 5, LAYER 6 and LAYER 7 have a higher rate of hits reconstructed by one strip.

signal of a strip stems of a fluctuation, the neighboring strips do not have to send also a fake signal at the same time. Therefore hits of such fluctuations will be reconstructed by a single strip. This kind of *noise* will be seen in a high rate of hits containing exactly one strip. An estimation of the noise level can be extracted by simulated events. In table 3.4 the fractions of simulated hits with a certain number of strips are presented for all layers and both sides. The data distribution looks similar but in some layers the fraction of hits with only one strip is significantly higher, see table 3.5. The inner layers have a good agreement but the outer layers, especially LAYER 6 and LAYER 7 in the ISL have many more hits containing exactly one strip. The simulation generates also noise hits randomly to reproduce the detector behavior but can not describe the outer layers correctly.

3.3.4 Determination of the global position of hits

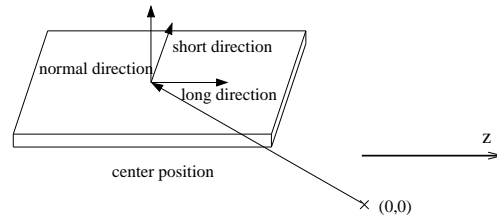


Figure 3.15: Definition of the geometrical parameters on a halfadder.

The position of the hits in an event depends on the local measurement on the wafer and the global position of the wafer itself. The alignment of the silicon detector stores the orientation and the global center positions of each sensor. The combination of these alignment information and the local hit measurements enable a parametrization in a global coordinate system of the entire detector, see figure 3.15. Using cylindrically coordinates is the best choice for the cylinder symmetric CDF detector and the global coordinate system is explained in figure 2.6.

$$\vec{x}_{global} = \vec{e}_{short\ direction} \cdot \phi_{local} + \vec{e}_{long\ direction} \cdot z_{local} + \vec{x}_{center\ position}. \quad (3.6)$$

In a perfectly aligned detector, the direction of $\vec{e}_{long\ direction}$ on a sensor is parallel to the z -axis and $\vec{e}_{short\ direction}$ is perpendicular. The global position of a hit can be easily calculated with:

$$\phi = \arctan\left(\frac{e_{short\ direction}^Y \cdot \phi_{local} + Y_{center\ position}}{e_{short\ direction}^X \cdot \phi_{local} + X_{center\ position}}\right) \quad (3.7)$$

$$z = e_{long\ direction}^Z \cdot z_{local} + Z_{center\ position}. \quad (3.8)$$

3.4 Study of the hit quality

The hits of the silicon detector are the basis of the track reconstruction. Therefore one relies on high quality reconstructed hits. The signal information of the detector can also contain fake hits, which should be identified and removed. To provide the best possible hit set to the track reconstruction strategies I have studied the hit quality and developed some requirements of the hit properties which are used to reduce the fake rate of the noise hits. The better understanding of the silicon hit properties and the improvement of the hit quality benefits the silicon track reconstruction.

3.4.1 Comparison of hit quality between measured and simulated data

The silicon sensors are read out via electronic chips with signal amplification. Therefore small charges can be measured but small fluctuations may also result in a signal. With strip information only, the noise can not be separated from signals of real particles. A possibility to estimate the fraction of the noise is to compare the number of 3D-Hits with the number of all 2D-Hits. Real particles should have a measurable signal on both sides of a sensor. These two hits have to build a three dimensional measurement and in a perfect detector with no noise all hits will be also a 3D-Hit. In this case the efficiency would be 100%. If there is no hit on the other side of the sensor, the hit will remain only as a 2D-Hit. If a signal stems from an electric fluctuation there is no reason for a signal on the backside and therefore the inefficiency of the 3D-Hit reconstruction is a measure for noise. The fraction of 3D-Hits depend also on the detector performance because if some strips or chips of one side are not working anymore, no 3D information is provided.

For example, in figure 3.16 and 3.17 the ratio of 3D-Hits to 2D-Hits is shown. Each histogram represents a bulkhead segment of a layer and each point is a halfadder with its corresponding wedge number on the x -axis. For comparison simulated data with fully reconstructed $t\bar{t}$ events with realistic physical cluster model is used and additional noise is added to represent the data correctly. The efficiency of over 90% in the simulation is due to a small number of noise hits. In measured data there are less 3D-Hits compared to 2D-Hits and the maximum fraction is up to 85%. The noise level is much higher in data and differs from the expectation of the simulation. In figure 3.16 all reconstructed silicon hits are used without any cuts. Hits added to a track should be cleaned up from noise because finding a particle track is a much more reliable information and is correlated to the hits. This can be seen in the histogram 3.17 a) with a much higher efficiency of 3D hits, almost 100%. Using only hits on tracks could introduce a bias because these hits were use to construct the silicon tracks. In the validation plot 3.17 b) only tracks are used which are not reconstructed with

the requirement of an existing 3D-Hit and no difference between the two plots is visible.

The conclusion of these plots is that the noise level on data is much higher than on simulated data.

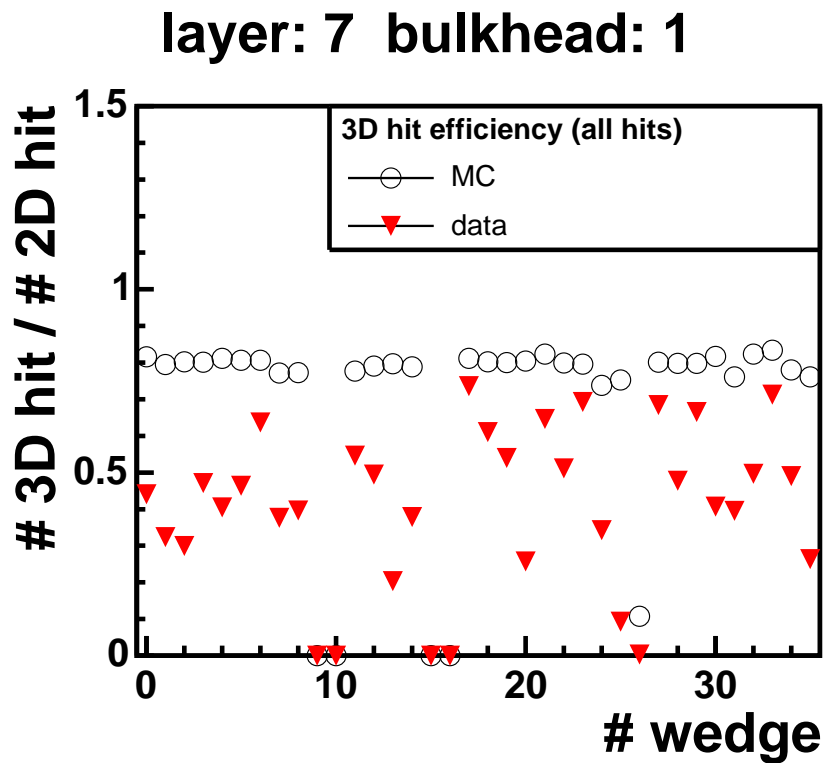


Figure 3.16: The fraction of 3D-Hits to 2D-Hits is a hint for noise. This example of layer 7 bulkhead 1 shows the lower fraction in data compared to simulated data. Each point represents an entire halfadder with the corresponding wedge number. If there are no 3D-Hits, one side is totally damaged. The higher noise rate in data can be seen on all sensors.

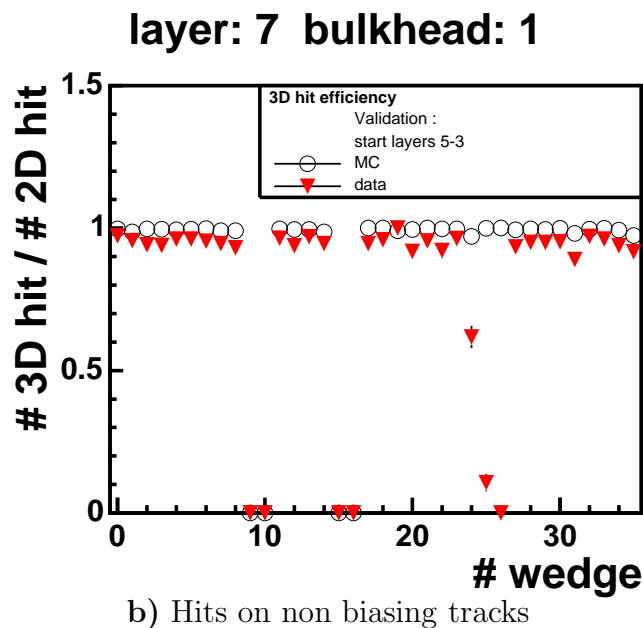
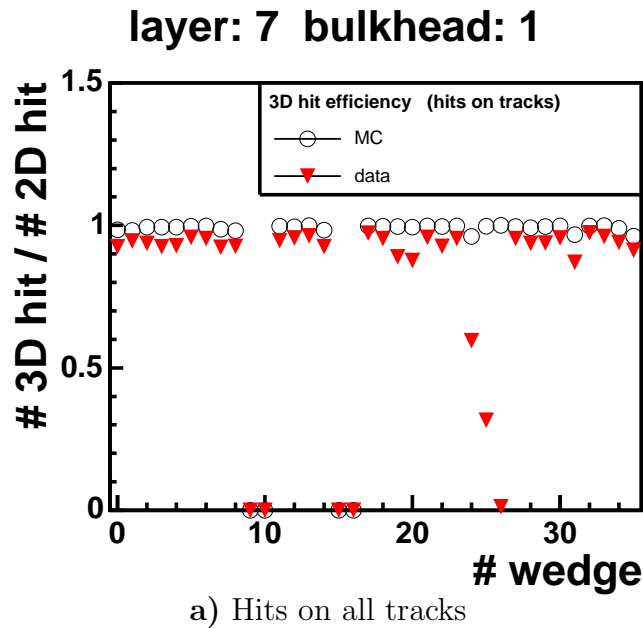


Figure 3.17: The fraction of 3D-Hits added to tracks is much higher and is in data and simulation almost 100%. So the pattern recognition cleans up the used hits and nearly no noise is added. Using tracks from all algorithms a) could introduce a bias because some of them are constructed with the requirement of an existing 3D-Hit. Those tracks with that hit as starting point are removed in b) to check the biasing.

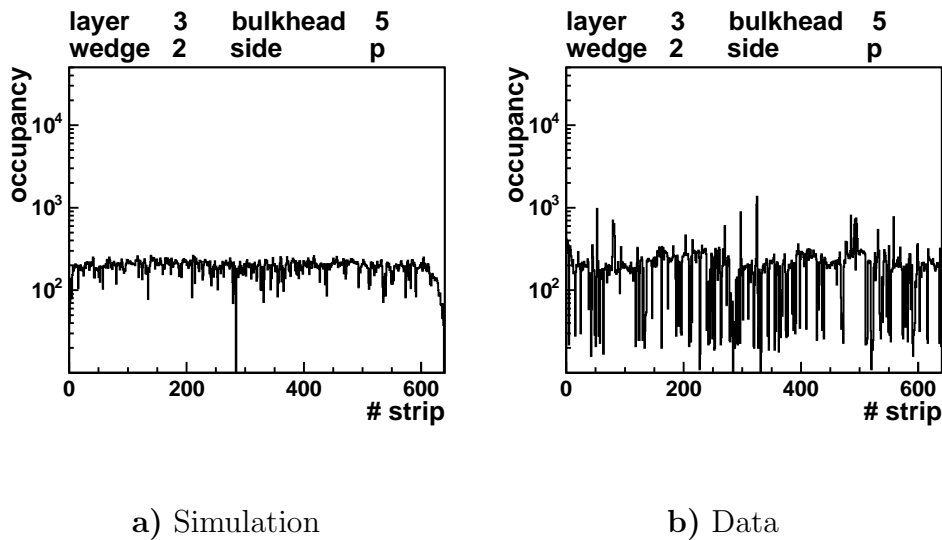


Figure 3.18: The occupancy of the sensor in layer 3, bulkhead 5, wedge 2, side p for simulation and data. The simulation a) has a flat distribution. In measured data b) the occupancy of the strips is very different and some *dead* or *hot* strips are visible.

3.4.2 Study of the strip occupancy distributions

The studies of the hit quality show a difference in the noise level between data and simulated data. In this section the noise level should be determined quantitatively and a possibility to remove some fake hits is presented. For a better understanding the occupancy of each halfadder side is investigated. Not all 1384 distributions can be displayed in this thesis and so only some typical examples will be discussed here. The following effects can be seen on several halfadders. An overview for all layers is given in the appendix A.1 - A.4.

In the simulated data all wafers are modeled in the same way and have a flat distribution of hit occupancy over all strips, see figure 3.18 a). There are no *hot* strips and only special *dead* strips are reproduced. Inefficient strips with a occupancy much lower than the average are not modeled, but there are a lot of those strips in measured data. In figure 3.18 b) the reconstructed hits of data are shown. The signal rate differs extremely strip by strip.

LAYER 7 has some specific effects at the edges. On all axial sides of this layer the occupancy rises at the wafer edge, so-called *ISL-wings*. The other side of these sensors have similar effects, but the entire last chip has a much higher signal rate. This can be seen in figure 3.19 a) for the axial and in 3.19 b) for the stereo side, but both effects are not reproduced in the simulation, see figures 3.19 c) and 3.19 d). Compared to the average number of hits in LAYER 3, the number of hits in LAYER 7 is expected to be lower due to the larger circumference and higher number of wedges. However in data the average in all

layers is almost the same which is already a hint for a much higher noise level in LAYER 7. The energy deposition of a passing particle can also be measured by one single strip, which has the same characteristic as the described noise. Without more information hits of particles can not be distinguished from fake signals which are statistically distributed. Using only hits which have been added to tracks show a cleaned up occupancy distribution due to the much more reliable track information, see figure 3.19 e) and 3.19 f). The good track resolution separates the noise from any measurements and therefore the probability of adding a noise hit to a track is very small.

Some *very hot* strips have an over 100 times higher occupancy than the average and always send a signal. An example of these very *hot* strips is shown in figure 3.20 b) and compared to simulation in figure 3.20 a). With this very high signal rate, these strips are added more often to tracks, which can be seen in the distribution of hits on tracks in figure 3.20 d). These strips are added 10 times more often to tracks than all others. With this effect a track candidate pointing in the region of the fake hit picks up the noise incidentally as the best possibility. Adding hits to a track changes its parameters. Noise hits can pull them into a wrong direction. For track reconstruction it is important to prevent this. One characteristic of these noisy hits is that they are composed of a single strip. Information about the silicon strips can be obtained by calibrations of the silicon detector. Such a calibration result is shown in figure 3.21 and the marks at 145 and 325 on the x -axis are the recognized bad strips. In these cases the neighboring strip has a short circuit and effects the calibration in the way that the pedestals on surrounding strips are reduced and all small fluctuations on these strips will become a signal. The hot strips are distributed in all layers and on each side. The tracking should use a cleaner hit set and has to take these hot strips into account.

3.4.3 Reduction of fake hits

Combining the information of quality and size, some noisy strips could be identified and will not be used for tracking anymore. If such hot hits of only one bad flagged strip are removed, the occupancy in the plots 3.20 c) looks much better. The distribution of hits added to tracks is flat again and has no *hot* strips anymore, see figure 3.20 e).

Hits containing such a *very hot* strip are dominantly reconstructed only from this single strip. Rejecting all hits of a single strip which are marked as bad in the calibration, remove 93.5% of the *very hot* strips in the hit set.

The quality of the hit set and as a consequence the quality of the tracks is much better and the fake rate is reduced. These effects are not modeled in simulation correctly and can only be studied on data.

3.4. STUDY OF THE HIT QUALITY

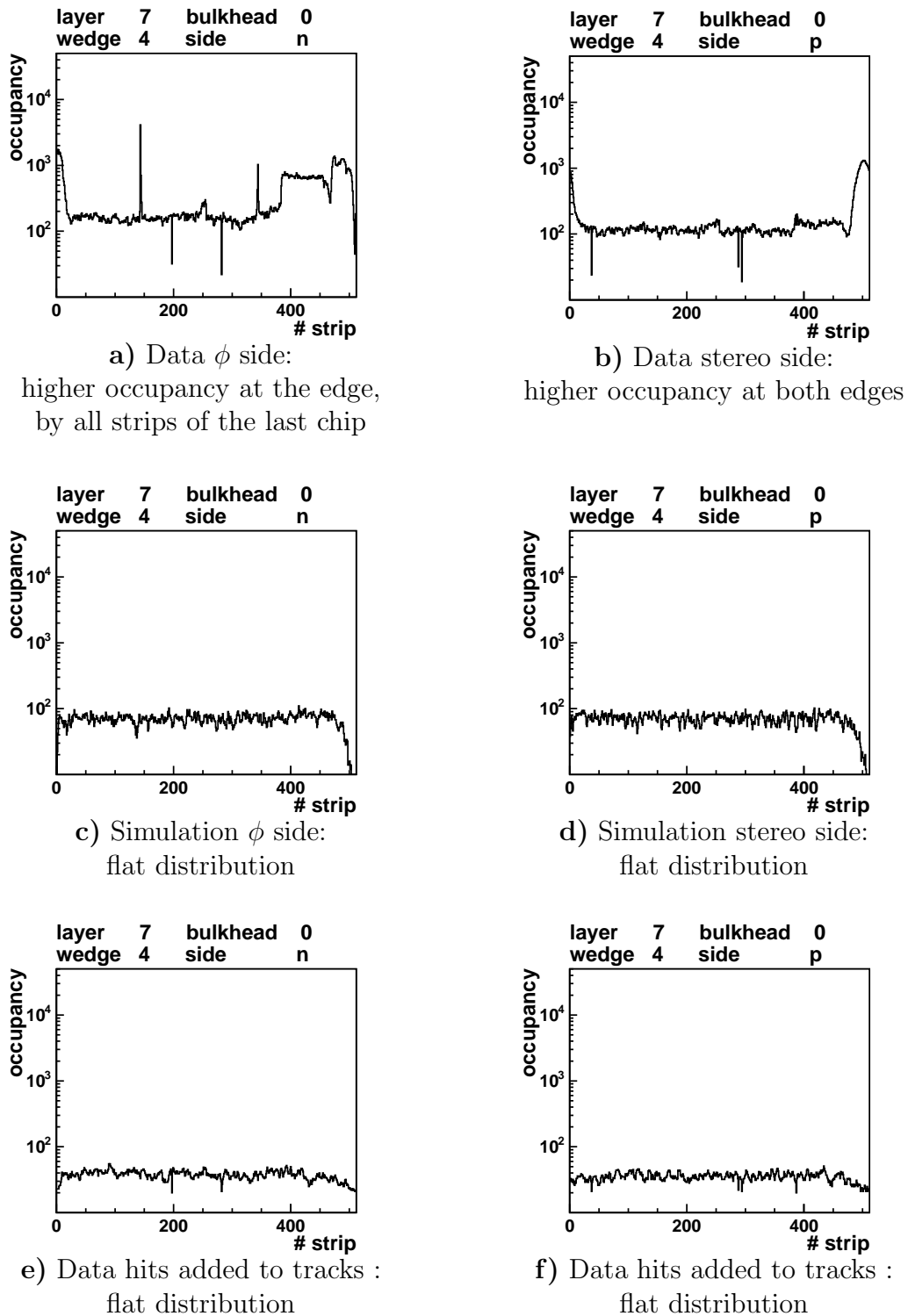
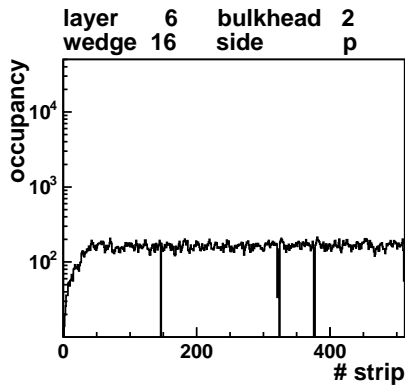
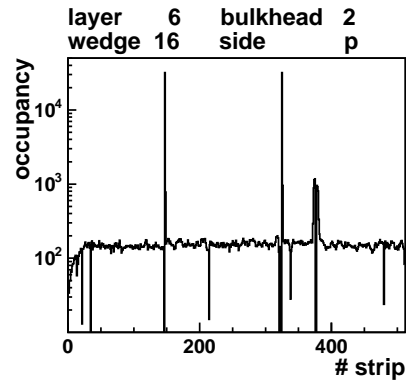


Figure 3.19: The occupancy of the sensor in layer 7, bulkhead 0, wedge 4 is shown. The data shows some differences compared to the simulation, like a higher signal rate at the edges b) and on the n side of the silicon the entire last chip has a higher occupancy a). In simulation the distribution of both sides is totally flat c) and d). This is not modeled in the simulation and seems to be noise. The track reconstruction collects mostly the reasonable hits and so these noise effects are gone and the distribution is flattened out e) and f).

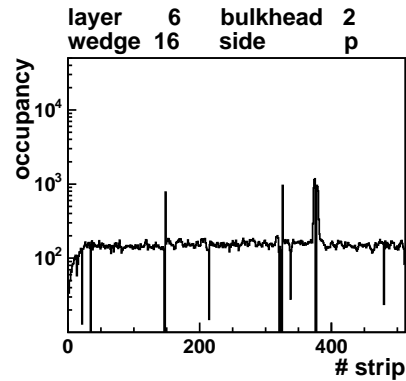


a) Simulation :
flat distribution

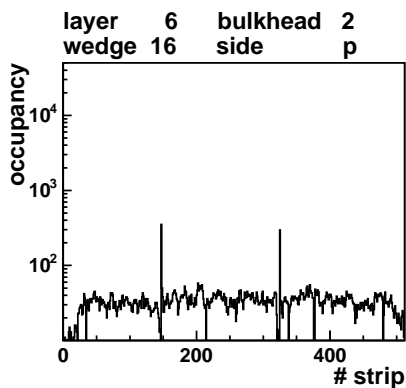


b) Data :
Two very *hot* strips with a 150 times
higher occupancy than the average

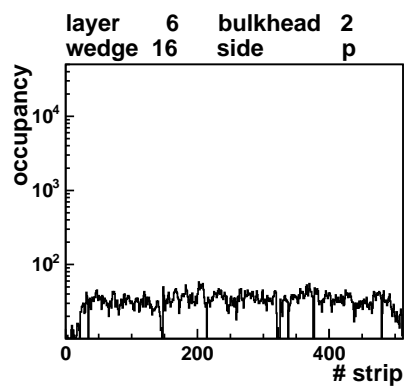
Figure 3.20: The occupancy of the sensor in layer 6, bulkhead 2, wedge 16, side p shows a flat distribution in simulation a). In data b) two very hot strips with a much higher occupancy are visible. These noise hits are also seen by hits added to tracks d) and can be removed by a cut on hits which are reconstructed by a single bad-flagged strip. The occupancy distribution for all hits is flattened out c) and the effect for hits added to tracks is gone e).



c) Corrected data :
Removing hits, built of only one bad
strip, from the hit set will reduce the
noise and the two very hot strips are
almost gone



d) Data hits added to tracks :
Noise is added statistically to
tracks. Hot strips still visible on
tracks
 ≈ 10 times higher



e) Corrected data hits added to tracks :
Without these *one bad strip* hits, the
distribution of hits on tracks is flat
again and the noise is not visible
anymore

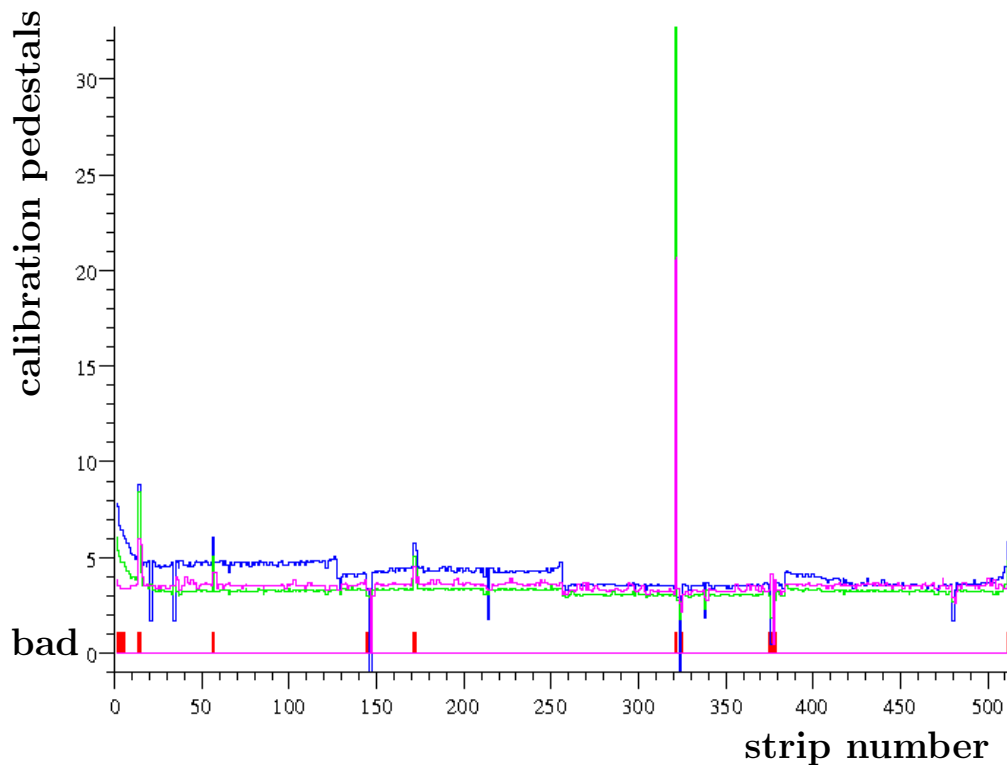


Figure 3.21: The calibration a of sensor in layer 6, bulkhead 2, wedge 16, side p is stored to a database. The bad strips are marked red on the x -axis. The *hot* strips 145 and 325 are identified as bad and a neighbor of a pinhole. The pedestal for these strips is chosen too low and all fluctuations will pass the required charge limit and become a signal. So two very hot strips are the result but these noisy strips are mostly one-strip-hit and can be identified.

Applying a correction and removing all bad one-strip-hits increases the quality of the hit set. The hitsize fractions of the corrected hit set is described much better by the simulation. Table 3.6 with the corrected rates of the hitsize is nearly the same as for the simulated data in table 3.4. LAYER 6 and LAYER 7 are corrected most and the rate of one-strip-hits is now much lower, as expected from simulation. The hits on tracks are almost free of noise. This allows the comparison to the physical fraction of the hitsize, see table 3.7. The rate of the one-strip-hits in the outer layer is still lower than in the corrected data. Hits from passing particles could be reconstructed with only one strip due to a very small energy deposit or a partly reconstruction by the hit clustering due to missing measurements. If the position of the intersection is at the border of the sensor, only the last strip can collect the signal charge. Dead strips can interrupt or end the sequence of strips of a charge deposit and stop the clustering to form a partly reconstructed hit. A further cut on these hits is not reasonable but another requirement for all hits is introduced to remove bad hits. Each hit has

detector	layer	type	fraction of hits [%]					
			1 strip		2 strips		> 2 strips	
			axial	stereo	axial	stereo	axial	stereo
L00	0	PHI	14.7	-	19.1	-	66.2	-
SVX II	1	Z90	8.7	13.9	17.8	19.0	73.5	67.1
	2	Z90	9.2	12.7	20.7	19.8	70.1	67.5
	3	SAS	12.2	8.3	23.1	21.7	64.7	70.0
	4	Z90	12.6	17.8	21.5	23.3	65.9	58.9
	5	SAS	17.6	11.0	25.4	24.3	57.0	64.7
ISL	6	SAS	14.3	19.0	25.4	25.4	60.3	55.6
	7	SAS	11.2	15.2	23.1	25.0	65.7	59.8

Table 3.6: Fraction of the hits with different number of strips per layers for corrected data. Hits with only one bad strip were removed and so the fraction in the outer layers are better described by the simulation.

detector	layer	type	fraction of hits [%]					
			1 strip		2 strips		> 2 strips	
			axial	stereo	axial	stereo	axial	stereo
L00	0	PHI	8.0	-	27.5	-	64.5	-
SVX II	1	Z90	8.3	13.0	24.8	27.1	66.9	59.9
	2	Z90	8.7	12.1	28.7	26.8	62.6	61.1
	3	SAS	11.2	5.2	29.4	25.5	59.4	69.3
	4	Z90	9.2	17.4	29.1	29.0	61.7	53.6
	5	SAS	13.8	5.9	32.4	28.0	53.8	66.1
ISL	6	SAS	11.3	14.3	28.1	28.6	60.6	57.1
	7	SAS	5.6	10.3	16.6	22.2	77.8	67.5

Table 3.7: Fraction of hits with different number of strips per layers for data tracks. This sample is cleaned up from noise and the fraction of one strip hits is lower.

to have a total charge higher than 20 ADC counts. This effects all hits but for the one-strip-hits it is harder to reach the limit and so this also reduces the fake rate for these kind of hits.

3.4.4 Determination of the CDF II silicon detector functionality

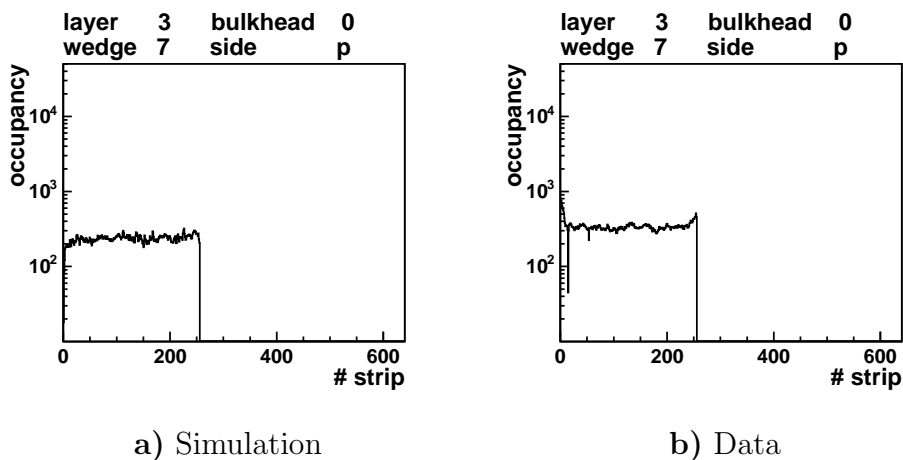


Figure 3.22: The occupancy of the sensor in layer 3, bulkhead 0, wedge 7, side p for simulation a) and data b). The simulation reproduces the same behavior as the data. Only the first two readout chips are working and the other three do not deliver any information.

The studies of the hit distribution also show a lot of *dead* strips and sensors. A single non-working strip reduces the cluster size of the charge deposit and results in a misplaced position of the hit but it can still be found. If there are some strips missing, the hit can not be reconstructed anymore and will result in an inefficiency for the tracking. Some sensors have one or more readout chips damaged, see figure 3.22 b) or can not deliver any information for all strips. The failure of a dead halfadder can have multiple reasons, also the hardware of the readout chain could be broken. A broken portcard or junctioncard can not be replaced, because they are mounted directly in the detector and are not accessible anymore.

Broken cables or erroneous optical fibers of the readout chain can change a bit of the binary strip number. The result of this modification is a transformation of the original strip number to an other number, which is already used by a strip. The original strip number seems to be dead due to the missing signals. Therefore the correct position of the signal of these strips is ambiguous and the distribution is similar to the distribution of a readout chip, with half the channels. Such an occupancy distribution is presented in figure 3.23 b). Only the first 64 strips of all four chips with 128 channel seem to send signals. The

seventh bit of the binary strip number is not transported by the readout chain and therefore the strips in the range 65-128 are projected to the range 1-64. The example of the three dead chips on the halfadder in LAYER 3, bulkhead 0, wedge 7 is reproduced in simulation as seen in figure 3.22 a) but not all of them. For the simulated events a database was used to remove the hits on these halfadders and to simulate the same detector behavior as on data. This database was designed for realistic data simulation, because in some time periods the silicon detector was partly turned off and the simulated events have to reproduce that.

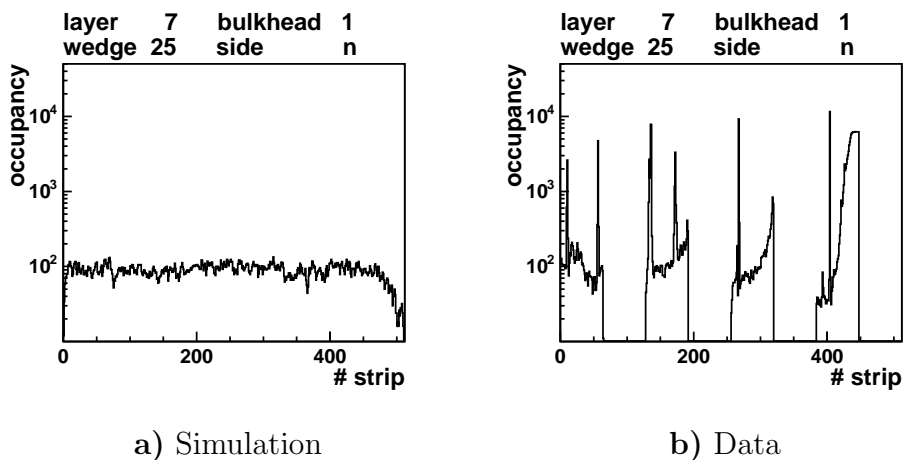


Figure 3.23: The occupancy of the sensor in layer 7, bulkhead 1, wedge 25, side n shows only a partly working sensor in data b). A bit error during transmission transforms the second half of each 128 channel chip to the first 64 channels. All signals seem to be measured by the first half of the chip and the second half seems to have no information. This is not reproduced by the simulation in a).

The control system of the silicon detector allows to power each single halfadder and so this was the smallest unit to turn off. At the beginning of this study the database stored only halfadder information, but the data shows many more dead wedges. This can be seen in figure 3.24 a) for an old simulated distribution compared to data 3.24 c). A new database was introduced and more information about chips are stored. With these additional information the simulation can reproduce much better the detector status during data taking. The new distribution of the simulated hits is shown in 3.24 b). The current map of the 3D-Hits can be seen in figure 3.25 for all four SAS layers. The side specific plots for all layers are in the appendix A.7 - A.6.

3.4. STUDY OF THE HIT QUALITY

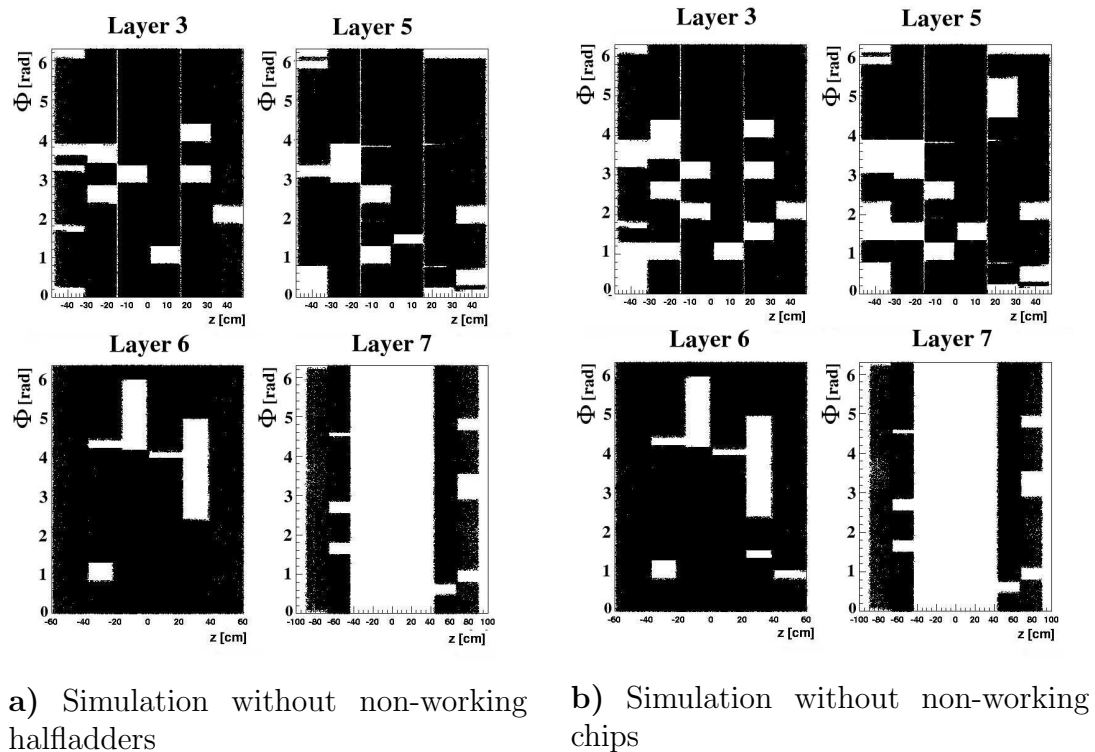
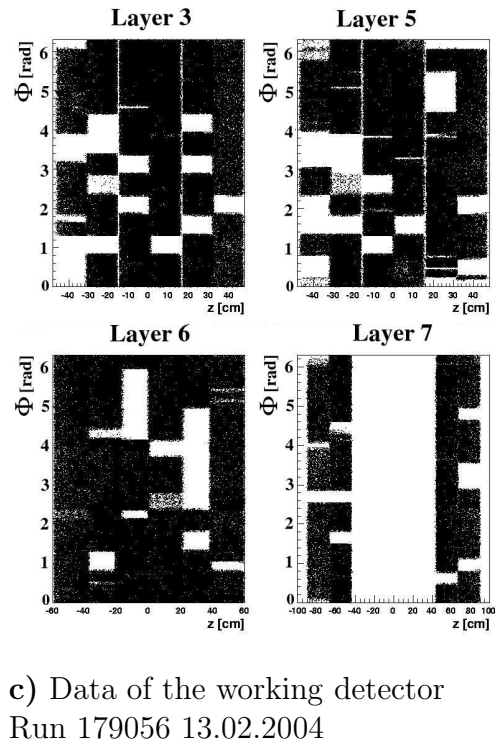


Figure 3.24: Map of working 3D sensors in SAS layers .

In the older simulation a) all hits on working halfadders are used and in the newer simulation b) the hits are signals only from working read-out chips. Some good halfadders have non-working chips on them and so the simulation which used the new database of readout chips has a finer resolution. The comparison between the simulated hit distribution and the reconstructed data c) is much better for the chip sensitive simulation. The old standard halfadder based database is replaced by the more exact readout chip database. The data is not changed but the agreement with the simulation is much better now.



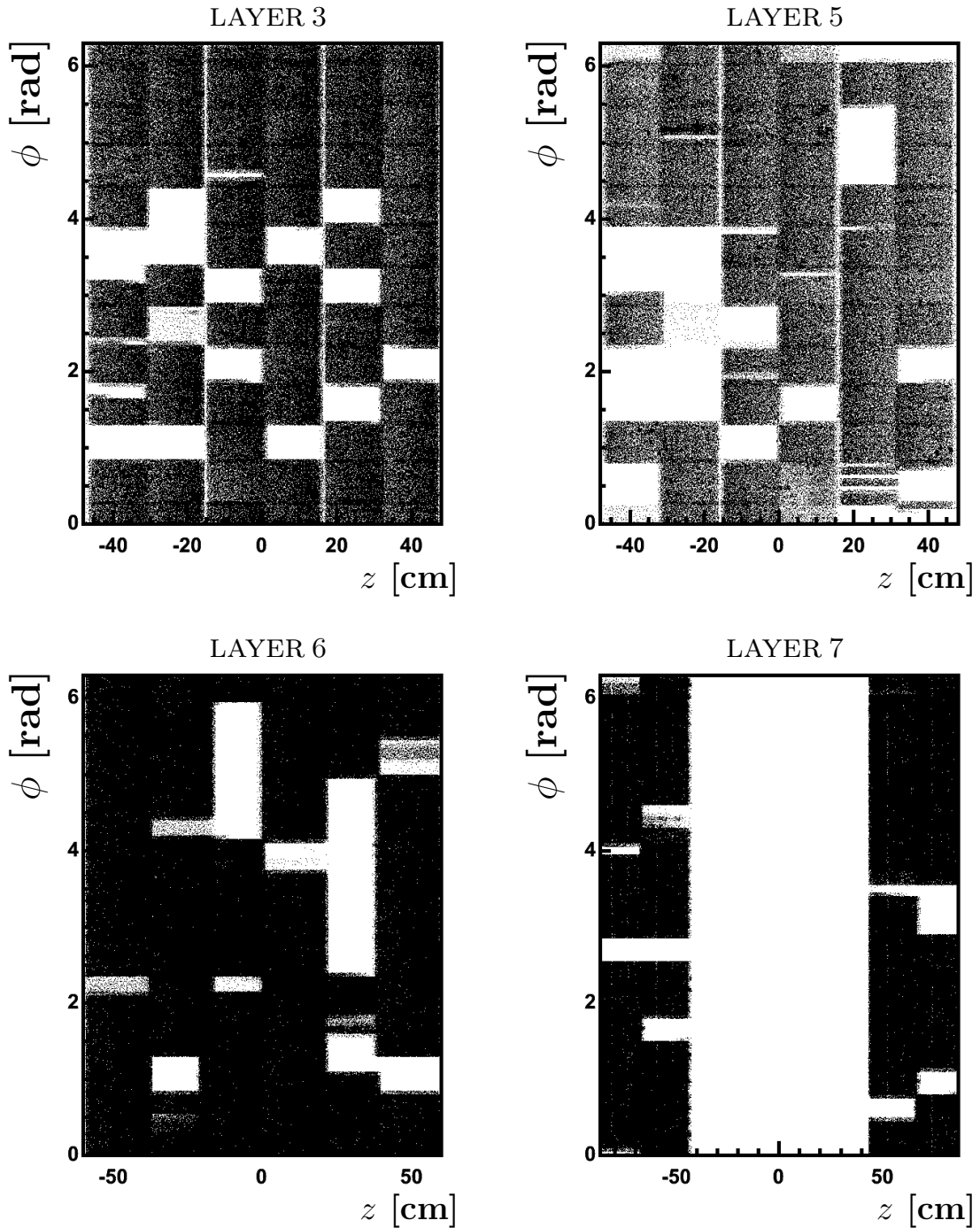


Figure 3.25: Map of working 3D sensors in SAS layers. For a 3D hit, both sensor sides have to be working and if one information is missing, there are no 3D measurements. The occupancy of all sensors is used to find holes in the coverage of the silicon layers. Only these four layers deliver three dimensional hit information which is necessary for silicon only tracking. Not reconstructible hits result in inefficiencies in the silicon pattern recognition. LAYER 7 has no central barrel, which explains the gab in the coverage of the central region $[-45.\text{cm},45.0\text{cm}]$.

3.4. STUDY OF THE HIT QUALITY

In the coverage of LAYER 6 two holes of contiguous wedges can be seen in figure 3.25 c). These halfadders are not powered due to the missing cooling of these silicon sensors. The cooling lines of the central barrel were blocked with glue during the installation which was noticed too late. However 11 of 12 lines of the installed ISL could be reopened successfully, see figure 3.26. Only the two ranges in the coverage of the LAYER 6 are still not recovered.

The efficiencies of the 3D-Hit reconstruction depend on available stereo side information. The back side strips are bond via aluminum wires which have a thickness of a few microns to the readout electronic. During calibration the used frequency of the synchronous readout of the test signal results in an oscillation of the wire due to the Lorentz force in the magnetic field. At the resonance frequency some of the wires broke and the readout chain for these strips are disconnected. In picture 3.27 a) the missing connection can be seen at the right side. The thin wires break at their weakest point, the bond. In figure 3.27 b) the broken bond is magnified.



a) ISL cooling line with connection elbow

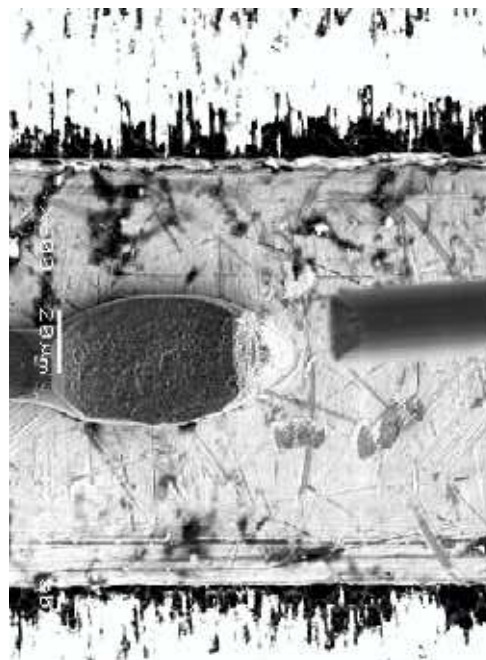


b) Cooling line blocked with glue and reopened

Figure 3.26: The ISL cooling lines of the central barrel were blocked with glue but 11 of 12 lines could be reopened.



a) Broken micron wires for read out z/stereo sides.



b) Magnification of a broken bond.

Figure 3.27: Broken bonds of z/stereo read out wires. The micron thin connections between the back side and the read out electronics broke by resonance oscillations due to calibration test.

Chapter 4

Track reconstruction

A track of a charged particle is the combination of all its position measurements along the trajectory. Additionally to the list of measurements, a track is fitted to a reference helix and provide the parameter set of the fit result. Track reconstruction is the task of combining all point measurements together to a track of a charged particle and is often simply called *tracking*. The measured signals of the particle track are separated point positions without a clear connection to each other. Therefore the hits of one track have to be identified and selected out of many others. The track reconstruction in the silicon detector is also called *silicon pattern recognition*, the task of finding the correct hits which belong to the track. Adding measurements to a track which do not belong to the particle will distort the track reconstruction. A combination of many arbitrary hits can result in a reconstructed track, which has no corresponding particle in the detector and is called *fake* track. The fake rate is a quantity of the performance of the track reconstruction.

The trajectory of a charged particle is bent to a helix due to a homogeneous magnetic field inside the detector. The curvature of the helix depends on the momentum and charge of the particle and the helix direction points back to the origin of the particle. Therefore the track reconstruction fits the selected point measurements to a helix and provides its parameters.

The silicon track reconstruction is a part of the event reconstruction for the CDF II experiment and the prerequisite for the physics analyses which are based on track information. The track information is also used for calculations of several other objects during reconstruction, like vertices.

I developed a new tracking algorithm and improved an existing strategy of the silicon track reconstruction. In this chapter both new strategies for silicon pattern recognition, *Silicon StandAlone Tracking* and *Silicon Forward Tracking* are presented.

4.1 Basics of track reconstruction

4.1.1 Parametrization of a track

The homogeneous magnetic field at CDF II is parallel to the z -axis. The orientation of the helices is along this field, so that a helix bends in the $r\phi$ plane of the detector. Three parameters are needed in the $r\phi$ plane and two parameters in the z direction to specify the helix.

Describing the trajectory as a single helix is only possible in a complete vacuum without any material interactions. A detector contains a lot of material which interacts with the passing particles. Due to multiple scattering and the energy loss in the material, the particle track is a piecewise helix from one interaction point to the next. An illustration of the helix in material is shown in figure 4.1.

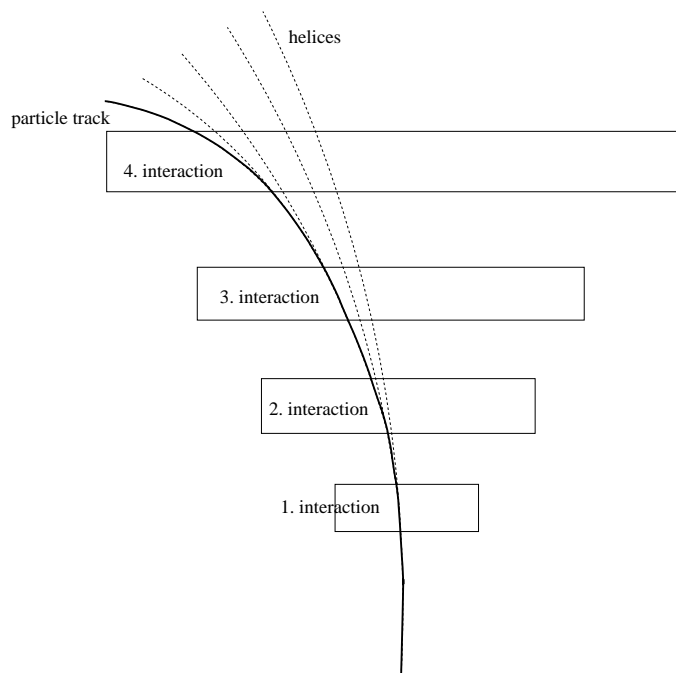


Figure 4.1: An illustration of a particle trajectory with material interactions is shown. The track can not be described by one single helix. Only from one interaction point to the next a helix can be used and so the track is in total a piecewise helix.

The perigee is the closest approach of the helix circle to a point of the origin in the $r\phi$ plane. The perigee is chosen as the reference point of the parametrization of the track helix. This is illustrated in figure 4.2 with an example of a track in the $r\phi$ plane. Relating to the piecewise helix in the detector, the helix

parametrization with only one set of parameters is not practicable for the reconstruction process but it is the best and easiest for the usage in physics analyses. At CDF the following five parameters are calculated [41] and stored for each track :

$$track_{perigee} = (\cot \theta, z_0, \phi_0, C, d_0) \quad (4.1)$$

- $\cot \theta$ is the cotangent of the polar angle θ . This is a measure of the helix pitch and the z component of the momentum. It corresponds to the pseudorapidity η which is normally used at hadron colliders $\eta = -\ln(\tan(\theta/2))$.
- z_0 is the z position at the perigee
- ϕ_0 is the direction of the helix in the $r\phi$ plane at the perigee.
- C is the half curvature of the helix circle in the $r\phi$ plane and has the same sign as the charge Q of the particle. $C = \text{sign}(Q)/2\rho$ where ρ is the radius of the circle with the center in (x_0, y_0) . C is a quantity for the momentum of the particle in the $r\phi$ plane. The $r\phi$ component of the vector of the momentum is called transverse momentum p_t .
- d_0 is the signed impact parameter. $d_0 = \text{sign}(Q) \cdot (\sqrt{x_0^2 + y_0^2} - \rho)$. It is the distance between origin and helix at minimum approach and has a sign to form a right handed system of \vec{p}_t, \vec{d}_0 and \vec{e}_z .

The described perigee parametrization uses the coordinate origin (0,0) as reference. Due to a shifted beam line position the origin of the particles is not in (0,0) and the relevant physical information are not identical to the parameters anymore. To provide the observables directly, the definition of the perigee parametrization is modified. The perigee is now the point on the helix with the closest approach to the beam position and so the impact parameter d_0 measures the distance between the perigee and the primary vertex of the $p\bar{p}$ collisions. The effect is illustrated in figure 4.3 a). The z position of the perigee z_0 also has to be corrected, especially for forward tracks with a high η value. This effect can be very large, see figure 4.3 b). The beam line position is not fixed and varies with time, so the reference for the perigee definition and the coordinate system of the parametrization has to be adapted.

4.1.2 Track fitting

One part of the track reconstruction is the track finding process, the so-called pattern recognition. The other part is the track fitting process which provides the best parameter estimation of a given hit sample. The track helix has five parameters which are correlated and so the errors of the parameters are given by a 5x5 matrix, the so-called covariance matrix. Track fitting uses statistical

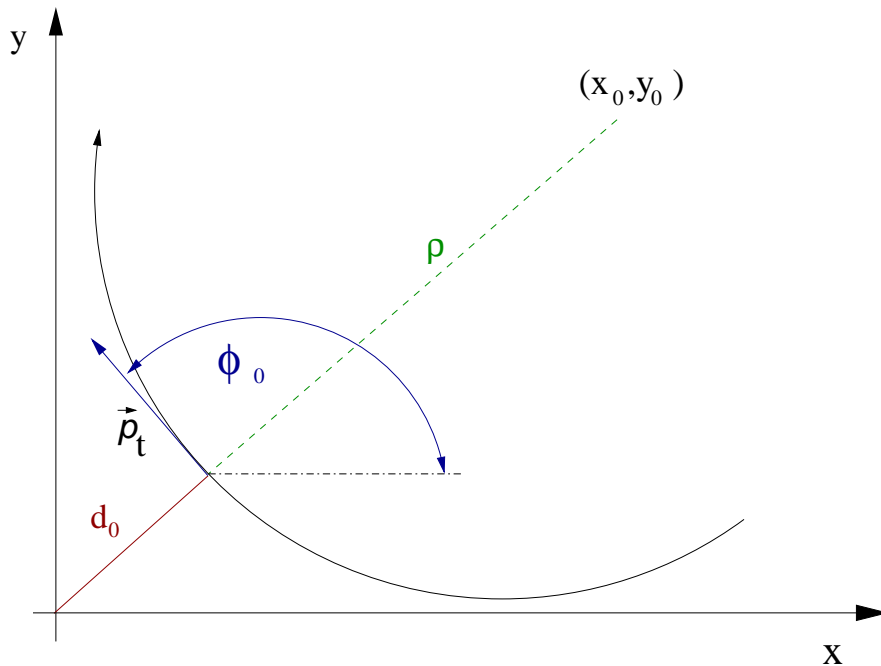


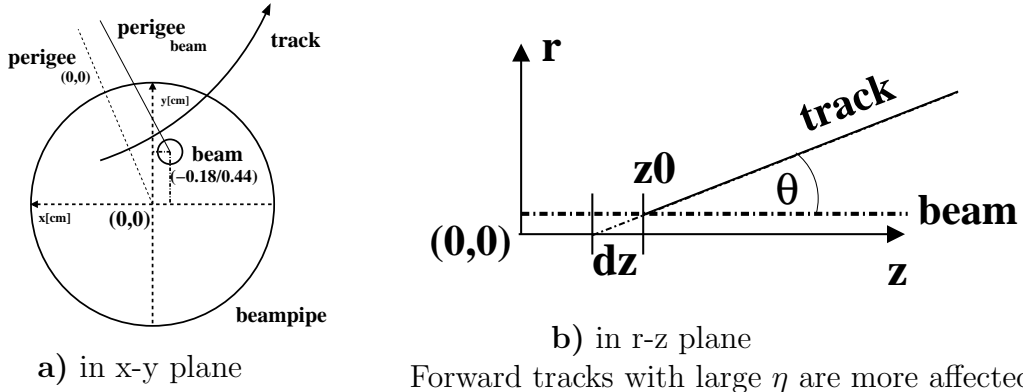
Figure 4.2: Parametrization of a charged particle track in the r/ϕ plane. At CDF II the perigee is used for parameter definition.

methods to estimate the track parameters and their covariance matrix. Out of the many possibilities of different methods, the one which suits best to the defined requirements should be selected [33].

The fit method should also provide a measure of the fit quality. On the basis of this the resulting track can be accepted or reject. Every method based on a χ^2 minimization suits for this task.

The fitter has to be very fast and should have the ability to also fit a part of a track. These features already allow the usage of the fitter during pattern recognition. A progressive fitter will implement these abilities due to the incorporation of new measurements into the fit step by step.

As mentioned in section 4.1 the trajectory in the real detector is a piecewise helix due to the energy loss of the particles by the interaction with material. The energy deposit depends on the momentum and the mass of the particles and has to be taken into account by the fitter. For every track fit, the fitter requires a mass of the particle to which the track corresponds. The majority of the particles in the detector are pions and so the pion mass m_π is used as a default mass if no other particle hypothesis is used for the track fit. During track reconstruction all tracks are fitted with the default pion hypothesis, since information about the particle hypothesis are not available during initial track reconstruction. With a new particle hypothesis from particle identification the refitted track will provide a better parameter estimation and a more exact result. At CDF II all fitting methods are equivalent to a χ^2 minimization. For the im-



Forward tracks with large η are more affected.

Figure 4.3: Beam offset in data is taken into account by changing the perigee parameters with respect to the beam position.

plementation in the *TrackingKal* package the Kalman Fitter was chosen. This method is fast enough in all fitting scenarios and performs well.

Kalman Filter

R.E. Kalman proposed a filter method for signal selection in electrical engineering in 1960 [42]. The principle of this filter can be transferred to a fitter method, the so called *Kalman Fitter*. The fitter only uses the last fit result, which implicitly contains all information of the previous measurements and fits. The last fit result combined together with a new measurement becomes the new reference for the fit. The Kalman Fitter is a progressive fitter because it does not explicitly refer to the previous measurements and can incorporate new measurements step by step without a recalculation of all previous fit results. This fast fitter provides also a quality criteria and suits for the purpose of track fitting.

Basic concept of the Kalman Fitter

Prerequisites of the Kalman Fitter are the possibility to describe the measured quantity as a function and the knowledge of the uncertainty of the measurements. With a linear transport model this information can be propagated to the next measurement and there becomes the new reference. The error of that new estimation is a combination of the lack of information at the previous result and the uncertainty of the propagation. The reference combined together with the measurement by an error weighted mean is the new result and the starting point of the next propagation. By incorporating more and more information the uncertainties are reduced and the errors decrease. More detailed information and examples are given in [43].

The basic assumption of the Kalman Fitter are

- clear sorted structure in one dimension of a measurement set
- linear propagation or transport model
- white and uncorrelated noise
- Gaussian error and noise distributions

Realization for track fitting

For the implementation in the silicon pattern recognition the assumptions of the Kalman Fitter have to be fulfilled.

- The measurements in the silicon detector can be arranged by the radius. Two hits of the same track can not have the same radius, nevertheless they can be in the same layer. The sensors of one layer overlap at the borders and so one track can have two hits there but for the internal use the layers are divided into inner and outer one with different radii. So the measurements can be sorted clearly by the radius.
- The helix trajectory propagation can usually not be described by a linear transformation model but the deviation of the reference is small. With a Taylor Series Expansion of the distance between the reference trajectory and the fitted track, a linear transport model can be generated by dropping negligible terms of higher order. In the fit the deviation is kept small by setting the current fitted track to the new reference trajectory.
- The noise in the detector has to be uncorrelated but can be assumed to be fulfilled because there is no reason for strong correlation between the signal hits and the noise. The small effects of coherent electronic noise or broken strips are negligible.
- The errors of the hit measurement are assumed to be Gaussian due to the clustering method. The mean and the standard deviation of the hit position are calculated with a Gaussian probability density distribution.

The last difference to the basic Kalman filter are the five parameters of the helix trajectory. Instead of determining only one parameter, we have to fit a five dimensional vector and a 5x5 covariance matrix for the uncertainties and correlations. This change of dimensionality of the parameter space is not a fundamental difference and is explained in more detail in [43]. For the internal usage

the covariance matrix is transformed to a weight matrix, which is the inverted covariance matrix. Larger uncertainties have smaller weights and vice versa.

Internal track parametrization

Using a progressive fit method requires a different track parametrization than the one using the perigee because this point is a property of the already finished track helix and can not be determined exactly during reconstruction. All hit measurements in the silicon detector are local positions on a sensor or global positions in the CDF coordinate system. This should be reflected by the parametrization of the fitter to use its full power. It uses the CDF cylindrical coordinates for the position on the helix, the angle β for the direction in the $r\phi$ plane, θ for the direction in z and κ the curvature of the circle, see figure 4.4. These five parameters are called *local* because they are a function of the radius r .

$$track_{local}(r) = (\theta(r), z(r), \beta(r), \phi(r), \kappa(r)) \quad (4.2)$$

The radius dependent parametrization is more complex and every parameter set at each material interaction has to be stored. Therefore this parametrization has no general parameters and is only used internally. After track reconstruction or refitting is finished, this big amount of detailed information is not used anymore. The trajectory helix is converted into the perigee parametrization because storing only five parameters per track is more efficient. These five information are enough for the most physical analyses and all other information can be reproduced.

Fit directions

The progressive fitter incorporates all information during the fit process and therefore the last position measurement of the fit provides the best estimate of the helix parameters. The fit result depends on the starting point and the direction of the linear propagation. So there are two possible directions of the fit, forward or backward.

The *Forward Fit* starts from the innermost measurement outward, in the same flight direction as the charged particle and assumes the origin to be in the beampipe. This fit provides the best track parameter estimation outside the silicon detector, see figure 4.5, and is useful for the extrapolation from the silicon detector to the outer drift chamber or calorimeter cells.

The *Backward Fit* starts at the outermost layer of the silicon detector and collects the hit information inward to the beampipe. So this fit provides the best track parameter estimation at the origin of the particles, see figure 4.6 and are e.g. used for vertexing.

The combination of both fits will be the best estimation of the parameters at any

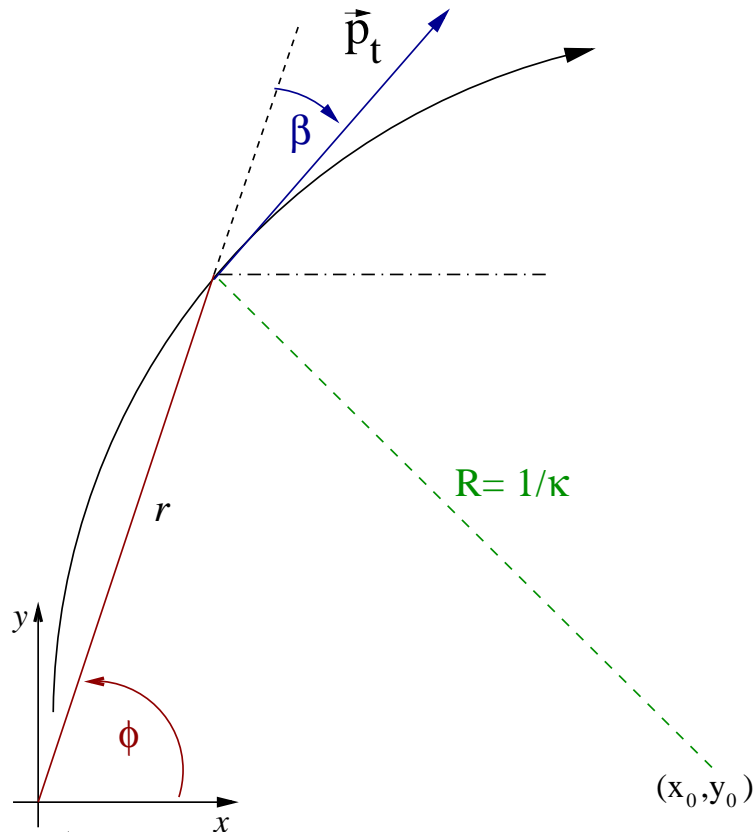


Figure 4.4: Parametrization of a charged particle track in the $r\phi$ plane. The internal parameters of the TrackingKal package are given at any radii and in local coordinates.

radius r_0 . The error weighted mean of the *Forward Fit* from the beampipe up to the radius r_0 and the *Backward Fit* from the outermost measurement up to the same radius r_0 are calculated. The weight matrix is larger and the uncertainties are smaller due to the incorporation of all information in both directions.

4.1.3 Material description

The material in a detector can be divided into active material, which provides measurement information and passive material, which is mainly the support structure of the detector, like cables, cooling lines and mountings. The arrangement of the active material in the silicon detector, the silicon wafers, are done in sublayers, wedges and bulkheads, see table 3.1. The inner and outer wedges of one layer overlap at the borders but they are separated into different sublayers. Each sublayer has a definite radius, which corresponds to the inner or outer wedges. The sorting in ϕ angle is definite per sublayer and also the z position information is unique. For the pattern recognition the hit measurements can

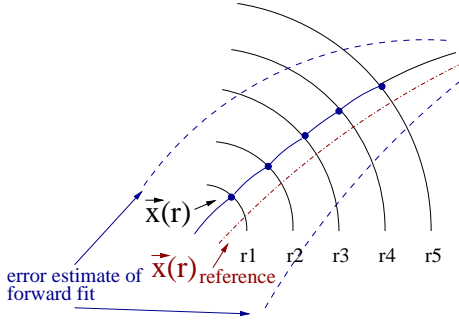


Figure 4.5: The forward fit starts from the innermost measurement and incorporates the information up to the outermost layer. It provides the best parameter estimation outside the silicon and can be used for extrapolation of the track into the outer drift chamber.

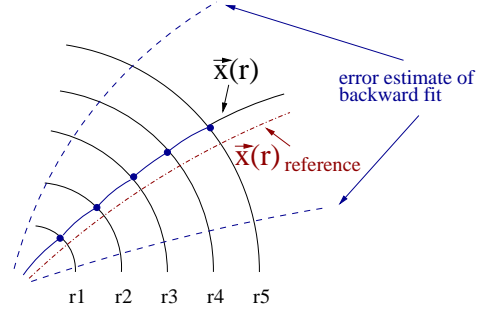


Figure 4.6: The backward fit starts from the outermost measurement and collects information inward. The best parameter estimation is inside the beampipe and is useful for physics analyses.

thus be organized first in r than in ϕ and last in z . This is also the most efficient structure for the fitter and reflects the internal track parametrization. To find the next measurement on the next layer and to calculate the propagation of the reference trajectory to the next intersection are the most time consuming part of the tracking and fitting.

The silicon wafers are not only an active material but also passive. For the fitter all interactions of the particle with the detector material has to be taken into account. The most precise description of the interactions would be done by a *GEANT* simulation with the entire detector geometry. However the large amount of material and the many layers slow down the simulation of the detector response by a detailed material integrator.

For a fast implementation of the estimation of the particle interaction with the detector material, an approximation of the detailed material description is generated. In the *SiliconGeometry* package [44] all detector components of the silicon detector are listed. The track reconstruction of measured data and simulated data use that material description for the fitter. In the *TrackingKal* package an approach to a more detailed description of the silicon detector is achieved by applying additional material and fit layers in the detector description. A sub-layer is built of two measurement layers and one material layer. Additionally to the silicon material, there is also other material in the detector, like the readout electronic or the mountings. The concept of fit layers limits the passive material integration to cylinders between the silicon layers. For the fitter each layer corresponds to a fixed radius and can be sorted by the order of the radius. The intersections of the helix with the material have to be calculated analytically, what limits the possible material description also to cylinders and planes parallel

4.1. BASICS OF TRACK RECONSTRUCTION

to z . The implementation of this method into the TrackingKal package ends up with 74 fit layers of various types in total. A detailed list of all fit layers is given in appendix B.

A GEANT based material integrator was used to calculate all the average material properties for a huge amount of tracks. The detector volume was divided into equidistant ϕ and z bins and for the radius the binning reflects the layer structure. For each of these cells each material property (dE/dx constant, minimal ionization energy and radiation length) is averaged and stored in the so-called *SiliMap*, see figure 4.7. The size of this map can be reduced due to the large symmetry of the detector and identical bins can be stored only once. A detailed description of the SiliMap implementation is presented in [45, 46].

The implementation of the SiliMap material integrator in the TrackingKal packages is used by the Kalman Fitter. Also other silicon track fitters of the CDF II offline software can use the SiliMap due to the 100x faster time performance compared to GEANT while having results of similar resolution.

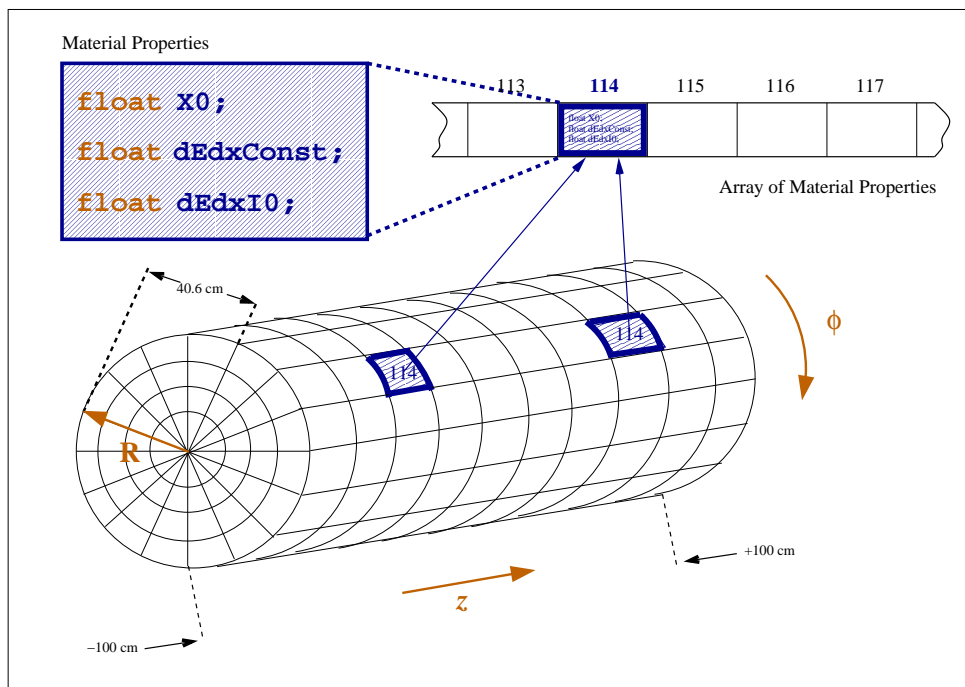


Figure 4.7: The SiliMap is a binned map of the passive material properties. Each map bin holds the index of a description of the average material properties at the position of the bin. Due to the high symmetry of the silicon detector several bins have the same average material properties.

4.2 Tracking strategies

The tracking system of the CDF experiment is built of two different sub-detectors, the drift chamber COT and the silicon detector. The properties of the two detectors are different and therefore each detector type has its own tracking strategies. The tracking algorithm of the drift chamber is the so-called *COT tracking* and the *silicon tracking* defines the tracking algorithm in the silicon detector. For the silicon track reconstruction there are various algorithms with different advantages to provide flexibility and the best overall result. The strategies can be separated into the *silicon-only tracking* and into the *Outside In tracking*. The Outside In tracking uses additional information of the drift chamber to reconstruct tracks and the silicon-only tracking only take measurements of the silicon detector into account. The algorithms of the silicon pattern recognition will be discussed in more detail below and the new silicon track reconstruction strategies of the TrackingKal package will be presented. The order of presentation reflects the sequence of the strategies which is used in the default CDF offline software.

The Tracking strategies are:

- COT Tracking (Drift chamber)
- Outside In Tracking (OI)
- Silicon StandAlone Tracking (SiSA)
- Silicon Forward Tracking (FWD)
- Inside Out Tracking (IO)

COT Tracking: The track density in the drift chamber is lower due to the larger radii and so the tracks are more isolated. As a consequence the reconstruction in the COT can be done faster and with a high purity due to less combinatorics. Also almost no duplicated tracks are constructed. The list of COT tracks provides the first track information of charged particles of the event.

The algorithm can only reconstruct tracks of particles which pass the entire drift chamber. Depending on the detector geometry these tracks are limited to the range which is covered by the entire COT ($|\eta| \leq 1$). Also the transverse momentum of the particle has to be larger than 0.5 GeV/ c to reach the drift chamber due to the curvature of the track. A detailed description of the different tracking algorithms of the COT is given in the references [39, 47, 48, 49].

Outside In Tracking: The pure track list of the COT can be used to perform the first pattern recognition in the silicon detector. These tracks are extrapolated

back into the silicon and along this reference trajectory the hits are searched. This algorithm is called Outside In racking. At CDF II there are two different implementations. One is an extended version of the RUN I algorithm with a generic progressive fitter [50] and the other one is the version of the TrackingKal package which uses the fast Kalman Fitter. Both strategies are used by default. To reduce CPU time and to not duplicate the COT tracks in the OI track list, the second strategy does not use the full silicon hit set. The hits added to a track by the first OI strategy are marked as used and are ignored by the following algorithms. The tracks of the COT can be considered as reasonable and so the algorithm looks for silicon hits belonging to these tracks without further requirements. The OI tracks inherit the good momentum resolution from the long COT tracks $\sigma_{p_t}/p_t^2 \approx 0.15\%$ $(\text{GeV}/c)^{-1}$ and gain the good impact parameter and z-position resolution ($\sigma_{d_0} \approx 10\ \mu\text{m}$, $\sigma_{z_0} \approx 50\ \mu\text{m}$) from the silicon measurements. With COT tracks as seeds the OI tracks have the same requirements for the particle properties ($|\eta| \leq 1$ and $p_t > 0.5\ \text{GeV}/c$). The strategy of the hit search is explained in detail by the example of the OI tracking of the TrackingKal package in section 4.2.1.

Silicon StandAlone Tracking : These tracks are reconstructed only from silicon measurements and do not use any other information. The reference trajectory of a particle track is built by two 3D-Hits and has to be distinguished from any arbitrary hit combination which forms a fake track. To reduce combinatorics and duplicated tracks only unused hits can build a track candidate. A detailed description is given in section 4.2.2. This algorithm reconstructs tracks within the full coverage of the silicon detector $|\eta| \leq 2$ and is mainly used in forward direction. Low momentum tracks ($p_t > 0.2\ \text{GeV}/c$) do not reach the drift chamber but can be reconstructed by the SiSA strategy. Also inefficiencies of the OI tracking in the central region can be compensated. The requirement of two 3D-Hits out of four possible layers is a limitation on the acceptance of the working detector. As seen in figure 3.25 there are many holes in the coverage of the SAS layers which results in inefficiencies. The next strategy tries to compensate for this effect.

Silicon Forward Tracking : This algorithm is similar to the *Silicon StandAlone Tracking* but relax the requirement of two 3D-Hits. The reference trajectory is only built of one 3D-Hit and one $r\phi$ hit. The second needed z information is taken from already reconstructed z vertices. The higher combinatorics requires a better preselection and harder acceptance criteria. Also the minimum transverse momentum is chosen to be larger ($p_t > 0.8\ \text{GeV}/c$ in default reconstruction) in order to reach an acceptable CPU time usage, see figure 4.13. A detailed description of the strategy is given in section 4.2.3.

Inside Out Tracking : The last strategy in the track reconstruction chain extrapolates the silicon tracks into the drift chamber. If SiSA and FWD tracks

point to segments of the COT, additional information can improve these tracks. The IO strategy forms tracks with silicon and COT measurements which are similar to the OI tracks [51]. The momentum resolution of these tracks is better than the silicon-only tracks due to additional measurements and increased track length. The confirmation of the silicon tracks by COT information also decreases the fake rate because a silicon track of a charged particle which points to a drift chamber segment must also have measurements there.

4.2.1 Outside In Tracking

Search road: The OI strategy uses a COT track as a reference trajectory which is extrapolated into the silicon detector. The position at the outermost intersecting layer of the silicon is calculated from the parameters of the COT track. The hits are searched for in a three to eight standard deviations large window. This search window is limited to a maximal size due to an underdefined covariance matrix or too large errors. All hits in the search window which pass the quality criteria are considered as belonging to the track. Only one hit of them can be the true representation of the energy deposit of the particle. All other hits do not belong to the track but it is not possible to distinguish between them. So for each possibility the reference track is copied and the corresponding hit is added. Also the original reference track without added hit is kept, because none of them might be correct or the correct hit was not reconstructed due to inefficiencies of the silicon detector. This method is called cloning and ends up with a list of possible track candidates. These candidates are fitted with the Kalman Fitter and the resulting parameters are used to extrapolate the track to the next measurement layer. For each candidate the next hit search is performed at that intersection position in the next measurement layer and so the clones are branched up. This procedure is repeated till the innermost layer is reached. Depending on the event type there are up to 200 COT seed tracks. An illustrated example is given in figure 4.8 with two possible hits in the outermost layer and the three resulting clones.

Choose best clone : Two criteria select the best track from the many possible clones. The number of picked up hits is a quantity of the added information and the χ^2 per degree of freedom (*dof*) defines the goodness of the clone fit. A particle deposits energy in each interacting layer and therefore in all active measurement layers a hit should be reconstructed. A track candidate has to find these hits and so the fraction of found hits over the passed active measurement layers reflects its quality. Not all clones are pursued till the innermost layer due to that failed quality criterion.

Loop structure : The structure of the different layers with a unique radius would allow to search all different hit types in one pass, what worked well in simulations

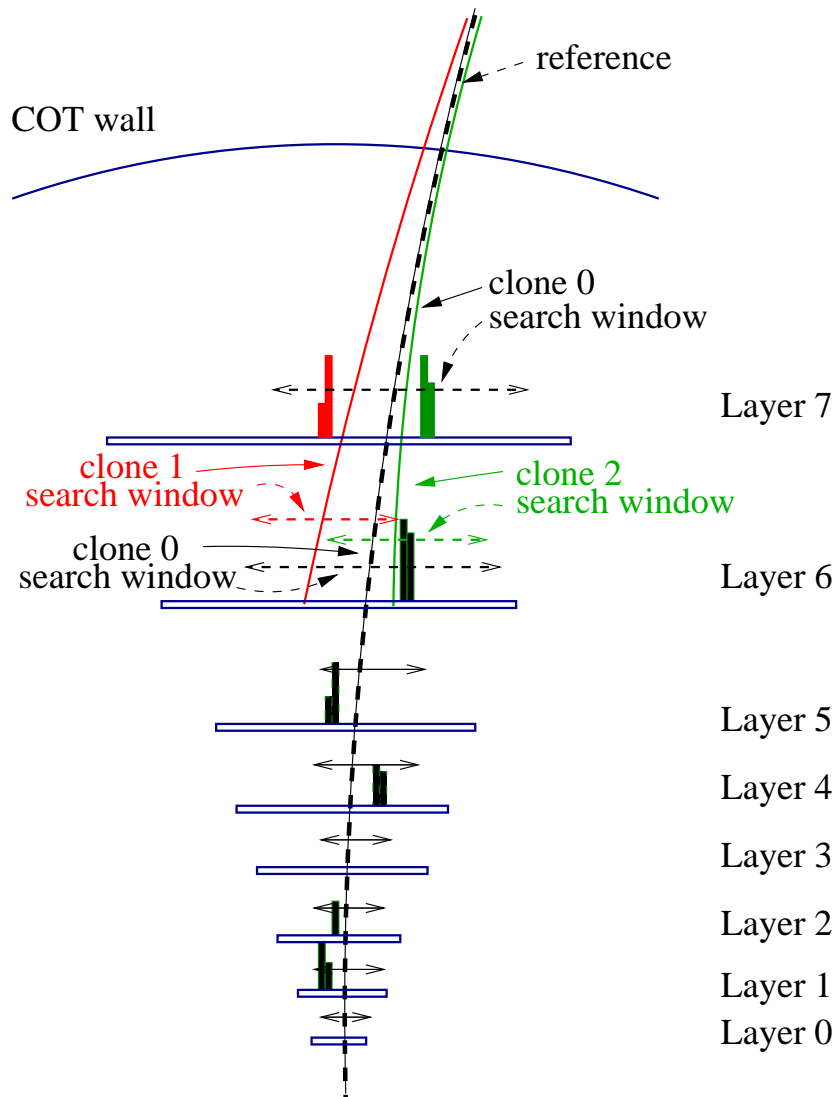


Figure 4.8: A illustration of the hit search along a reference trajectory. For each possible hit, the track is copied, fitted and extrapolated to the next measurement layer. This procedure is continued till the innermost layer is reached.

with a perfectly aligned detector. Applying this method on measured data does not work optimal due to some misalignment in the silicon detector. Doing the hit search for each hit type separately is much more robust. So first only axial measurements are searched and at least three have to be found to form a silicon OI track in the $r\phi$ plane. This is the new reference trajectory for the search of stereo hits, which is performed in the same way as for the ϕ hits. If additional stereo information are found, the resulting track becomes the new reference but there is no requirement of a SAS hit. Also the last iteration for the z hit search is done similarly but no z hit is required [43].

The OI strategy of the TrackingKal is performed in these three loops and is called KalOISVX3LoopTracker. At least three $r\phi$ hits have to be added to the seed COT track to become an OI track. With no additional silicon stereo or z hits the z resolution of an OI track depends only on the COT resolution in z .

4.2.2 Silicon StandAlone Tracking

The Silicon StandAlone strategy is a silicon-only algorithm, no further information from other detector components is used. No reference trajectory exists and the seed helix has to be built by the algorithm itself. To determine the five parameters of a helix, three measurements in the $r\phi$ plane and two measurements in the rz plane are needed.

Hit type : Creating any arbitrary combination of three axial hits for the determination of the $r\phi$ parameters (d_0 , C , ϕ_0) is principally possible but would result in too large combinatorics. Most of them would be a wrong seed with no real physical representation. Adding z information independently will also increase the fake rate. The best starting point clearly would be identified positions of a track in all three dimensions. A 3D-Hit is a clear combination of a ϕ and a *stereo* measurement in the SAS layers and both hits confirm each other. These hits also have a definite z measurement. If two 3D-Hits are used for the determination of the helix only one additional information in the $r\phi$ plane is required.

Used hits : The chain of track reconstruction strategies should work exclusively and already found silicon tracks should not be found again by a following algorithm. Therefore the hits added to a track are marked as used and will be ignored later. SISA tracking uses this flag to build the reference track only with unused hits and skips a 3D-Hit if its stereo or ϕ hit is already incorporated to an existing track fit.

Seed Track : Two 3D-Hits from different layers, together with the beam line position, form the seed trajectory. The accurate beam position is reconstructed

from previous events and is used for the reference. The beam position information is not incorporated into any fit and so it enters not as a measurement. This algorithm requires two 3D-Hits out of four layers. A particle which energy deposits in the silicon detector can not be reconstructed to a 3D-Hit, can not be found by this strategy. The efficiency of the algorithm is strongly correlated to the detector acceptance. A starting point of an algorithm with looser requirements can recover these inefficiencies and is used by the FWD strategy.

Reduction of arbitrary combinatorics : A reduction of the combinatorics is done by a weak cut on the ϕ region of the chosen hits which has to be consistent within $\Delta\phi = \pm\pi/20$ and corresponds to $p_t > 0.1$ GeV/ c . This is shown in figure 4.9. There are still up to 100.000 of these hit combinations and most of them do not describe a possible track candidate for a particle. The calculation of the helix parameters consume CPU time and should not be done for fake track-candidates. The information of the rz positions of the starting 3D-Hits can be used for a further selection of reasonable track candidates.

The origin of the track should be compatible with the z positions of the primary interaction in the event. Therefore a straight line of the rz points is constructed and the position at the accurate beam line has to be consistent with the z position of the primary vertex within ± 5 cm, see figure 4.10. The consistency check of the z position leads to a further reduction of the fake seeds but requires at least one reconstructed primary vertex. First, there is a pre-tracking primary vertex finder implemented in the TrackingKal package which is based on COT information and the seed tracks themselves [52]. Additionally, a second algorithm calculates possible z positions of the primary vertex by using COT and OI tracks. Most of the vertices found by the first algorithm are confirmed by the second which provides also a quality criterion of the reconstructed vertices [53, 54]. Without any reconstructed vertex this strategy can not find any track and so the inefficiency of the vertexing is strongly correlated to the tracking efficiency.

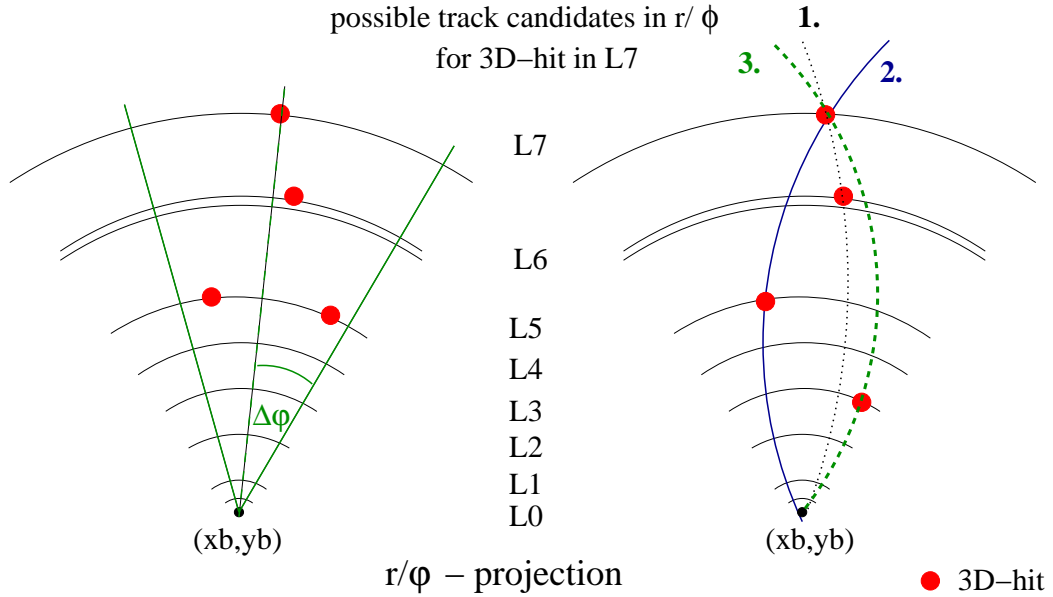


Figure 4.9: Construction of the reference trajectory in $r\phi$. All combinations of two 3D-Hits in a small ϕ segment with the beam position are used to construct a seed track for reconstruction.

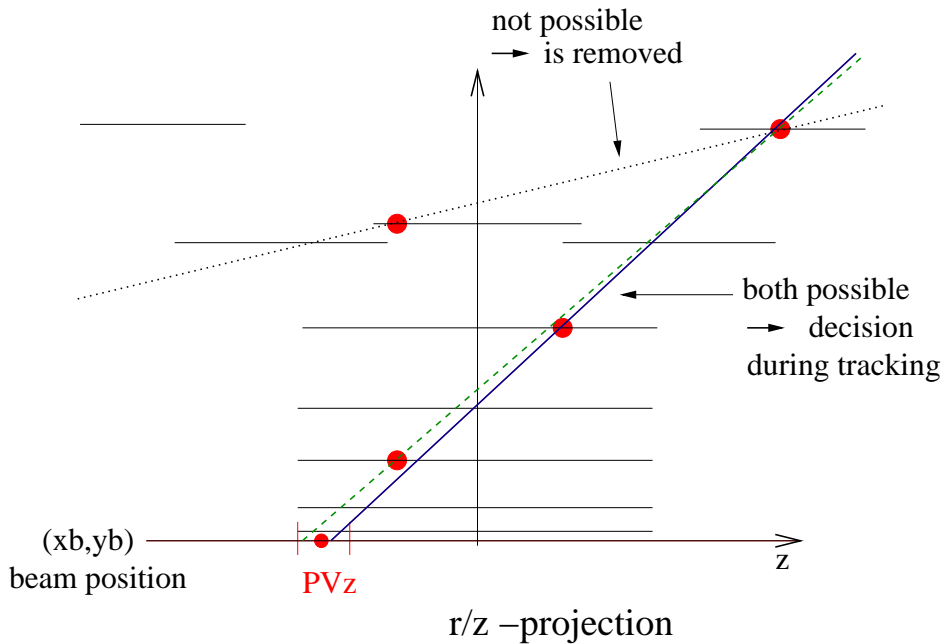


Figure 4.10: Construction of the reference trajectory in rz . The seed track in $r\phi$ has to be consistent with the z position of the primary vertex.

Candidates : If a seed trajectory is selected by the algorithm above, it is worth to determine the full parameter set of the helix for this possible track candidate. To reduce the large combinatorics of the seed candidates and to remove fake tracks, the helix parameters are used for a further seed track selection. The description with the helix parameters are more accurate and so z_0 has to be consistent with a primary vertex within ± 1.6 cm. The seed hits have to pass an η depending charge cut, $Q_{hit}/\sin(\theta) > 20$ ADC, to remove candidates built from noise hits. The hit charge function of η reflects the energy deposit along the pathlength of the particle through the silicon sensor.

Ranking of the seed tracks : The hit search for the now given reference tracks is performed in the same way as in the OI tracking, with the candidates instead of the COT tracks. The track candidates are sorted by their resolution to start with the best track. First the seeds built from 3D-Hits in LAYER 3 and LAYER 5 are processed the shortest distance to the beam and the best z resolution. Then the hit combinations from LAYER 3 and LAYER 6, followed by LAYER 5 and LAYER 6 and at last all LAYER 7 candidates are reconstructed. Another selection criteria is the transverse momentum where high momentum tracks are preferred. If a candidate is accepted as a track after the hit search was performed, all the associated hits are marked as used. This prevents duplicated tracks because the hits of each candidate has been checked against used hits. A reference track is removed if a seed hit has been used already. To find the best tracks first, the following quality requirement is applied many times. In the first iteration a track must have at least in 80% of the active layers a reconstructed hit, the second only 60% and in the last iteration only 40%. The tuning parameters for this strategy are listed in appendix C.

Summary : The SISA strategy can find tracks up to $|\eta| \leq 2$ and with a minimum transverse momentum of $0.2 \text{ GeV}/c$ and a resolution of $\sigma_{p_t}/p_t^2 \approx 0.4 \% (\text{GeV}/c)^{-1}$. Running after the OI algorithm and incorporating only unused hits, the main usage is in forward direction. The requirement of minimum two 3D-Hits out of four possible SAS layers results in some inefficiencies of the imperfect detector. This can be compensated by the following strategy which loosens this requirement.

4.2.3 Silicon Forward Tracking

The last strategy of the TrackingKal package which runs in the default reconstruction chain is the *Silicon Forward Tracking*. The algorithm is similar to the *Silicon StandAlone Tracking* and also uses only silicon information. This section explains the main differences between these two strategies. It does not repeat

the details which are equivalent to the SISA strategy. The reference trajectory again is built from silicon hit measurements but the requirements are looser than in the SISA strategy to compensate the inefficiency of the detector acceptance. The five parameters of the helix are determined again by three $r\phi$ and two rz information.

Seed Track : The main improvement of this strategy is the loose requirement of only one 3D-Hit in contrast to the Silicon StandAlone Strategy which requires at least two of them. This algorithm builds the seed track with one 3D-Hit, the beam line, a $r\phi$ hit and the z position of a reconstructed vertex instead of a second 3D-Hit. Therefore the primary vertices have to be reconstructed first and a certain quality requirement has to be fulfilled. The z vertices in the *ZVertex-Module* are determined by the following algorithm. A list of pre-tracking vertices which have high efficiency but also a high fake rate, is cleaned up by confirmation by reconstructed tracks. A certain number of tracks with $p_t > 0.3$ GeV/ c have to be associated to a vertex and have to be consistent within 1 cm (5 cm) of silicon vertices (COT standalone vertices). The z position of the vertex is the error weighted mean of their z_0 parameters. The beam position in the $r\phi$ plane is corrected at the corresponding z position with the slope of the beam line. These information are used to construct a reference but are not incorporated as a measurement.

Reduction of arbitrary combinatorics : The combinatorics in this algorithm is much larger than in the SISA strategy due to the weaker requirements. The axial hit and the 3D-Hit have to be in a ϕ region within $\Delta\phi = \pm\pi/20$ which corresponds to a first weak cut of $p_t > 0.1$ GeV/ c . Already using the z position of the vertex for the construction of the seed, it can not be used for the reduction of the fake tracks. The $r\phi$ hit itself has no z measurement but it has to be within the range of the sensor. The vertex position has to be consistent within the range, covered by both straight lines from the 3D-Hit to the borders of the halfadder, see figure 4.11. This reduces the most unlikely combinations.

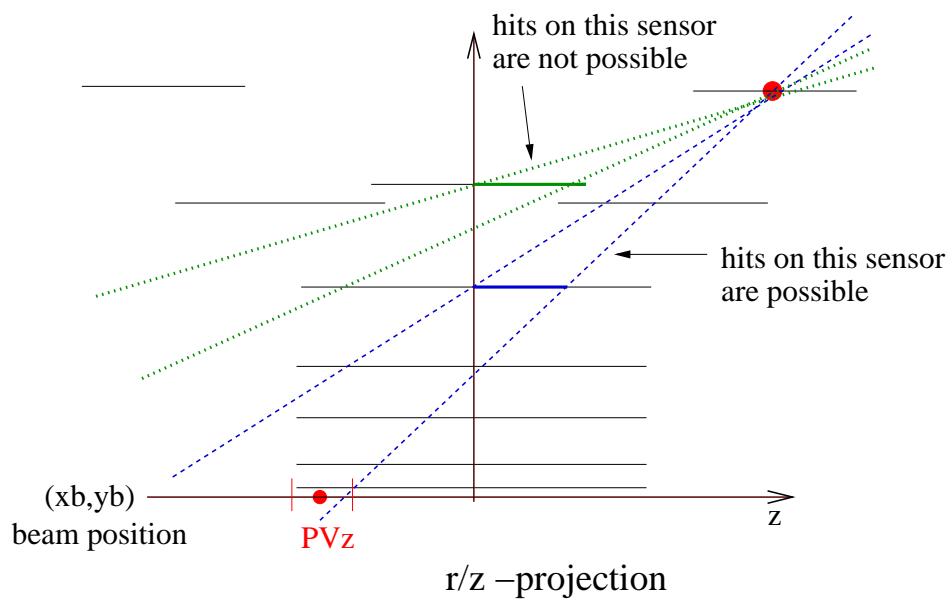


Figure 4.11: Construction of the reference trajectory in rz . The sensor position in z of the $r\phi$ hit has to be consistent with the primary vertex. The hit has no z information itself but has to be on an intersecting halfadder. With this requirement some arbitrary combinatorics can be removed.

For one 3D-Hit and several axial hits of a particle trajectory multiple seed tracks can be built. To minimize this ambiguity and reduce the combinatorics, the $r\phi$ hit is required to be on a layer inside the layer of the 3D-Hit.

To perform the tracking in an reasonable CPU time, some transverse momentum cuts are applied to the preliminary momentum of the seed helix. As the default configuration has to reconstruct all events in an acceptable time, minimum p_t is chosen to be 0.8 GeV/ c . A cut on the maximum p_t is also defined ($p_t < 500$ GeV/ c) which is of no consequence for tracks of particles. In section 4.3 the timing performances of different momentum cuts are presented.

The largest effect is achieved by incorporating only unused hits. This algorithm should recover the inefficiencies of the previous ones and not do the entire track reconstruction. So the main usage will be in the forward and far forward region, like SISA, because tracks in the central region are already reconstructed by other strategies.

Candidates : The three $r\phi$ and the two rz information are used to construct the reference helix for the hit search. Only an η depending charge cut for the hits, $Q_{hit}/\sin(\theta) > 20$ ADC, can be applied to remove candidates built from noise hits.

Ranking of the seed tracks : The first sorting criterion is the layer of the 3D-Hit, the second the transverse momentum p_t of the reference track. The track has no real z resolution due to only one z measurement. The longer track length of the seeds with a 3D-Hit in the outer layer reduces the sensitivity to misalignment and the relative errors of the reference parameters. Additionally the probability for finding a corresponding axial hit to a 3D-Hit is larger in the outer layers. If the 3D-Hit is in LAYER 3 for example, the axial hit has to be in LAYER 1 or LAYER 2. So the reference trajectories of 3D-Hits in LAYER 7 are preferred over LAYER 6, LAYER 5 and LAYER 3.

Summary : The FWD strategy can find tracks up to $|\eta| \leq 2$ and with a minimum transverse momentum of 0.8 GeV/ c and a resolution $\sigma_{p_t}/p_t^2 \approx 0.5\%$ (GeV/ c) $^{-1}$. The algorithm recovers some inefficiencies of the SISA strategy by starting with only one 3D-Hit. Running last and incorporating only unused hits, the main usage is in forward direction. The loose starting requirement results in a very large combinatorics, which has to be reduced. The selection criteria are harder to reduce fake tracks.

The tuning parameters for this strategy are listed in appendix C.

4.2.4 Inside Out Tracking

This strategy extrapolates tracks reconstructed with the SISA and FWD algorithms into the drift chamber and incorporates further hit information if avail-

able. Tracks from particles which do not traverse the entire drift chamber can not be found by the COT tracking. The hit positions of these particles, usually in the innermost COT layers, can improve the silicon-only track. The geometrical acceptance of the drift chamber in forward direction and the efficiency of the silicon-only tracking results in a coverage of $\approx 1.1 \leq |\eta| \leq 1.7$ for the IO tracks.

Algorithm : The tracks reconstructed with the silicon-only strategies are fitted outward with the Kalman Fitter which delivers the best parameter estimation at the inner COT wall. These helix parameters form the reference trajectory for an outward hit search in the drift chamber. The COT hits are fitted to a COT track without any silicon information. After this process it is treated like an OI algorithm and the COT track is fitted together with the silicon hits of the former seed track by an inward Kalman-fit. This fit results in the best estimate of the perigee parameters and their covariance matrix.

4.3 Performance of the strategies

In this section the performances of both new silicon strategies are studied. In order to be used in the official reconstruction software of CDF II the CPU time consumption of the new strategy has to be of the same order as the other strategies. The computing time depends directly on the combinatorics of the seed track candidates. Also the efficiencies of the track reconstruction strategies have to be studied. In this section simulations are used for this. The efficiency of the silicon-only strategies are also determined with measured data and presented in the next chapter 5.2.

4.3.1 Combinatorics of the seed tracks

The new *Silicon Forward* track reconstruction strategy should compensate the inefficiencies of the other algorithms. Therefore the requirements of the seed trajectory are less tight which result in a large number of possible track candidates.

To visualise the high combinatorics of the silicon-only strategy the number of seed track candidates and the number of reconstructed tracks are shown in figure 4.12. Four datasets represent different event types, two in the simulation and two in measured data.

In the simulation of $Z^0 \rightarrow \mu\mu$ ($ztop0i$), see figure 4.12 a) and $Z^0 \rightarrow ee$ ($zewkae$), see figure 4.12 b), an underlying event is added to the simulated Z^0 boson decay, to reflect a typical collision event in the detector with all other decaying and scattering particles. Such an underlying event to a simulated event is called a minimum bias event. Nevertheless there is only a low silicon detector occupancy which results in a low combinatorics of the seed candidates. The SISA strategy

starts the track reconstruction with up to 1000 seed candidates. In the same events the FWD strategy builds up to 2000 seed candidates due to the loose requirement of only one reconstructed 3D-Hit instead of two 3D-Hits.

The track number distribution of the dataset *ptop00* in figure 4.13 c) contains reconstructed events with at least one high energetic electron in forward direction. Figure 4.13 d) shows the distribution of the number of tracks and seed candidates of the dataset *jpmm0d* which contains events with at least two muons, forming the J/Ψ mass. Both distributions of the number of seed candidates have shapes with very long tails up to 12000 candidates. The presented range is according to the plots of the simulated datasets and therefore only a part of the distribution is shown. The large mean value illustrate the high combinatorics in measured data, which is much larger than expected from simulation. The reason for this might be a much higher noise rate, compared to the simulation. In table 4.1 all numbers of the different datasets and strategies are compared to each other.

All seed candidates have to be processed by the tracking strategy. Along their reference helices the hit search is performed. This search is the most time consuming part of the track reconstruction.

	dataset	tracks		candidates	
		SiSA	FWD	SiSA	FWD
simulation	zewkae	10	2	87	303
	ztop0i	11	3	120	415
data	ptop00	19	13	1585	3495
	jpmm0d	22	15	1177	3910

Table 4.1: The average number of the reconstructed tracks and seed candidates of the silicon-only strategies. 3000 events of each dataset were reconstructed and the average number of tracks and candidates are calculated. In the measured datasets there are huge numbers of candidates which are used to reconstruct tracks. The huge amount of track seeds is the result of a much higher combinatorics of silicon hits compared to the simulation.

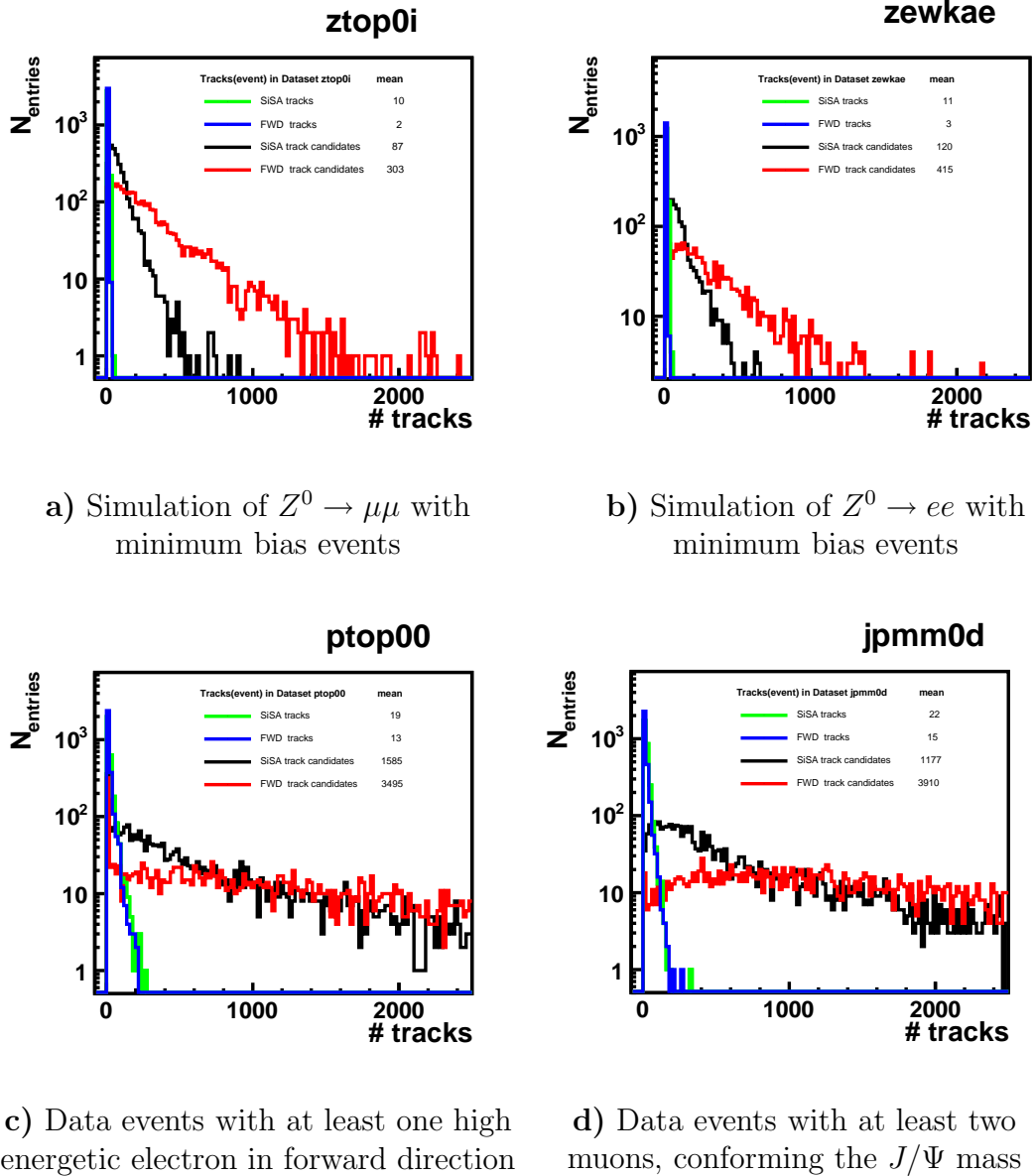


Figure 4.12: Number of the reconstructed tracks and seed candidates per event from 3000 reconstructed events. The SiSA tracking strategies form up to 1000 seed tracks per event in the simulation. The FWD strategy builds up to 2000 seed candidates, both can be seen in a) and b). In data the number of candidates of both tracking strategies is observed to be much larger, up to 12000. Only a part of the very long tail of the distribution is shown in the plot. The calculated mean of the data distributions reflects the enormous increase in the combinatorics of the silicon hits, which form the seed candidates, compared to the simulation.

4.3.2 Time performance of the silicon tracking

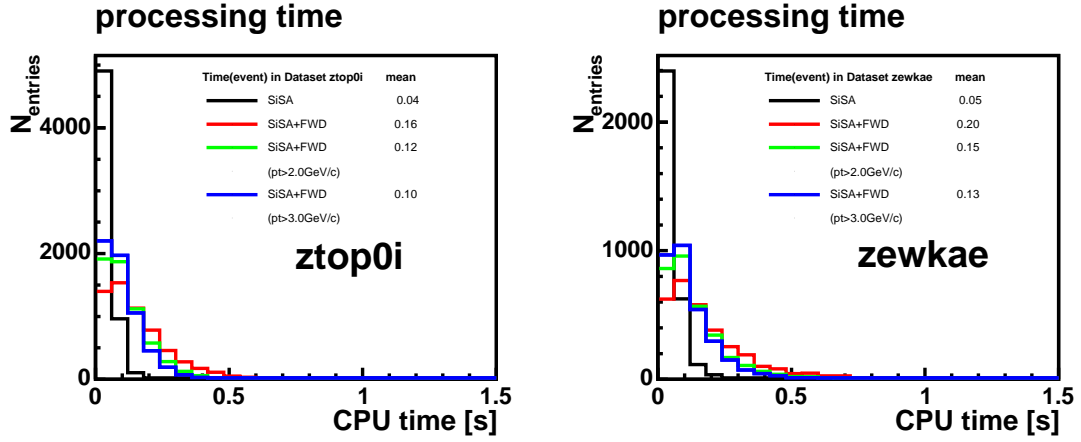
A reasonable CPU time performance is important for all track reconstruction strategies. The implementation of the fast Kalman Fitter combined together with the object oriented programming language *C++* has enabled an entire chain of silicon pattern recognition algorithms. To run in the chain of the official reconstruction software of CDF II the new FWD strategy has to consume CPU time in a comparable way to SiSA strategy. A momentum cut on the reconstructed tracks is implemented in the algorithm and is used for the reduction of the seed candidates.

All the plots 4.13 a) - d) show the distribution of the CPU time consumption of the silicon strategies per event. To optimize the value of the requirement of a minimal transverse momentum, the FWD strategy was performed several times with different cut values. To study the time performance in events with different characteristics, various datasets are used. Two examples of simulated data and two examples of measured data are shown and described below.

In the simulation of $Z^0 \rightarrow \mu\mu$ (*ztop0i*), see figure 4.13 a) and $Z^0 \rightarrow ee$ (*zewkae*), see figure 4.13 b), the FWD strategy consumes a similar amount of time compared to the SiSA algorithm. No long tails of the time distribution are visible due to the low combinatorics of the seed candidates, see figures 4.12 a) and b). Both the CPU-time distributions of dataset *ptop00* in figure 4.13 c) and of dataset *jpmm0d* in figure 4.13 d) have both long tails which contain events of high combinatorics. Most events can be reconstructed fast by the SiSA algorithm due to the lower combinatorics, which is shown in the figures 4.12 c) and d). Some of the events which can be processed fast have low combinatorics due to inefficiencies which can be compensated by the FWD strategy. The much higher number of seed candidates of the FWD strategy results in a longer consumption of CPU time.

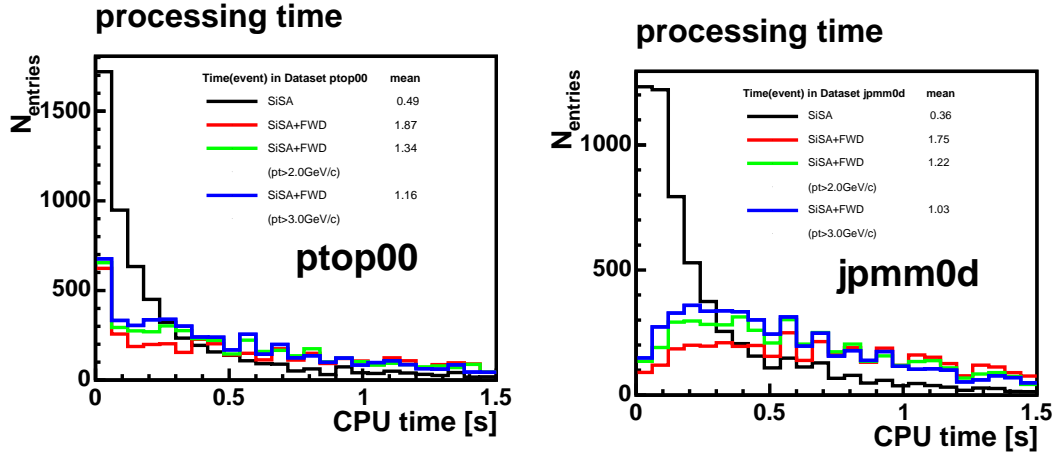
The mean of these distributions determines the average computing times of the silicon-only strategies per event. In total the FWD tracking with a momentum cut larger than 3.0 GeV/*c* takes twice as long as the SiSA strategy, the default $p_t > 0.8$ GeV/*c* cut up to three times longer, see table 4.2. But the silicon track reconstruction is only one part of the entire event reconstruction. The average CPU time consumed for a total event reconstruction is listed in the table 4.3. With the new silicon-only strategies the event reconstruction takes more time, up to twice as long. Therefore the lowest possible value with a reasonable time consumption of the event reconstruction has been chosen as the new momentum requirement.

4.3. PERFORMANCE OF THE STRATEGIES



a) Simulation of $Z^0 \rightarrow \mu\mu$ with minimum bias events.

b) Simulation of $Z^0 \rightarrow ee$ with minimum bias events.



c) Data events with at least one high energetic electron in forward direction.

d) Data events with at least two muons, conforming the J/Ψ mass.

Figure 4.13: CPU time consumption of different datasets: Almost no noise and low occupancy of the silicon detector results in a low combinatorics in the simulated events a) and b). Both silicon pattern recognition strategies show no tails of high CPU time consuming events. The shape in the data plots c) and d) are different. There are long tails from events with a high combinatorics which increase extremely for the FWD strategy. Some of the fast events in the SISA strategy are dominated by the inefficiency which can be compensated by FWD. The reconstruction software was running on a computer system with an AMD Athlon MP 2800+ CPU.

4.3. PERFORMANCE OF THE STRATEGIES

CPU time in sec	dataset	SiSA	SiSA+FWD	SiSA+FWD	SiSA+FWD
				$p_t > 2.0 \text{ GeV}/c$	$p_t > 3.0 \text{ GeV}/c$
simulation	zewkae	0.05	0.20	0.15	0.13
	ztop0i	0.04	0.16	0.12	0.10
data	ptop00	0.49	1.87	1.34	1.16
	jpmm0d	0.36	1.75	1.22	1.03

Table 4.2: The CPU time consumption in seconds of the silicon-only strategies is averaged over 3000 events. Compared to the SiSA strategy the additional time of FWD tracking is up to a factor three slower, depending on the momentum cut. The reconstruction software was running on a computer system with an AMD Athlon MP 2800+ CPU.

CPU time per event in sec	dataset	complete event reconstruction with			
		SiSA	SiSA+FWD	SiSA+FWD $p_t > 2.0 \text{ GeV}/c$	SiSA+FWD $p_t > 3.0 \text{ GeV}/c$
simulation	zewkae	0.77	0.93	0.87	0.85
	ztop0i	0.69	0.81	0.77	0.75
data	ptop00	1.65	3.08	2.54	2.35
	jpmm0d	1.60	2.94	2.43	2.24

Table 4.3: The CPU time consumption in seconds per event is averaged over 3000 events and show the effect in time of the additional FWD. The reconstruction software was running on a computer system with an AMD Athlon MP 2800+ CPU.

4.3.3 Track reconstruction efficiency in the simulation

Efficiency can be defined in many ways. A possibility of the definition of efficiency can be the ratio of reconstructed tracks to the particle tracks which fulfill the minimum requirements of the strategy and therefore can be defined as findable.

To determine the denominator information of the simulated particles is used. In this efficiency study a simulated particle track is defined as findable if at least five hits can be reconstructed in the silicon detector and the transverse momentum of the particle is larger than $0.2 \text{ GeV}/c$.

The numerator of the efficiency is the number of tracks which are reconstructed by the several strategies and can be matched to a simulated particle track. The matching of both tracks is performed with the track parameters which have to be consistent within small windows in $|\Delta\phi| < 0.1$, $|\Delta z| < 0.5$, $|\Delta d_0| < 0.2$, $|\Delta\text{curvature}| < 0.005$ and $|\Delta\text{cotan}(\theta)| < 0.1$.

The efficiency can be calculated for each tracking strategy separately. In figure 4.14 the efficiencies of all strategies and their combination are presented. Due to the exclusive track reconstruction chain of the several strategies, one reconstructed track can not be found by another strategy. As a consequence the sequence determine each fraction of the total efficiency. Therefore the Outside In strategy, running first, reconstruct almost all tracks in the central region. The subsequent SISA and FWD strategies provide track reconstruction in the forward region. In the central region the silicon-only tracks have to be extended into the drift chamber and are visible as Inside Out tracks. In the range $|\eta| < 1$ the IO tracks are low momentum tracks which do not traverse the entire COT. Both new silicon-only strategies increase the η range of the track reconstruction up to 2.5. A tracking efficiency of over 50% is achieved up to $|\eta| < 2$ compared to the previous efficiency of 10% at $|\eta| = 2$.

4.3.4 Summary

The efficiency in the forward region at $|\eta| = 2$ could be increased from 10% to over 50% in the simulation. The overall performance of the silicon-only strategies is improved. The new FWD strategy enables track reconstruction in the silicon detector up to $|\eta| = 2.5$.

The tuning of the momentum cut of the FWD algorithm reduces the combinatorics of the seed candidates which results in a reasonable CPU time consumption. All presented tracking strategies are implemented in the offline software of CDF II and are part of the next official data reconstruction.

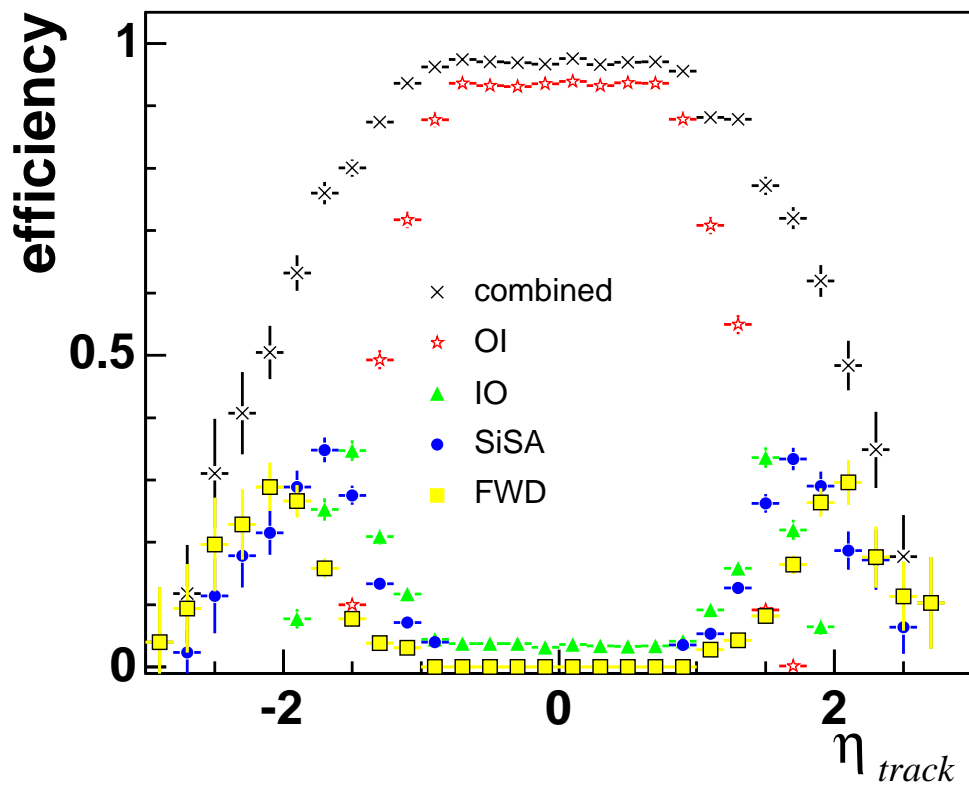


Figure 4.14: Efficiency of the various tracking strategies and their combination versus η .

Chapter 5

Performance of the Forward Tracking using CDF data

To validate the new tracking strategies in forward direction, the new tracks are used in the reconstruction of the invariant di-lepton mass. The leptonic decay of the Z^0 boson provides a clear signal of two isolated high- p_t tracks which can be identified and used for the evaluation of the track reconstruction efficiency. The only difference in the experimental signature between e^- and e^+ or μ^- and μ^+ is the sign of the curvature of their tracks. Therefore in this thesis the term *electron* resp. *muon* is used for both, the particle and the anti-particle. A reconstructed electron contains an isolated energy measurement in the calorimeter and a matched track of any tracking strategy. The reconstructed muons are defined similarly by a measurement in a muon chamber and an associated track. The event selection of the leptonic Z^0 decay is described. The invariant mass of a central lepton and a second lepton of the same family with opposite charge is reconstructed. The improvement of the track reconstruction efficiency is shown by the example of forward electrons. The studies of the di-lepton mass distribution in this thesis are done to validate the performance of the silicon-only track reconstruction strategies by an increase of the total number in the mass peak.

5.1 Used data samples

Depending on the various detector components and their possibility to measure different particle properties, the collision events are already divided into several data streams by the trigger. Each stream splits also up into so-called trigger paths which select events with specific characteristics [55, 56].

The datasets `bhe10d`, `bhe10h` and `bhe10i` contain all events from the trigger path for central high- p_t electrons, `ELECTRON_CENTRAL_18`.

The transverse energy E_t of a calorimeter is defined as $E_t = E_{em} \cdot \sin \theta$, where θ is the polar angle of corresponding track or if no track information available

the polar angle of the detector cell itself. Without a track, the origin of the measured particle is assumed to be in (0,0) and therefore the detector angle allows a rough estimate of the transverse component E_t of the measured energy, which is often called *detector- E_t* .

ELECTRON_CENTRAL_18

- *Level1* : L1_CEM8_PT8
The requirements are at least one deposition of energy in the central calorimeter with detector- $E_t > 8$ GeV, a hadronic to electromagnetic energy ratio (HAD/EM) < 0.125 and one found XFT track with $p_t > 8.34$ GeV/c.
- *Level2* : L2_CEM16_PT8
At least one energy deposition in the central calorimeter must have an energy $E_t > 16$ GeV and its cluster centroid is located in $|\eta| < 1.317$. So the cluster is located in the central part of the calorimeter. The found COT track at Level 1 has to be matched to the cluster.
- *Level3* : L3_ELECTRON_CENTRAL_18
The matched track is used to recalculate the preliminary E_t of the detector to a more exactly E_t of the electromagnetic cluster, which has to be larger than 18 GeV. The track p_t has to be larger than 9 GeV/c. Level3 also adds a cut on the lateral shower profile (Lshr) of the electromagnetic cluster. This quantity describes the comparison of the measurement to the shower profile of an ideal electron in the detector.

The datasets `bhmu0d`, `bhmu0h` and `bhmu0i` contain events of the two trigger paths for high- p_t muons. The MUON_CMUP18 trigger path utilizes information from both the CMU and the CMP detector systems. Muons found in the CMX detector are in the MUON_CMX18 trigger path.

MUON_CMUP18

- *Level1* : L1_CMUP6_PT4
The requirement is at least one muon track segment in the CMU detector having $p_t > 6$ GeV/c and an additional consistent track segment in the CMP detector. A track in the COT with $p_t > 4.09$ GeV/c has to be found and matched to the track segment. A track segment of a muon chamber can also be called stub in the jargon of CDF II .

- *Level2* : L2_TRK8_L1_CMUP6_PT4
The track found in the COT must have $p_t > 8$ GeV/ c .
- *Level3* : L3_MUON_CMUP_18
The track has to match to the muon stub in a window of $r - \Delta\phi_r$ in the CMU less than 20 cm and in the CMP less than 10 cm.

MUON_CMX18

- *Level1* : L1_CMX6_PT8_CSX
The requirement is at least a muon stub in the CMX detector having $p_t > 6$ GeV/ c and consistent hits in the CSX detector. Also a track passing through at least 4 layers of the COT detector with $p_t > 8.34$ GeV/ c is required to correspond to the muon stub.
- *Level2* : L2_AUTO_L1_CMX6_PT8_CSX
In this level no additional requirements are set and all events are accepted automatically.
- *Level3* : MUON_CMX18
The track found in the COT has to match to the CMX stub in a window of $r - \Delta\phi_r$ of less than 10 cm and requires a $p_t > 18$ GeV/ c .

Each dataset represents a different time period in which the data are collected. In table 5.1 the run range, date of data taking, integrated luminosity and number of events of the datasets are presented.

These datasets are a rough preselection of events with similar properties. For a physics analysis the interesting events have to be extracted by a more sophisticated selection.

	Dataset	first run	date	last run	date	$\int Ldt$ [pb ⁻¹]	events
<i>electron</i>	bhel0d	138425	02/04/02	186598	08/22/04	333	26499559
	bhel0h	190697	12/07/04	203799	09/04/05	363	20026640
	bhel0i	203819	09/05/05	212133	02/22/06	258	28775269
<i>muon</i>	bhmu0d	138425	02/04/02	186598	08/22/04	333	6629079
	bhmu0h	190697	12/07/04	203799	09/04/05	363	5769255
	bhmu0i	203819	09/05/05	212133	02/22/06	258	8760406

Table 5.1: Used data samples with run range, date of data taking, integrated luminosity and number of events contained in each sample.

5.1.1 Event selection

The characteristics of the leptonic Z^0 boson decay are two isolated high- p_t leptons. In the used datasets, the trigger already preselected events which have high probabilities of at least one central high- p_t lepton. Additionally to this triggered central lepton, a second high- p_t lepton of the same family but opposite charge is required. Electron events where the primary electron is identified as a conversion, where a photon converts into an electron and a positron and muon events containing cosmic rays are removed.

To reconstruct electrons or muons, a track has to be matched to the signals of the calorimeters or muon chambers, respectively. Therefore the efficiency of the lepton reconstruction depends on the tracking efficiency and the reconstruction efficiency of the electromagnetic cluster or muon stubs.

To ensure good quality of the event reconstruction, the difference between the z -vertex of the event and the z_0 of the leptons is required to be small due to ensure they come from the same vertex. All specific cut variables are explained in this section and are listed in table 5.2 for central electrons and in table 5.4 for central muons.

To validate the forward track reconstruction of the *Silicon StandAlone Tracking* and the *Silicon Forward Tracking* the trigger lepton is chosen to be a central lepton which passes all the required cuts. There is no central requirement for the second lepton. If this lepton also is in the central region, the same cuts are applied as for the primary. For leptons detected in the forward region the cuts are defined of the different properties of the plug electromagnetic calorimeter because of the difference compared to the central calorimeter. The coverage of the total muon system is only up to $|\eta| < 1.5$. The muons in the central region, CMUP and CMX are triggered and provide a definite measurement of a muon. The BMU system is mainly used to confirm an isolated track to be a muon and in the far forward region $|\eta| > 1.5$, there is no muon system installed. Therefore the definition of the muon cuts are track based only.

5.1.2 Electron data sample

The trigger path `ELECTRON_CENTRAL_18` preselects central high- p_t electrons. The selection cuts of the three trigger levels are presented below and also the event selection cuts are given. Since two electrons are used the second electron can be also in forward direction. The electrons in forward direction are called *plug electrons* due to the matched cluster of the plug calorimeter. The specific requirements of the electrons are listed in table 5.2 and 5.3.

Central electrons

The used baseline cuts for the *central electrons* are given in table 5.2. The considered variables are :

- E_t : Transverse energy of the calorimeter.
- p_t : Transverse momentum of the associated track.
- E_{had}/E_{em} : Ratio of the hadronic calorimeter energy to the electromagnetic calorimeter energy.
- E/p : Ratio of the electromagnetic calorimeter energy to the momentum of the associated track.
- $|z_0|$: z_0 parameter of the associated track.
- $|\Delta z|$: Distance between z_0 of the associated track and the z position of the primary interaction.
- *Isolation* : is defined as the energy in a cone of the radius $\Delta R = \sqrt{\Delta\eta^2 + \Delta\phi^2} = 0.4$ around the center of the electron cluster divided by its total energy. The cluster energy is corrected by the leakage energy of the calorimeter.
- L_{shr} : The lateral shower profile of the electromagnetic cluster.
- χ_{strip}^2 : Quality of the match of the shower shape for the best matching CES strip cluster with that expected for an electron.
- *# Hits for a good COT segment* : Number of required hits.
- *# Good COT Axial Segments* : Number of COT axial super-layers segments with at least 5 hits for the associated track.
- *# Good COT Stereo Segments* : Number of COT stereo super-layers segments with at least 5 hits for the associated track.

Plug electrons

The used baseline cuts for the *plug electrons* are given in table 5.3. The considered variables are :

- E_t : Transverse energy of the calorimeter

5.1. USED DATA SAMPLES

Central Electron Variable	Cut
E_t	≥ 20.0 GeV
p_t	≥ 10.0 GeV/c
E_{had}/E_{em}	$\leq 0.055 + 0.00045 \cdot E$
E/p ($E_t < 100$ GeV)	$\leq 2.0c$
$ z_0 $	≤ 60.0 cm
$ \Delta z $	≤ 3.0 cm
Isolation	≤ 0.1
L_{shr}	≤ 0.2
χ^2_{strip}	≤ 10.0
# Hits for a good COT segment	≥ 5
# Good COT Axial Segments	≥ 3
# Good COT Stereo Segments	≥ 2

Table 5.2: The baseline cuts for *central electrons*. [57]

- E_{had}/E_{em} : Ratio of the hadronic calorimeter energy to the electromagnetic calorimeter energy.
- *Towers in χ^2 fit* : Number of calorimeter towers used in fit.
- *PEM 3×3 χ^2* : Quality of the match of the energy in a 3×3 cell grid with the expectation for an electron.
- *PES cluster 5×9 ratio* : Ratio of the energy of the five central scintillator bars to the energy of all nine bars of the cluster in the PES. This ratio is defined separately for both dimension variables u,v and both have to fulfilled the cut criterion.
- $\Delta R(PES - PEM)$: Distance $\Delta R = \sqrt{\Delta\eta^2 + \Delta\phi^2}$ in the $\eta\phi$ - plane between the pre-shower cluster and the plug electromagnetic calorimeter cluster.
- $|z_0|$: z_0 parameter of the associated track.
- *Isolation* : is defined as the energy in a cone of the radius $\Delta R = 0.4$ around the center of the electron cluster divided by its total energy. The cluster energy is corrected by the leakage energy of the calorimeter.

Plug Electron Variable	Cut
E_t	≥ 20.0 GeV
E_{had}/E_{em}	≤ 0.05
Towers in χ^2 fit	≥ 1
PEM $3times3$ χ^2	≤ 10.0
PES U cluster $5times9$ ratio	> 0.65
PES V cluster $5times9$ ratio	> 0.65
$\Delta R(PEM - PES)$	≤ 3 cm
Isolation	≤ 0.1
$ z_0 $	≤ 60.0 cm

Table 5.3: The baseline cuts for *plug electrons* [58]

5.1.3 Muon data sample

In the central region there are two different muon systems and therefore each muon sub-detector has its own trigger path. The requirements of both trigger paths, MUON_CMUP18 and MUON_CMX18, are presented below. The events in the used dataset are triggered by a central muon but the study requires two muons and therefore the second muon can also be in forward direction. In this thesis the muons in the range of $|\eta| > 1.0$ are called *forward muons*. The event selection cuts for the central and forward muons are also defined in this section.

Central muons

The used baseline cuts for *central muons* are given in table 5.4. The considered variables are :

- p_t : Transverse momentum of the corresponding track.
- E_{had} : Energy deposition in the hadronic calorimeter.
- E_{em} : Energy deposition in the electromagnetic calorimeter.
- $|z_0|$: z_0 parameter of the associated track.
- $|\Delta x|$: Distance in $r\phi$ between the stub position and the extrapolation of the associated track to the stub.
- $|d_0|$: impact parameter of the associated track with silicon hits.
- *Isolation* : The ratio of the energy within a cone of the radius $\Delta R = 0.4$ of the muon to the transverse momentum of the muon.

5.1. USED DATA SAMPLES

Central Muon Variable	Cut
p_t	$\geq 20.0 \text{ GeV}/c$
E_{had}	$\leq 6 \text{ GeV}$
E_{em}	$\leq 2 \text{ GeV}$
$ z_0 $	$\leq 60.0 \text{ cm}$
$ \Delta x $ in CMU	$\leq 3.0 \text{ cm}$
$ \Delta x $ in CMP	$\leq 5.0 \text{ cm}$
$ \Delta x $ in CMX	$\leq 6.0 \text{ cm}$
$ d_0 $	$\leq 0.02 \text{ cm}$
Isolation	≤ 0.1
# Hits for a good COT segment	≥ 5
# Good COT Axial Segments	≥ 3
# Good COT Stereo Segments	≥ 2

Table 5.4: The baseline cuts for *central muons* [59].

Forward muons

The muons in forward direction are defined by track parameter cuts only and can be confirmed by the BMU muon system in the range $1.0 < |\eta| < 1.5$. Another requirement is that there is almost no energy deposition in the calorimeters along the track, since the muon is a minimal ionizing particle. The muon track has to be isolated and therefore no other tracks are allowed in a cone with $\Delta R = 0.4$ around the muon track. The used baseline cuts for *forward muons* are given in table 5.5.

Forward Muon Variable	Cut
p_t	$\geq 20.0 \text{ GeV}/c$
E_{had}	$\leq 6 \text{ GeV}$
E_{em}	$\leq 2 \text{ GeV}$
$ z_0 $	$\leq 60.0 \text{ cm}$
$ d_0 $	$\leq 0.02 \text{ cm}$
Isolation	≤ 0.1

Table 5.5: The baseline cuts for *forward muons* [59].

5.2 Efficiency of forward tracking

The plug electromagnetic calorimeter allows to determinate the efficiency of the track reconstruction in measured data. A central electron combined together with a plug electron has to be consistent within a mass window of $70 \text{ GeV}/c^2$ to $110 \text{ GeV}/c^2$ of the invariant Z^0 boson mass. A plug electron can be reconstructed without any track of the standard tracking strategies by the so-called *Phoenix* algorithm, a detailed description is given in [60]. The signal events of the leptonic Z^0 boson decay are used to define a denominator of reconstructible tracks. The fraction of events where a forward track matching a plug electromagnetic cluster, if found, is defined as an efficiency of the track reconstruction strategy.

5.2.1 Phoenix Electrons

The Phoenix electrons are reconstructed in the plug electromagnetic calorimeter, using a special strategy. The algorithm uses a standard PEM cluster selected by the cuts defined in table 5.3. In contrast to the PEM electrons no found track has to be matched to this electromagnetic cluster. The track of the Phoenix electron is reconstructed by the algorithm itself. With the position of the PEM cluster in the plug calorimeter and a reconstructed primary vertex, only the curvature of the electron trajectory is not determined. Therefore the Phoenix algorithm uses the transverse energy of the electromagnetic cluster as a quantity of the transverse momentum. The ratio E_t/p_t is equal to one and determines the curvature of the reference track. However both signs are possible due to the reconstruction of an electron or positron. The two helices with opposite sign of the curvature are the reference trajectories of the electron. The *Outside In* strategy of the silicon pattern recognition treats these tracks like COT tracks and executes a hit search along the helices from the outermost layer to the beampipe. For a valid found track at least three axial hits have to be incorporated into the track fit. In order to do this, both tracks are associated to the Phoenix electron and the selection criteria of the best track are the number of found hits and the χ^2/dof of the track. A schematic view of the Phoenix strategy is given in figure 5.1.

5.2.2 Track reconstruction efficiency in di-electron events

To determine the efficiency of track reconstruction in measured data, the event selection of possible Z^0 bosons are used. The tracks of the Phoenix electrons are assumed to be the reference for a reconstructed silicon-only track in measured data. Both tracks are considered matched to each other if the silicon-only track can also be matched to the electromagnetic cluster of the Phoenix electron and if the track parameters are consistent. The efficiency of the tracking

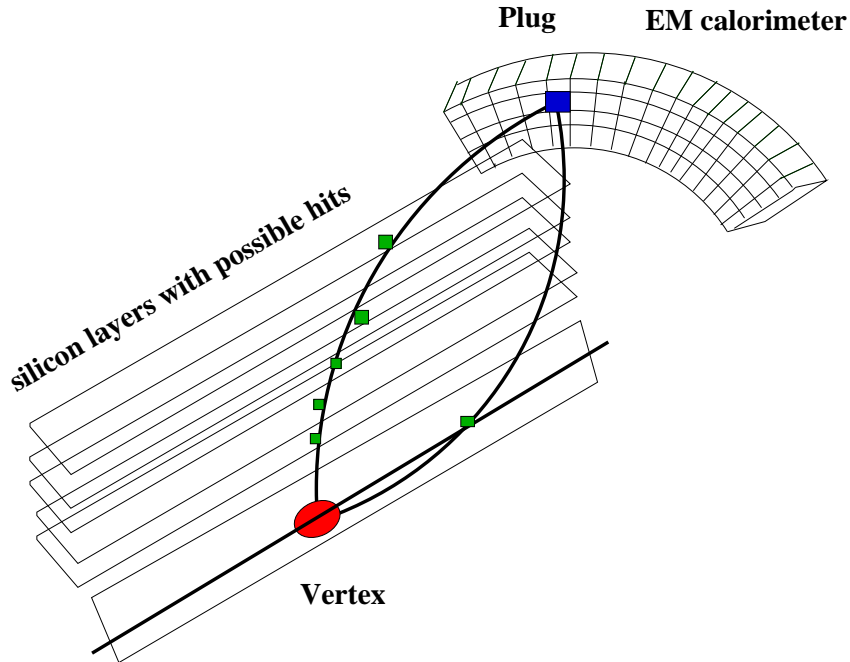


Figure 5.1: Schematic view of the phoenix electron reconstruction. The transverse energy of the plug electromagnetic cluster is used to determine the transverse momentum and the curvature of the electron track. Together with the position of the cluster and the primary vertex a seed helix for an electron and positron can be formed. Along this reference the silicon hits are searched for.

ε_{track} in forward direction can be calculated with the Phoenix electrons as the denominator and a matched silicon-only track as the numerator. The tracking of the Phoenix electrons is independent of the silicon-only tracking strategies and allows to calculate a geometric acceptance α of the silicon detector. The minimum requirements of the FWD tracking strategy are one 3D-Hit and four axial hits in total. The acceptance is defined as the ratio of Phoenix tracks which fulfill these requirements to all Phoenix tracks. The Phoenix algorithm can reconstruct electrons with only three axial hits on a track, due to the additional information of the plug calorimeter. The efficiency of the silicon tracking algorithm $\varepsilon_{algorithm}$ itself has to be corrected for the different requirements with at least four axial hits and one 3D-Hit. Therefore the efficiency is defined as the ratio of the found silicon tracks which can be matched to a PEM cluster, to the Phoenix electrons with a track which fulfill the requirements of the silicon tracking.

$$\begin{aligned}
\varepsilon_{track} &= \frac{\#\text{tracks, which are matched to a phoenix electron}}{\#\text{ all phoenix electrons}} \\
\alpha &= \frac{\#\text{ phoenix tracks (} \geq 1 \text{ 3D-Hit; } \geq 4 \text{ axial hits)}}{\#\text{ all phoenix electrons}} \\
\varepsilon_{algorithm} &= \frac{\#\text{tracks, which are matched to a phoenix electron}}{\#\text{ phoenix tracks (} \geq 1 \text{ 3D-Hit; } \geq 4 \text{ axial hits)}} \\
&= \frac{\varepsilon_{track}}{\alpha}
\end{aligned}$$

In figure 5.2 the acceptance and efficiency is presented as a function of η . The FWD algorithm completes the SiSA strategy. As an example the total efficiency of the silicon-only track reconstruction at $\eta = 2.0$ is almost 50%. The efficiency of the SiSA strategy alone is approximately 25% compared to 10% previously. The additional FWD strategy doubles the efficiency in that η range. The efficiency increase in all η ranges and shows a large improvement of the track reconstruction strategies. The efficiency of the algorithm itself has to be corrected by the acceptance of the silicon detector and results in over 60% at $\eta = 2.0$. The tracking strategies are optimised to provide the best performance in track reconstruction with a reasonable consumption of computing time.

5.3 Reconstruction of leptonic Z^0 boson decays

To select events with a possible Z^0 boson candidate, a central high- p_t lepton is combined with another second high- p_t lepton of opposite charge. The track of the central lepton is always reconstructed by the OI strategy and therefore these tracks provide no additional information of the forward-tracking performance. The track of the second lepton is used to study the track reconstruction in forward direction.

To demonstrate the contribution of the different tracking strategies, the distribution of the reconstructed di-lepton mass is shown for each tracking strategy separately. In this chapter the tracks of the IO strategy are also considered as silicon tracks due to the required reconstructed silicon track as a seed for the IO strategy. Without silicon-only tracking, which provides the seed tracks for the IO strategy, these tracks can not be found and therefore any contribution of the IO tracks to the event reconstruction can be seen as an achievement of the silicon-only tracking.

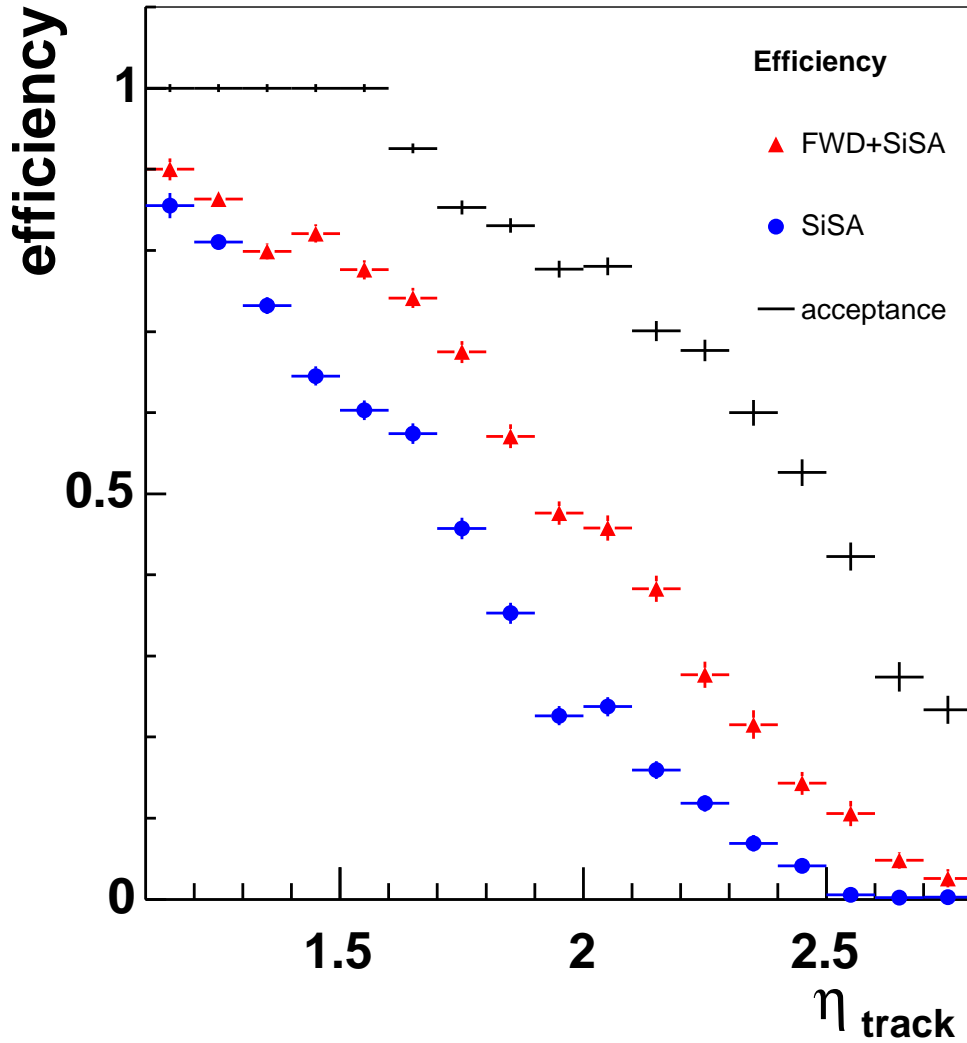


Figure 5.2: The efficiencies of the track reconstruction in forward direction depend on η . The efficiency of the SiSA strategy is improved and the combination of both strategies, SiSA and FWD results in an efficiency over 50% in the range $\eta < 2.0$. The tracking strategies require more reconstructed hits than the Phoenix strategy. Therefore the efficiency of the algorithm itself has to be corrected by the geometric acceptance of the silicon detector which is also presented in this plots. The ratio of the calculated efficiency to the detector acceptance is the efficiency of the algorithm itself.

5.3.1 Z^0 boson decay into electrons

In the efficiency study the di-electron channel was chosen to determine the efficiency of the silicon forward tracking using the Phoenix algorithm on observed data which can only reconstruct electrons. For the Z^0 boson decay into two electrons the usage of the Phoenix electrons would provide a higher efficiency compared to the plug electrons. Nevertheless the plug electrons can also be used for the reconstruction of the di-electron mass.

To validate the silicon forward tracking the Z^0 mass is reconstructed from a central electron and a second central electron or plug electron. The invariant mass of the two electrons is calculated from the calorimeter energy measurements and therefore the width of the mass peak depends on the calorimeter resolution. For particles with the required energy, the resolution of the calorimeter is better than the p_t -resolution of the track, e.g. a particle with an energy of 40 GeV:

$$\begin{aligned} \text{calorimeter: } \quad \sigma_E/E \ (E = 40 \text{ GeV}) &\approx 0.16/\sqrt{(E/[\text{GeV}])} = 2.53\% \\ \text{silicon track: } \quad \sigma_{p_t}/p_t \ (p_t = 40 \text{ GeV}/c) &\approx 0.005 \cdot (p_t/[\text{GeV}/c]) = 20.0\% \end{aligned}$$

In figure 5.3 the invariant mass of the two electrons $m_{e^+e^-}$ is presented for each track strategy separately and in figure 5.4 all distributions of the di-electron mass are stacked together, forming a clear Z^0 boson mass peak. The silicon tracking provides a gain in the number of reconstructed Z^0 bosons by around 40% compared to the central region only. The mean of a fitted Gaussian distribution is $\mu = (90.76 \pm 3.10) \text{ GeV}/c^2$ and is consistent with the world average of $m_Z = 91.19 \text{ GeV}/c^2$ [1].

The peak in the mass distribution is slightly asymmetric due to the bremsstrahlung of the electrons. The electrons interact with the material of the detector and lose energy. The energy loss can be seen by an asymmetric peak in the di-electron mass which is shifted slightly to lower masses. In figure 5.5 the η distribution of the second electron is shown. The electrons in the range $|\eta| < 1.0$ are matched to an OI track. In the region $|\eta| < 2.5$ the track which is matched to the electron, is reconstructed by the silicon-only strategies. The inefficiency at $\eta = 1$ is due to a gap in the electromagnetic calorimeter between the central part and the plug calorimeter.

5.3. RECONSTRUCTION OF LEPTONIC Z^0 BOSON DECAYS

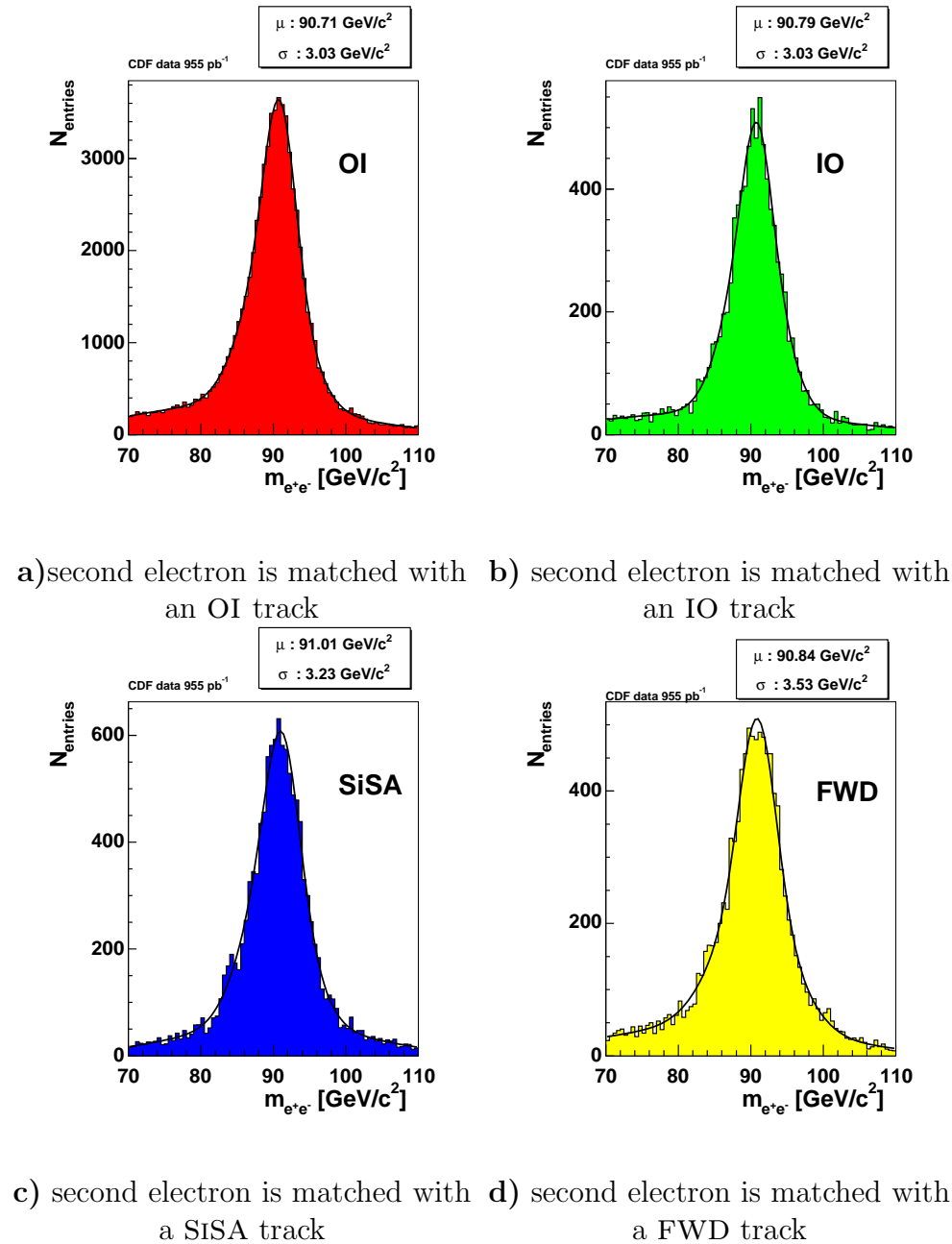


Figure 5.3: The plots show the invariant mass distribution of di-electron events. The first electron is a tight central electron and is combined to any other second electron which is selected by the cuts. The distribution of the reconstructed di-electron mass is shown for each tracking strategy separately. The resolution of the di-electron mass is dominated by the resolution of the calorimeter and therefore the mass distribution peaks with similar resolution for all different track types. The distributions are fitted using the sum of three Gaussians to account for the slightly asymmetric shape of the peak and long tails. The mean μ and σ of the Gaussian which represents the peak are displayed in each plot.

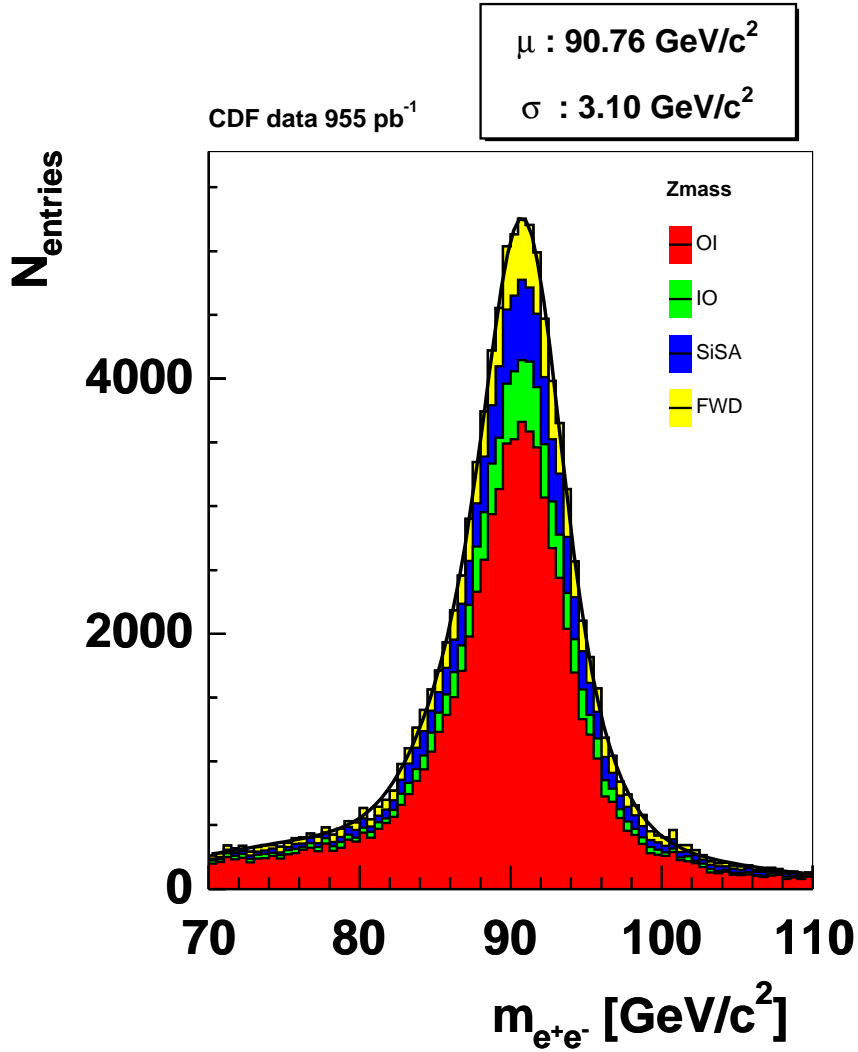


Figure 5.4: The mass distribution of two electrons shows a clear peak at the mass of the Z^0 boson. The fitted Gaussian has the mean at $(90.76 \pm 3.10) \text{ GeV}/c^2$. The silicon tracks increase the number of reconstructed Z^0 bosons by $\approx 40\%$ compared to the OI tracks. The distributions are fitted with a the sum of three Gaussians to account for the slightly asymmetric shape of the peak and the long tails. The mean and sigma of the Gaussian which represent the peak are displayed in the plot.

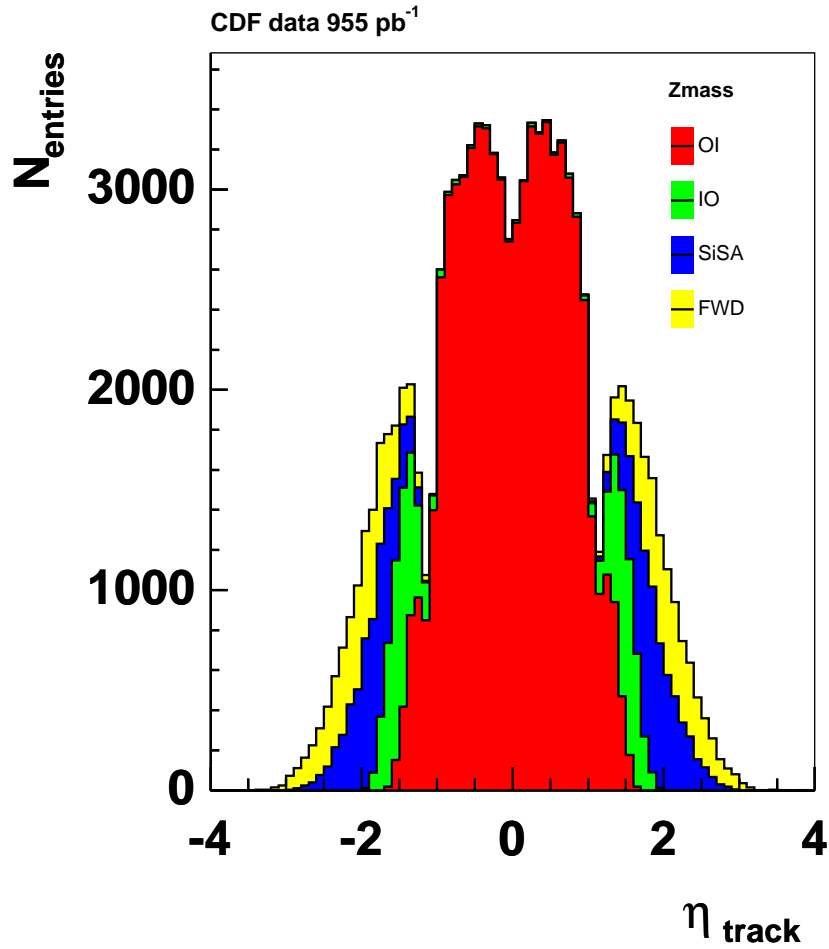


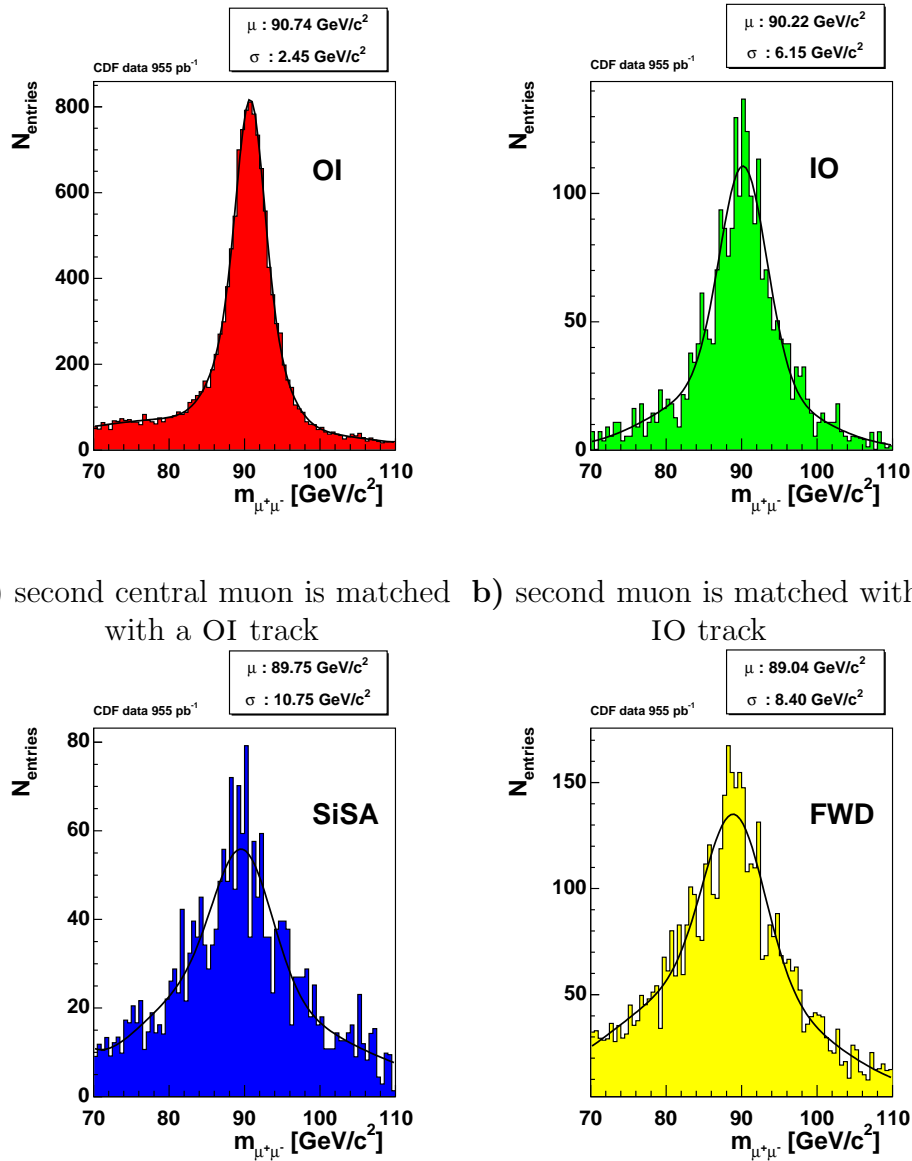
Figure 5.5: The η distribution of the track of the second electron shows the silicon tracks in forward direction. The central electrons are matched with tracks of the OI strategy. The inefficiency at $|\eta|=1$ is due to the gap between the central and the plug electromagnetic calorimeter. At $|\eta|=0$ the central electromagnetic calorimeter has some readout electronic devices, which also causes an inefficiency.

5.3.2 Z^0 boson decay into muons

The reconstruction of the di-muon mass is similar to the di-electron mass reconstruction. A central high- p_t muon is combined with a second muon of opposite charge. The second muon can be a central muon or a forward muon which is an isolated track which deposits almost no calorimeter energy. The invariant mass of the di-muon is calculated by the momentum of the central muon and the forward track. The resolution of the di-muon mass depends on the track resolution and therefore the OI tracks of the central muons profit from the good p_t resolution of the drift chamber. The resolution of the silicon tracks is worse due to the shorter length of the track and due to the smaller number of hits. The resolution of the tracks depends on the momentum of the tracks and varies strongly. The distribution of the reconstructed di-lepton mass is shown for each tracking strategy separately, see figure 5.6. In figure 5.7 these distributions are stacked and form a clear mass peak at the expected mass of the Z^0 boson. A fitted Gaussian has the mean value of $\mu = (90.53 \pm 2.74) \text{ GeV}/c^2$ and is consistent with the world average of the Z^0 boson mass of $m_Z = 91.19 \text{ GeV}/c^2$ [1]. The silicon tracking increases the number of reconstructed Z^0 bosons by $\approx 38\%$ compared to the OI tracks. For the reconstruction of muons in forward direction, the silicon tracking is the only possible algorithm to find the tracks of the particle. With the tracks of the SiSA and the FWD tracking strategy, the η range of the di-muon reconstruction can be increased from the central region $|\eta| < 1.0$ up to the forward region $|\eta| < 2.5$ which is shown in figure 5.8. The η distribution of the second muon in the di-muon reconstruction reflects the muon chambers of the detector. The central range $|\eta| < 0.6$ has the highest efficiency of muon reconstruction due to the two muon detectors CMP and CMU. The OI tracks in the range $0.6 < |\eta| < 1.0$ are matched to measurements in the CMX.

Isolated tracks in forward direction which pass no muon system are called *stubless muons* if the tracks pass the muon selection cuts. The fake rate of the stubless muons is higher due to the missing confirmation of a muon system. However the di-muon mass of the selected muon tracks peaks at the mass of the Z^0 boson. The width of the mass peak of the stubless muons is much broader than for the OI tracks due to the worse momentum resolution of the SiSA and FWD tracks.

$$\begin{aligned}
 \text{OI} & : \sigma_{p_t}/p_t^2 \approx 0.15 \% (\text{GeV}/c)^{-1} \\
 \text{SiSA} & : \sigma_{p_t}/p_t^2 \approx 0.4 \% (\text{GeV}/c)^{-1} \\
 \text{FWD} & : \sigma_{p_t}/p_t^2 \approx 0.5 \% (\text{GeV}/c)^{-1}
 \end{aligned}$$



a) second central muon is matched with a OI track b) second muon is matched with a IO track

c) second muon is matched with a SiSA track d) second muon is matched with a FWD track

Figure 5.6: The plots show the mass distribution of di-muon events. The first muon is a tight central muon and is combined to any other second muon passing the cuts. The distribution of the reconstructed di-muon mass is shown for each tracking strategy separately. The resolution of the di-muon mass is dominated by the resolution of the track momentum which also depends on the momentum. To compensate the effect of the different momentum resolutions for all tracks the distributions are fitted with two Gaussians. The mean and sigma of the Gaussian which represent the narrow peak are displayed in each plot.

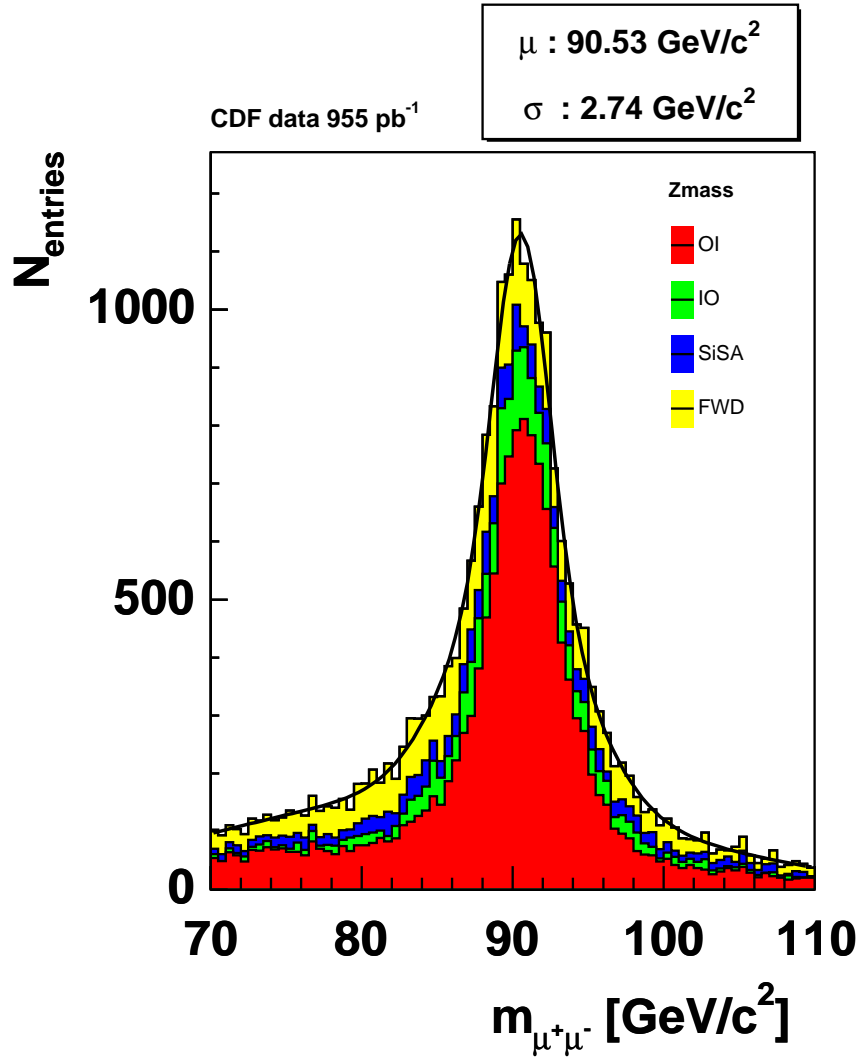


Figure 5.7: The mass distribution of two muons shows a clear peak at the mass of the Z^0 boson. The fitted Gaussian has the mean at $90.53 \text{ GeV}/c^2 \pm 2.74 \text{ GeV}/c^2$. The number of reconstructed di-muon events increases by $\approx 38\%$, using the silicon tracks in addition to the OI tracks. To compensate the effect of the different momentum resolutions of the tracks the distributions are fitted with a sum of two Gaussians.

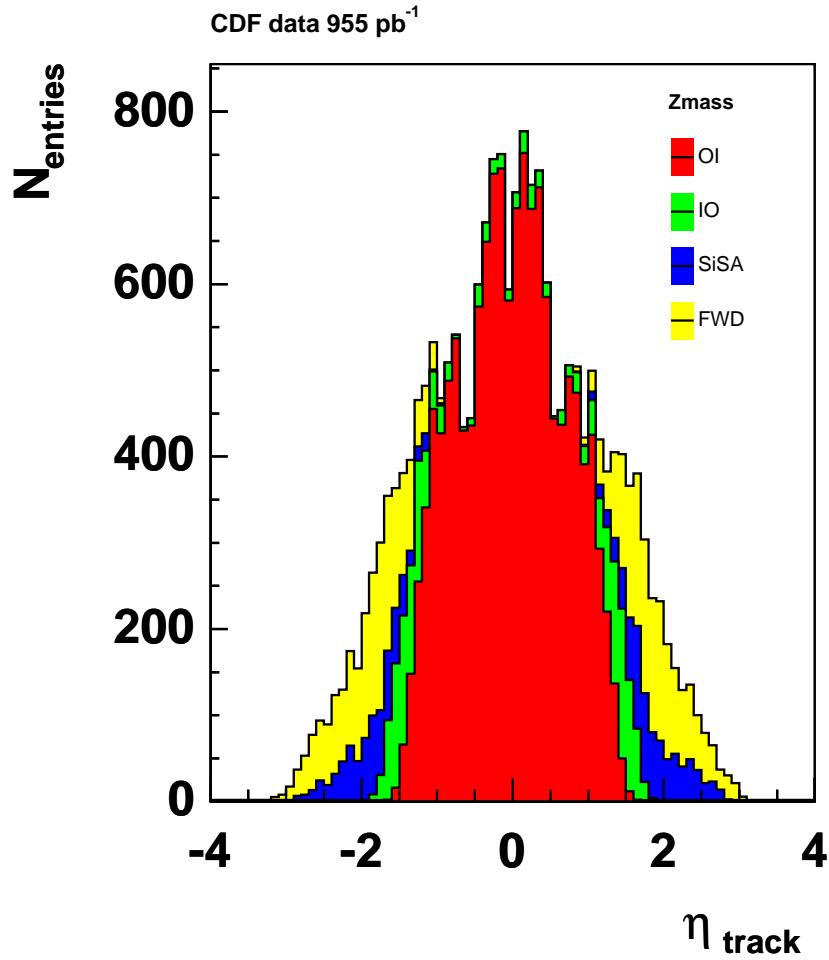


Figure 5.8: The η distribution of the second muon shows the silicon tracks in forward direction. The central range $|\eta| < 0.6$ has the highest efficiency of muon reconstruction due to the two muon detectors CMP and CMU. The OI tracks at $|\eta| \approx 1.0$ are matched to the measurements in the CMX. The muons of the silicon track strategies are isolated tracks which can be confirmed by the BMU muon system in the range $1.0 < |\eta| < 1.5$.

5.4 Summary

In the example of the leptonic Z^0 boson decay, approximately 40% of the reconstructed di-lepton events are matched with a silicon only track. With the SiSA and the FWD tracks, the η range of reconstructible particles is extended from the central region of the OI tracks $|\eta| < 1.0$ up to $|\eta| < 2.5$. The FWD strategy completes the SiSA strategy and improves the silicon track reconstruction in forward direction. At $\eta = 2.0$ a track reconstruction efficiency of 25% of the SiSA strategy can be achieved. The combination of both algorithms results in a total efficiency of 50% at $\eta = 2.0$.

fit results [GeV/ c^2]		OI	IO	SiSA	FWD	total
di-electron	mean (μ)	90.71	90.79	91.01	90.84	90.76
	sigma (σ)	3.03	3.03	3.23	3.53	3.10
di-muon	mean (μ)	90.74	90.22	89.75	89.04	90.53
	sigma (σ)	2.45	6.15	10.75	8.40	2.74

Table 5.6: Fit results of the di-lepton mass. Two Gaussians were chosen to describe the asymmetry of the di-electron mass due to the radiation of photons and the momentum dependence of the track resolution in the di-muon mass. The table shows the results of the fit parameters of the Gaussian representing the narrow signal peak.

Chapter 6

Conclusion

In this thesis I studied and developed tracking algorithms at the Collider Detector at Fermilab, CDF. As a first part I have improved the quality of the reconstructed hits on which the tracking algorithms are based. As second part the existing track reconstruction strategies are improved and a new tracking strategy is introduced in order to extend the acceptance for track-based analyses. The range in η where tracks can be reconstructed is increased by the new tracking algorithm.

The measurements of the silicon detector vary in their quality. By imposing requirements on the characteristics of signals which stem from fluctuations or miscalibrations of the detector, fake hits can be removed and a higher purity of selected hits can be achieved. The quality and timing performance of the track reconstruction benefits from an improved hit set which contains less fake hits. In some cases up to 93.5% of the fake hits can be removed.

The new silicon tracking algorithm completes the track reconstruction strategy of the central detector region which works well. Due to the requirement to find hits in the central drift chamber, the *Outside In* strategy is limited to the detector region up to $|\eta| < 1.0$. The existing *Silicon StandAlone* strategy is modified and improved to allow track reconstruction with an efficiency of 25% at $|\eta| = 2.0$, compared to the 10% efficiency of the previous version. To compensate for the geometrical acceptance of the working silicon detector an additional tracking strategy is implemented, the so-called *Silicon Forward* strategy. The new algorithm requires less reconstructed hits for a track in the silicon detector. This additional strategy improves the track reconstruction efficiency in forward direction. The combination of both new tracking strategies increases the track reconstruction efficiency by a factor of five, from 10% to 50% at $|\eta| = 2.0$.

I have studied the performance of both new silicon tracking strategies using data taken by the CDF II experiment from February 2002 until February 2006.

The total integrated luminosity of the data sets used is 955 pb^{-1} . To validate the track reconstruction, the Z^0 boson decay channel into e^+e^- and $\mu^+\mu^-$ was chosen. The signature of this decay are two high- p_t electrons or muons of opposite charge. A central high- p_t electron or muon is used to trigger such an event and the second lepton is used to study the tracking performance, especially in forward direction. The distributions of the reconstructed di-electron and di-muon mass show a clear peak at the expected Z^0 boson mass of $91.19 \text{ GeV}/c^2$. The forward leptons which are reconstructed by the new forward algorithms increase the number of reconstructed Z^0 bosons by $\approx 40\%$ compared to the tracks of the central region which are reconstructed by the Outside In strategy.

The resolution of the reconstructed Z^0 boson mass in the electron decay channel is dominated by the resolution of the energy measurement of the electromagnetic calorimeter and therefore is similar for tracks of all strategies.

In the muon decay channel the resolution of the reconstructed mass is dominated by the momentum resolution of the muon tracks. The central Outside In tracks have a p_t resolution of $\sigma_{p_t}/p_t^2 \approx 0.15 \text{ \% (GeV}/c)^{-1}$ compared to the tracks of the Silicon StandAlone strategy with $\sigma_{p_t}/p_t^2 \approx 0.4 \text{ \% (GeV}/c)^{-1}$ and the Silicon Forward strategy with $\sigma_{p_t}/p_t^2 \approx 0.5 \text{ \% (GeV}/c)^{-1}$. Therefore the width of the peak of the di-muon mass distribution is broader for events with a reconstructed forward muon from the Silicon StandAlone and Silicon Forward tracking strategies.

Both new silicon track reconstruction strategies are implemented in the offline software framework of CDF II and are part of the next official raw data reconstruction process. The increase of the η range of the track reconstruction opens a new field of track-based physics analyses in forward region. The decay products of numerous interesting physics events are boosted into forward direction. In future all statistically limited track-based analyses will benefit from the higher number of reconstructed events due to the new forward tracks.

Appendix A

Silicon hits

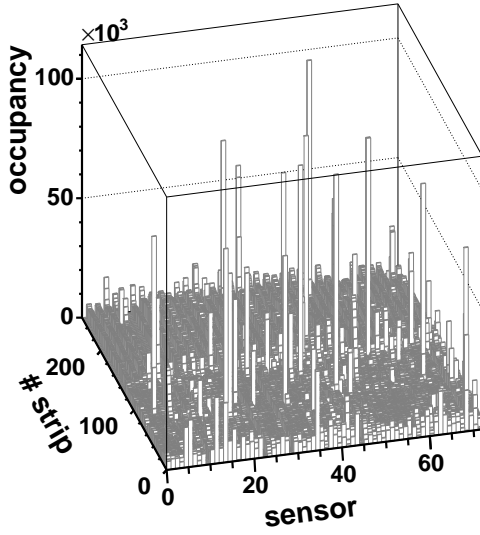
A.1 Studies of silicon hits and strips

In section 3.4.2 a study of the hit quality is presented utilizing the distribution of the strip occupancy. All strips of reconstructed hits are studied for each halfadder side. All the 1384 halfadder sides can not be presented in this thesis. To give an overview the distributions of all sensors of one layer are shown in a single plot. The strip axis is directly the strip number and the sensor axis is a combination of the wedge number and the bulkhead number of one layer side:

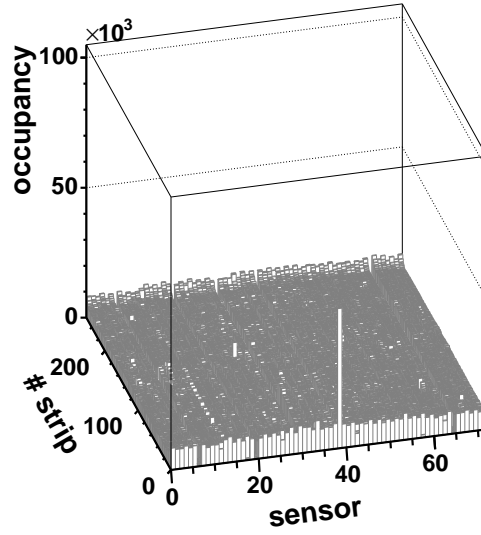
$$\text{no. of sensor} = \text{no. of wedge} + \text{no. of bulkhead} \cdot \text{total wedge number}$$

The occupancy plots A.1-A.4 give an overview of the hot and noisy strips in the several layers. Very hot strips with an over 100 times higher efficiency than the average can be seen in all layers. To identify these strips and remove them from the hit set will provide a much better hit quality to the track reconstruction strategies.

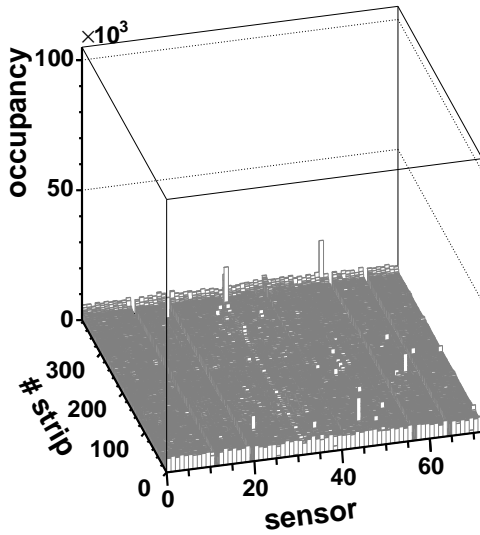
layer 0 side p



layer 1 side p



layer 2 side p



layer 3 side p

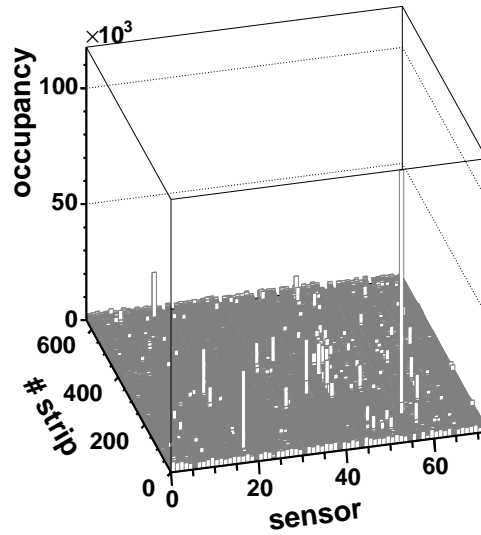
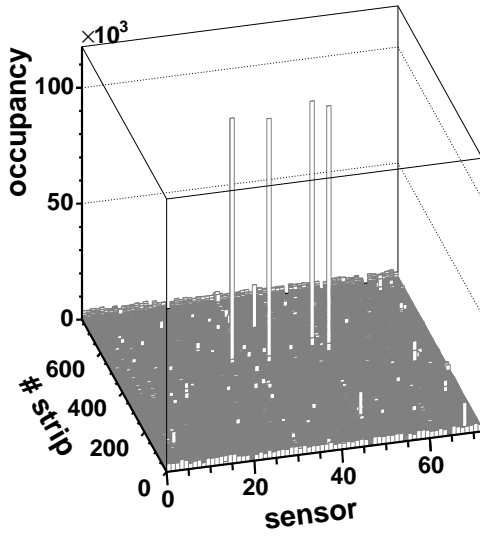
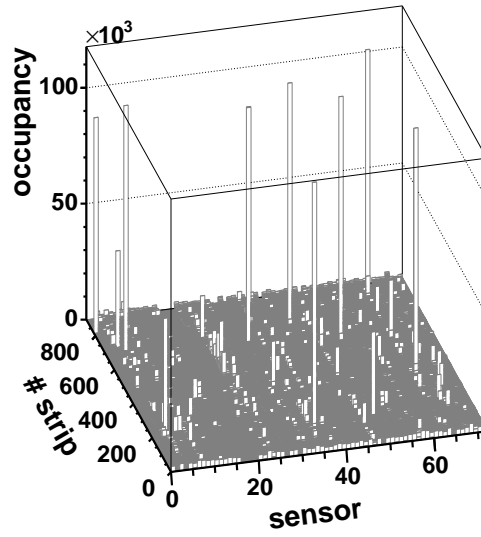


Figure A.1: The occupancy of all sensors on the p-side of LAYER 0 - LAYER 3 are shown.

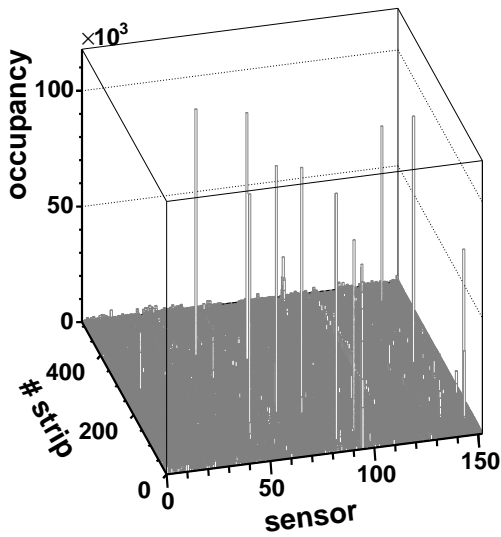
layer 4 side p



layer 5 side p



layer 6 side p



layer 7 side p

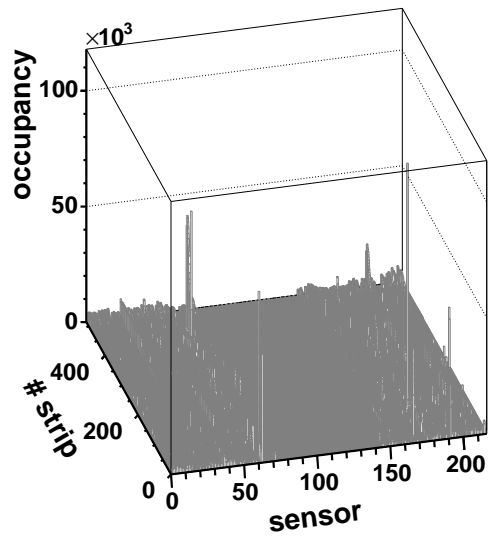
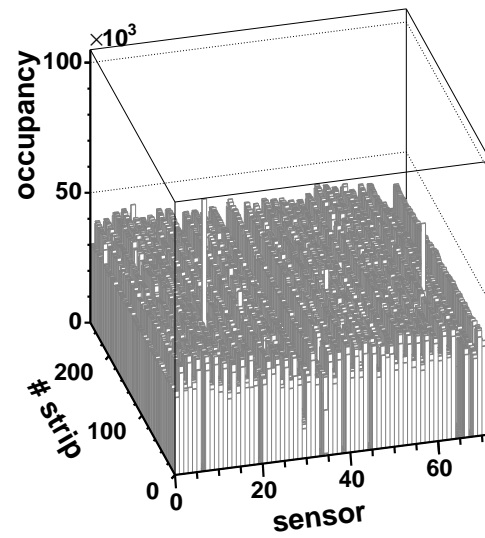
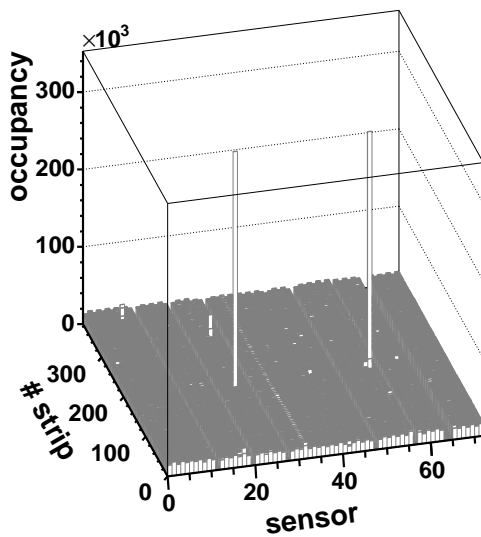


Figure A.2: The occupancy of all sensors on the p side of LAYER 4 - LAYER 7 are shown.

layer 1 side n



layer 2 side n



layer 3 side n

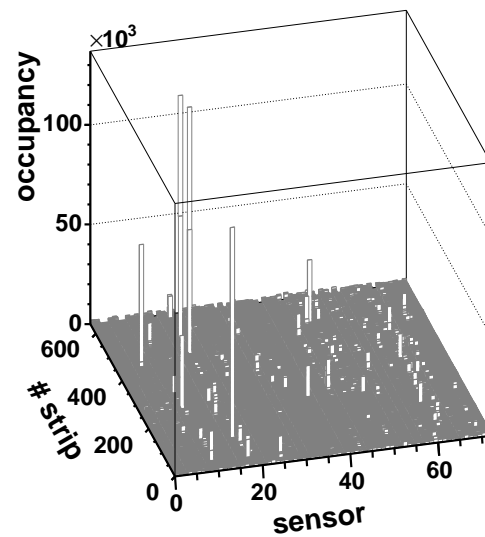
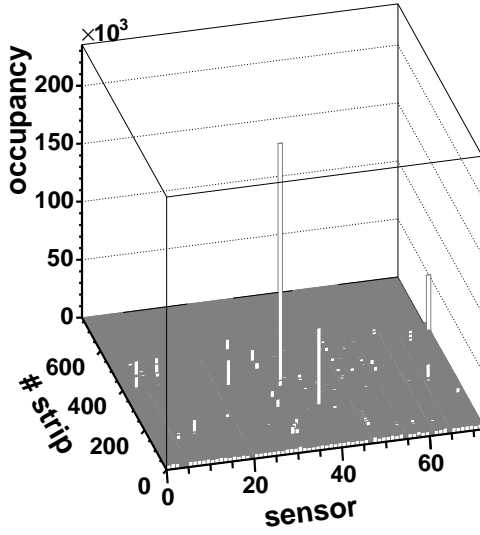
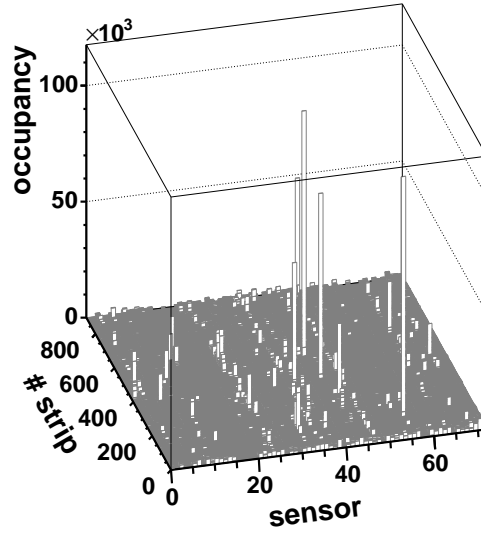


Figure A.3: The occupancy of all sensors on the n side of LAYER 0 - LAYER 3 are shown.

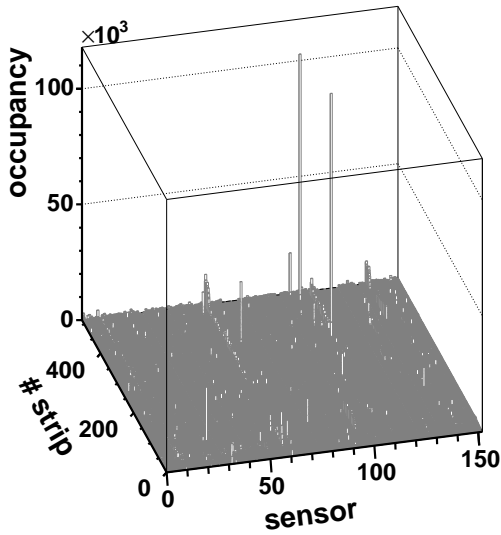
layer 4 side n



layer 5 side n



layer 6 side n



layer 7 side n

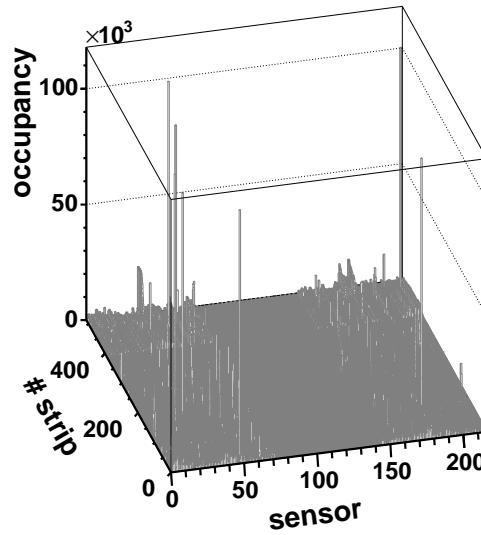


Figure A.4: The occupancy of all sensors on the n side of LAYER 4 - LAYER 7 are shown.

A.2 Map of working halfadders

Some halfadders and chips are not working anymore. A visualization of the occupancy of the ϕ -sides are shown in figures A.5, A.7 and the occupancy of the z - and *stereo*-sides are shown in figure A.6, A.8. The silicon-only track reconstruction strategies SiSA and FWD require 3D-Hits. A 3D-Hit is reconstructed of a measurement on the ϕ and on the stereo side of the SAS layers. Therefore both sides have to be working and the resulting combinations are shown in figure 3.25.

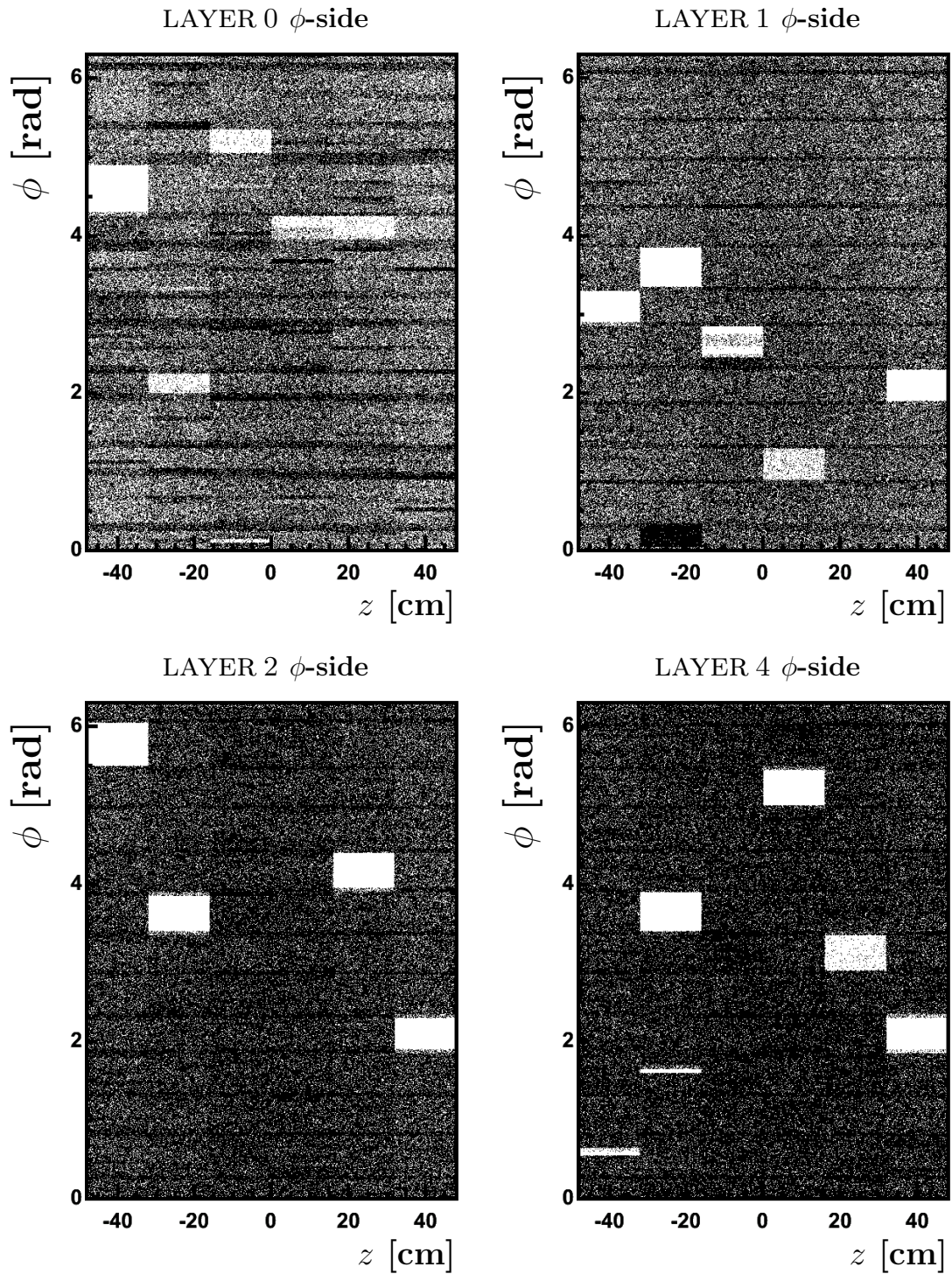


Figure A.5: Map of working ϕ sides in Z90 layers

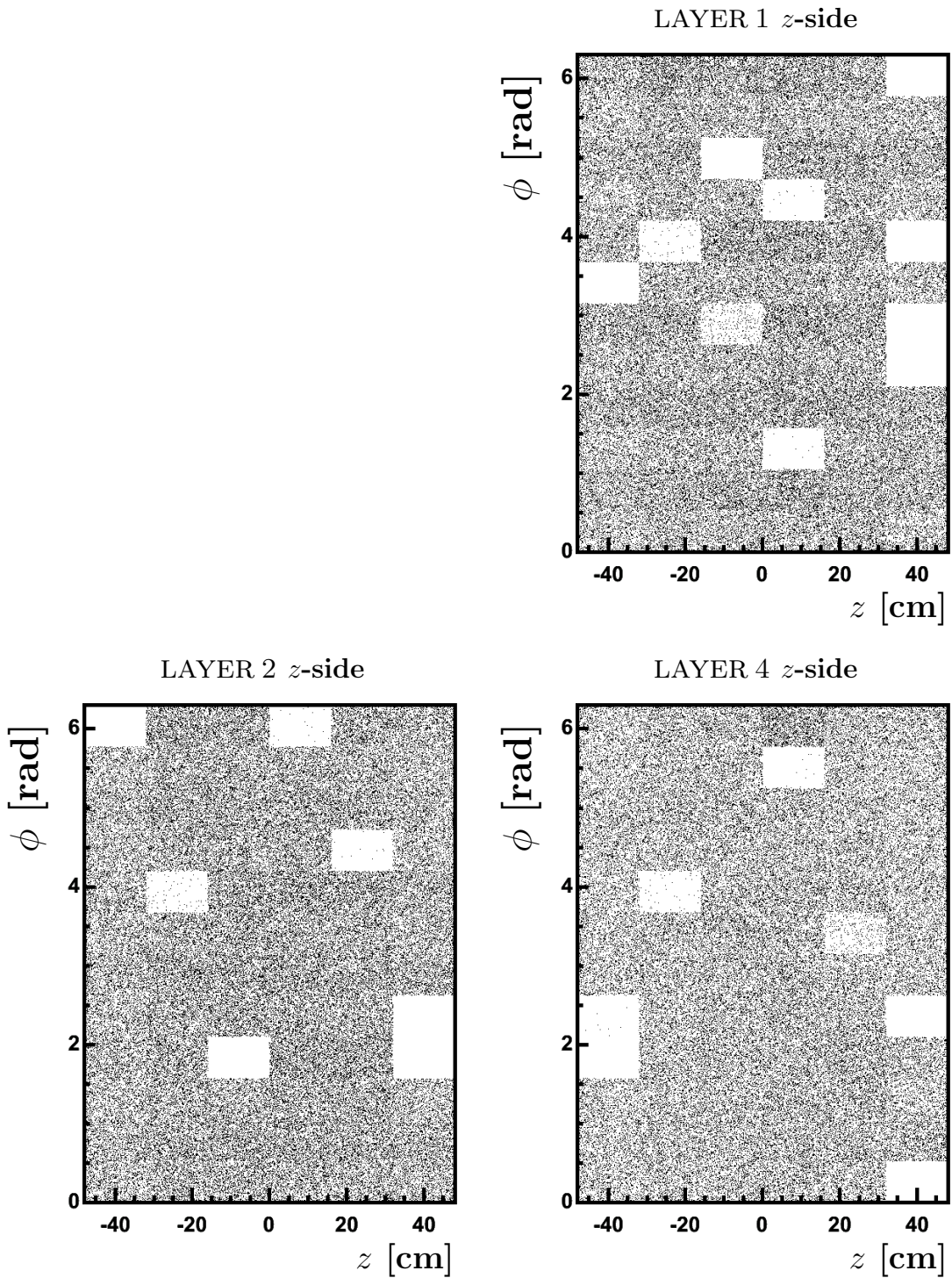


Figure A.6: Map of working z sides in Z90 layers

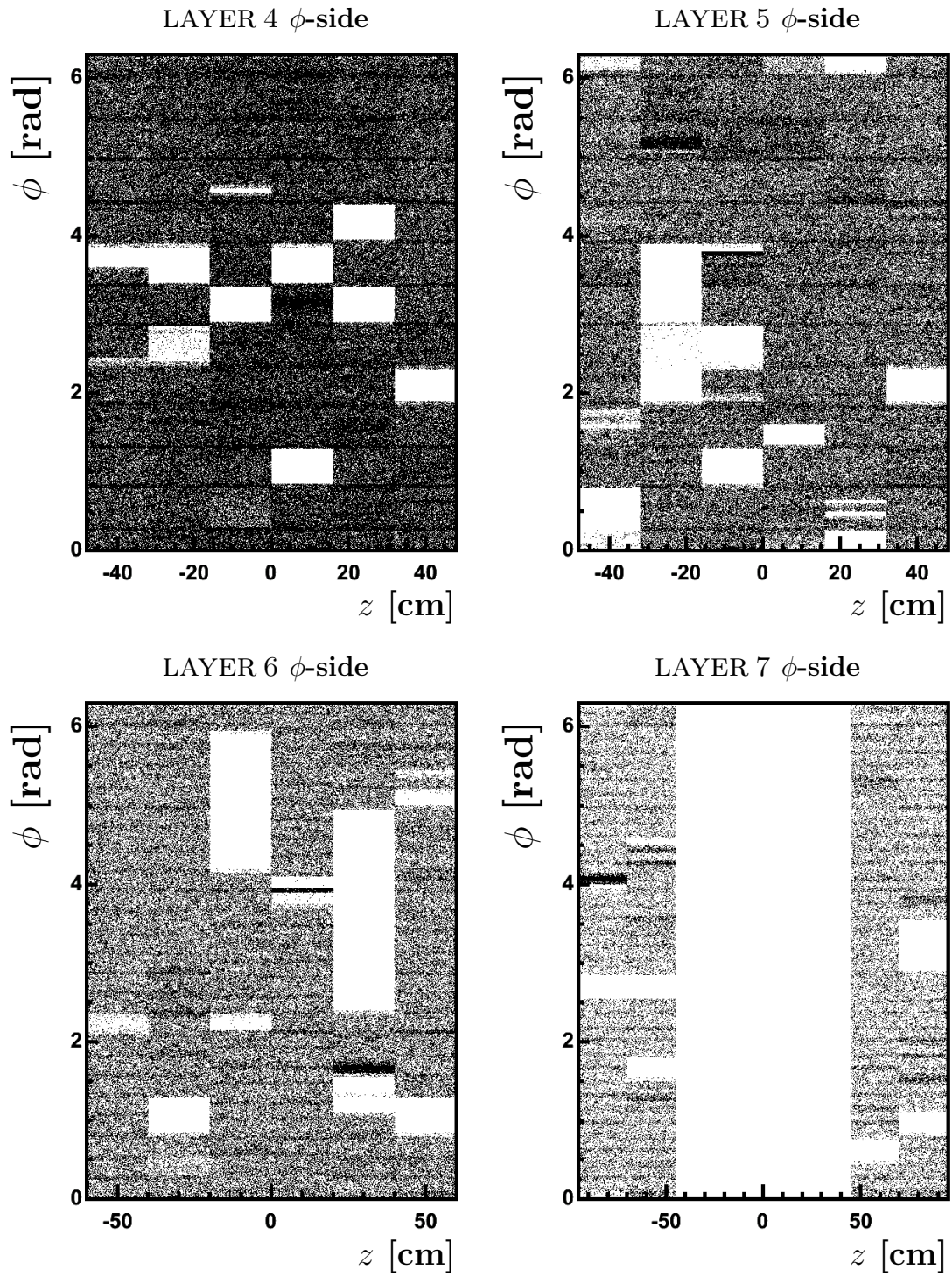


Figure A.7: Map of working ϕ sides in SAS layers

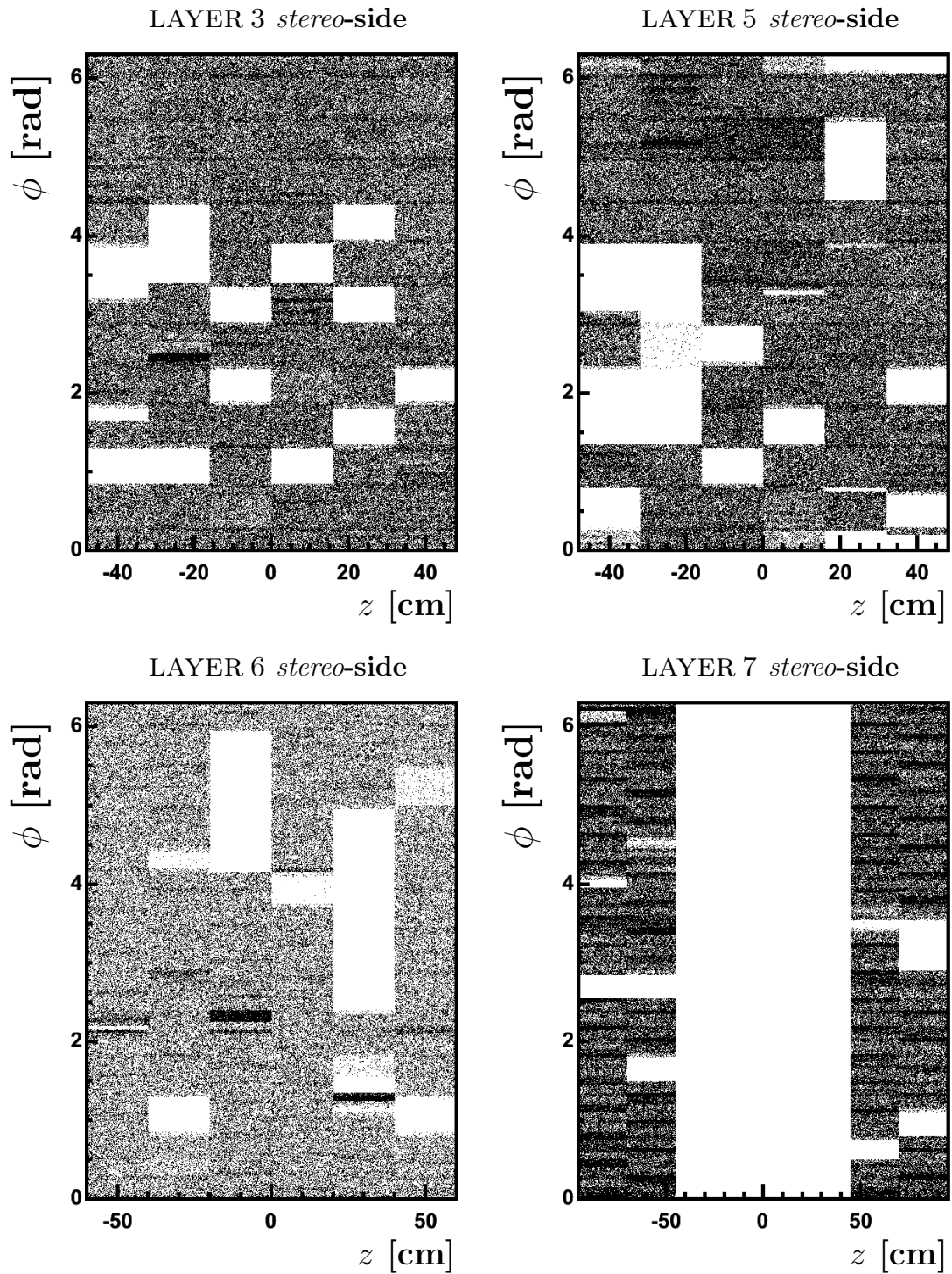


Figure A.8: Map of working stereo sides in SAS layers

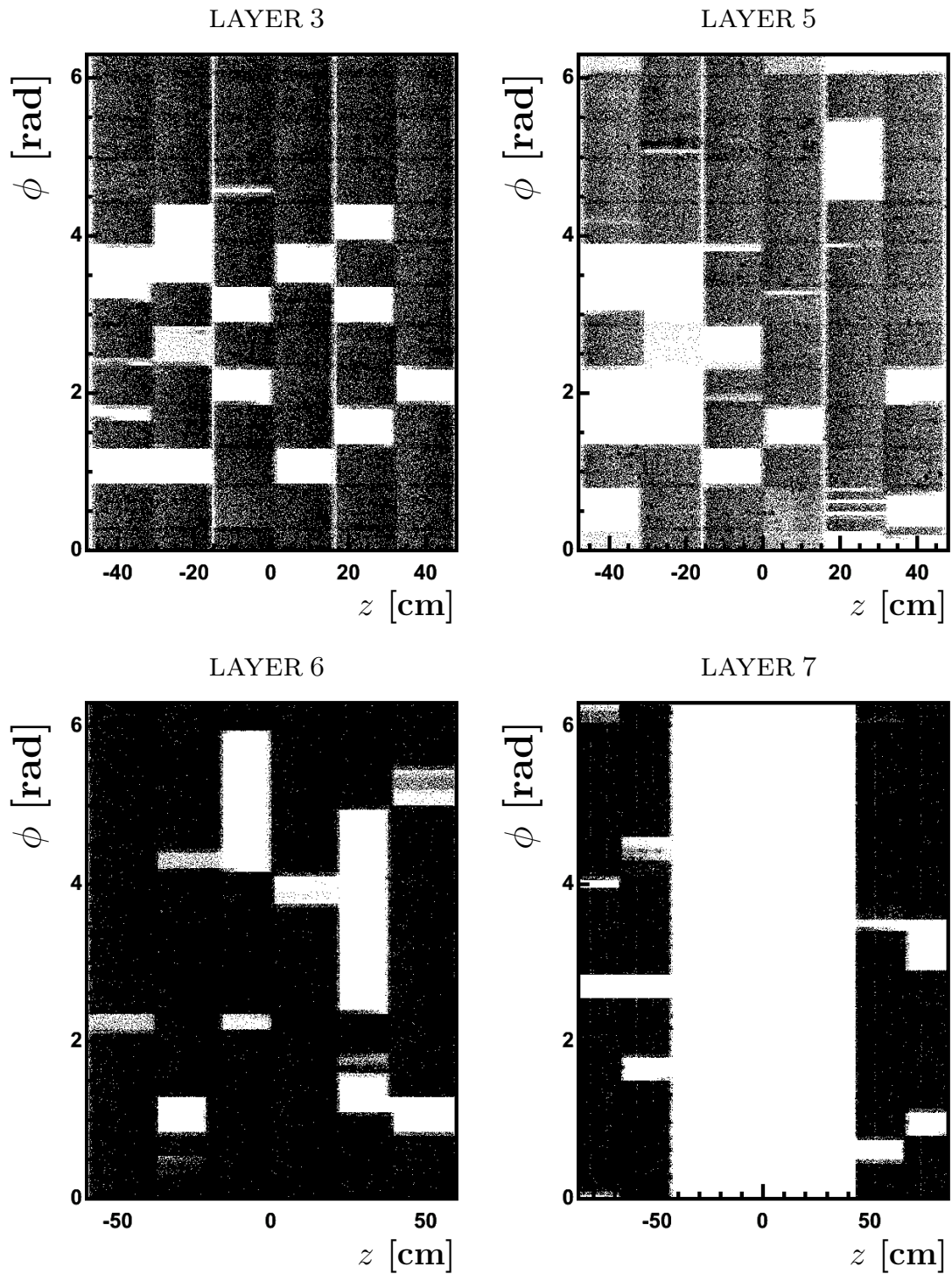


Figure A.9: Map of working 3D sensors in SAS layers

Appendix B

Fit layers

canonical layer	sub-layer	geometric layer	type	number	material
		Beam-Pipe	Extra	0	passive
			dE/dx-Material	1	passive
LAYER 0	inner	L00	Phi	2	active
			Material	3	passive
		L00Sup	Material	4	passive
		L00Sup	Material	5	passive
	outer	L00	Phi	6	active
			Material	7	passive
LAYER 1	inner	Z90	Z90	8	active
			Phi	9	active
			Material	10	passive
		Hybrid	Material	11	passive
	outer	Z90	Z90	12	active
			Phi	13	active
			Material	14	passive
Hybrid			Material	15	passive

canonical layer	sub-layer	geometric layer	type	number	material
LAYER 2	inner	Z90	Z90	16	active
			Phi	17	active
			Material	18	passive
		Hybrid	Material	19	passive
	outer	Z90	Z90	20	active
			Phi	21	active
			Material	22	passive
		Hybrid	Material	23	passive
LAYER 3	inner	SAS	SAS	24	active
			Material	25	passive
		Hybrid	Material	26	passive
	outer	SAS	SAS	27	active
			Material	28	passive
		Hybrid	Material	29	passive
	Hybrid	Material	30	passive	
LAYER 4	inner	Z90	Z90	31	active
			Phi	32	active
			Material	33	passive
		Hybrid	Material	34	passive
	outer	Z90	Z90	35	active
			Phi	36	active
Material			37	passive	
	Hybrid	Material	38	passive	
LAYER 5	inner	SAS	SAS	39	active
			Material	40	passive
		Hybrid	Material	41	passive
	outer	SAS	SAS	42	active
			Material	43	passive
	Hybrid	Material	44	passive	
		PortCard	dE/dx-Material	45	passive
		PortCard	dE/dx-Material	46	passive
		PortCard	dE/dx-Material	47	passive

canonical layer	sub-layer	geometric layer	type	number	material
LAYER 6		Hybrid	Material	48	passive
	inner	SAS	SAS	49	active
			Material	50	passive
		IslLedge	Material	51	passive
		Hybrid	Material	52	passive
	outer	SAS	SAS	53	active
			Material	54	passive
		IslLedge	Material	55	passive
		Hybrid	Material	56	passive
	central inner	SAS	SAS	57	active
			Material	58	passive
		IslLedge	Material	59	passive
		Hybrid	Material	60	passive
central outer	SAS	SAS	61	active	
		Material	62	passive	
	IslLedge	Material	63	passive	
LAYER 7		Hybrid	Material	64	passive
	inner	SAS	SAS	65	active
			Material	66	passive
		IslLedge	Material	67	passive
		Hybrid	Material	68	passive
	outer	SAS	SAS	69	active
Material			70	passive	
	IslLedge	Material	71	passive	
		InnerCan-PhysVol	Material	72	passive
			COT	73	passive

Table B.1: Table of all fit layers with the corresponding layers and sublayers.

Appendix C

SiPatternRecModule tcl-switches

The track reconstruction strategies can be controlled and tuned by so-called tcl-switches. All the switches concerning the silicon tracking strategies of the TrackingKal package are presented with their default values. The switches are sorted by their different tasks.

tcl-switches of the strategies

Turn the corresponding silicon track reconstruction on or off.

PerformOutsideInTracking	set	true
PerformOIZTracking	set	true
PerformKalOISvxStandaloneTracking	set	true
KalStandaloneOff	set	false
PerformKalSvxStandaloneTracking	set	false
PerformKalForwardTracking	set	false
PerformPerfectSiTracking	set	false

general tcl-switches for all strategies

The general properties of the strategies are set up by the following switches.

```

SVXBeamOff          set  false
UpdateSVXBeamEvent  set  true
BeamX0               set  -0.16695
BeamY0               set  0.43157
PassAllCandidates    set  false
minADCHitCharge     set  20
zigzagbonding        set  true
method               set  GLOBAL
ZVerDescrip          set  ZVertexColl
inputTracks          set  COTGlobalTrackin
inputHitSet          set  GlobalSIHitSet
outputTracks         set  GlobalSITracking
UseSiliMapInKal     set  false
KalCOTErrorScale    set  2.25

```

tcl-switches of the OutsideInTracker

The tuning switches of the Outside In strategy are presented below.

```

KALOIonUnusedCOTTracksOnly  set  true
KalOI3LoopDebugLevel        set  0
KalOI3LoopMinPhiHits        set  3
KalOI3LoopPhiminRoad        set  0.0
KalOI3LoopChi2Cut1          set  40.0
KalOI3LoopChi2Cut2          set  30.0
KalOI3LoopChi2Cut3          set  20.0
KalOI3LoopChi2Cut4          set  10.0
KalOI3LoopChi2Cutz          set  40.0
KalOI3LoopCleanUpPhi        set  true
KalOI3LoopCleanUpZ          set  true
KalOI3LoopPhiSigmaRoad1     set  8.0
KalOI3LoopPhiSigmaRoad2     set  6.0
KalOI3LoopPhiSigmaRoad3     set  3.0
KalOI3LoopZSigmaRoad        set  4.0
KalOI3LoopSASSigmaRoad      set  4.0

```

tcl-switches of the SiliconStandaloneTracker

The tuning switches of the Silicon StandAlone strategy are presented below.

KalSVXDebugLevel	set	0
UseZ90InKalSiSA	set	true
UseStereoInKal	set	true
UseAllHitsInKalStandalone	set	false
MinimumSVXPt	set	0.2
KalSVXMinPhiHits	set	4
KalSVXMaxChi2pdof	set	20.0
KalSVXPhiWindow	set	0.05
KalSVXZWindow	set	4.0
KalSVXPVz1	set	5
KalSVXPVz2	set	1.6
KalSVXCleanUpPhi	set	true
KalSVXCleanUpZ	set	false
KalSVXSigmaPhiWindow	set	6.0
KalSVXSigmaZWindow	set	6.0
KalSVXSigmaStereoWindow	set	6.0
KalSVXWindowIncrease	set	1.25
KalSVXHitLayerFraction1	set	80
KalSVXHitLayerFraction2	set	60
KalSVXHitLayerFraction3	set	40
KalSVXDeltaPhiSection	set	$\pi/20$

tcl-switches of the SiliconForwardTracker

The tuning switches of the Silicon Forward strategy are presented below.

KalFWDVerboseLevel	set	0
UseZ90InKalFWD	set	true
UseAllHitsInKalForward	set	false
MinimumFWDpt	set	0.8
MaximumFWDpt	set	500.0
KalFWDMinPhiHits	set	4
KalFWDMaxChi2pdof	set	20.0
KalFWDPhiWindow	set	0.05
KalFWDZWindow	set	4.0
KalFWDPVz1	set	5
KalFWDCleanUpPhi	set	true
KalFWDCleanUpZ	set	false
KalFWDSigmaPhiWindow	set	6.0
KalFWDSigmaZWindow	set	6.0
KalFWDSigmaStereoWindow	set	6.0
KalFWDWindowIncrease	set	1.25
KalFWDHitLayerFraction1	set	60
KalFWDHitLayerFraction2	set	40
KalFWDHitLayerFraction3	set	20
KalFWDDeltaPhiSection	set	$\pi/20$

System

These switches limits the maximum required system resources, both for in memory space and computing time.

UseTimeoutKludgeInKal	set	true
KalLimitCpuTime	set	false
KalMaxCpuTime	set	900.0
KalLimitRealTime	set	false
KalMaxRealTime	set	900.0
KalLimitMemory	set	false
KalMaxMemory	set	500.0

Bibliography

- [1] *The European Physical Journal G, Nuclear and Particle Physics*
- [2] A.Pukhov, E.Boos, M.Dubinin, V.Edneral, V.Ilyin, D.Kovalenko, A.Kryukov, V.Savrin, S.Shichanin, and A.Semenov.
CompHEP - a package for evaluation of Feynman diagrams and integration over multi-particle phase space. User's manual for version 33.
Preprint INP MSU 98-41/542, hep-ph/9908288
- [3] C. Lecci *A Neural Jet Charge Tagger for the Measurement of the $B_s^0 - \bar{B}_s^0$ Oscillation Frequency at CDF*
PhD thesis IEKP-KA/2005-13, University of Karlsruhe
- [4] CDF Collaboration,
CDF II Technical Design Report,
FERMILAB-PUB-96/390-E, Nov 1996, 318pp,
<http://www-cdf.fnal.gov/upgrades/tdr/tdr.html>
- [5] F. Abe *et al.* (CDF Collaboration),
Evidence for Top Production in $p\bar{p}$ Collisions at $\sqrt{s}=1.8$ TeV,
Phys. Rev. Lett. 73, 225 (1994)
- [6] T. Affolder *et al.* (CDF Collaboration),
Measurement of the Top Quark Mass with the Collider Detector at Fermilab,
FERMILAB-PUB-00/127-E
- [7] T. Affolder *et al.* (CDF Collaboration),
Measurement of the W Boson Mass with the Collider Detector at Fermilab,
FERMILAB-PUB-00/127-E
- [8] D. Acosta *et al.* (CDF Collaboration),
Measurement of B-meson lifetimes using fully reconstructed B decays produced in $p\bar{p}$ collisions at $\sqrt{s} = 1.8$ TeV,
Phys. Rev. D 65, 092009 (2002)
- [9] Fermilab Beam Division,
Run II Handbook
<http://www-bd.fnal.gov/runII/index.html>

BIBLIOGRAPHY

- [10] P. H. Garbincius,
Tevatron collider operations and plans,
hep-ex/0406013
- [11] Official Webpage of the Accelerator Division
<http://www-bdnew.fnal.gov/pbar/AEMPlots/today/PeakLuminosity.png>
- [12] CDF's official Luminosity Webpage
http://www-cdfonline.fnal.gov/ops/opshelp/stores/kumac/store_tot.gif
- [13] T. Affolder *et al.*, *Nucl. Instr. and Meth. A* **42586** (2004) 249
- [14] D. Bortoletto *et al.*, *Nucl. Instr. and Meth. A* **386** (1997) 87
- [15] A. Sill *et al.*, *Nucl. Instr. and Meth. A* **447** (2000) 1
- [16] L. Balka *et al.*, *Nucl. Instr. and Meth. A* **267** (1988) 272
- [17] S. Bertolucci *et al.*, *Nucl. Instr. and Meth. A* **267** (1988) 301
- [18] F. Abe *et al.*, *Nucl. Instr. and Meth. A* **271** (1988) 387
- [19] G. Apollinari *et al.*,
CDF end plug calorimeter upgrade project Proceedings of the Fourth International Conference on Calorimetry in High Energy Physics La Biodola, Italy (1993)
- [20] Y. Seiya *et al.*, *Nucl. Instr. and Meth. A* **480** (2002) 524
- [21] A. Artikov *et al.*, *Nucl. Instr. and Meth. A* **538** (2005) 358
- [22] M. Albrow
CDF Run II Trigger Table and Dataset plan,
CDF/PHYS/TRIGGER/CDFR/4718
- [23] B. Ashmanskas *et al.*, *Nucl. Instr. and Meth. A* **518** (2004) 532
- [24] G. Gomez-Ceballos *et al.*, *Nucl. Instr. and Meth. A* **518** (2004) 522
- [25] W. Wagner, H. Stadie, T. Arisawa, H. Wenzel and G. Veramendi,
Online monitoring in the CDF II experiment,
FERMILAB-CONF-02-269-E
- [26] B. Stroustrup,
The C++ Programming Language, 3rd Ed, 2003 Addison-Wesley
ISBN 0201889544
- [27] P. Schemitz,
Eine Hard- und Software Umgebung für Physik-Analysen bei CDF II,
PhD thesis IEKP-KA/2003-1, University of Karlsruhe

- [28] J. O. Coplien,
Multi-Paradigm Design for C++,
ISBN 0-201-82467-1
- [29] The TrackingKal package in the CDF Run II software
<http://cdfkits.fnal.gov/CdfCode/source/TrackingKal/>
- [30] *The CDF Run II Event Data Model Page*,
<http://www-cdf.fnal.gov/upgrades/computing/projects/edm/edm.html>
- [31] K. Bloom,
Getting Started with CDF Run 2 Offline, 2004
CDF/DOC/COMP_UPG/CDFR/5294
- [32] M. Feindt, S. Menzemer, K. Rinnert,
TrackingKal - A Tracking and Alignment Software Package for the CDFII Silicon Detector, 2003
CDF/DOC/TRACKING/PUBLIC/5968
- [33] P. S. Maybeck,
Stochastic Models, Estimation, and Control,
Vol. 1
- [34] G. Lutz
Semiconductor Radiation Detectors
Springer, Berlin, Heidelberg, New York, London, Paris 1999
- [35] P. Avery,
Applied Fitting Theory V. Track Fitting using the Kalman Filter
1992, CBX 92-39
- [36] J.P.Fernandez, L. Flores Castillo, D. Stuart,
ISL alignment
CDF/PHYS/TRACKING/PUBLIC/7371
- [37] T.Sjöstrand, S.Mrenna, O.Skands
The complete PYTHIA 6.400 manual
FERMILAB-PUB-06-052-CD-T, hep-ph/0603175
- [38] R.Brun, R. Hagelberg, M.Hansroul and J.C. Lassalle
GEANT: Simulation program for particle physics experiments.
User guide and reference manual
CERN-DD-78-2-REV
- [39] P. Gatti,
Performance of the new tracking system at CDF II,
CDF/THESIS/TRACKING/PUBLIC/5561

BIBLIOGRAPHY

- [40] N. Bachetta, et al.,
Results of the KEK Beam Test of SVX II Protoype Detectors,
CDF/DOC/TACKING/PUBLIC/3547
- [41] H. Wenzel,
Tracking in the SVX,
CDF/DOC/SEC_VXT/PUBLIC/1790
- [42] R. E. Kalman,
A new appraoch to linear filtering and prediction problems
Transaction of the ASME-Journal of Basic Engineering,
82 (Series D):35-45, 1960
- [43] S. Menzemer,
Track Reconstruction of CDFII Silicon Detector, 2003
CDF/THESIS/TRACKING/PUBLIC/5968
- [44] The SiliconGeometry package in the CDF Run II software
<http://cdfkits.fnal.gov/CdfCode/source/SiliconGeometry/>
- [45] K. Rinnert,
A Fast-Access Material Map for the SVXII/ISL Silicon Tracking Volume at CDF 2, **CDF/DOC/TRACKING/CDFR/5846**
- [46] K. Rinnert,
A highly efficient geometry model for track reconstruction in the Silicon Vertex Detector at CDF II,
PhD thesis IEKP-KA/2005-5, University of Karlsruhe
- [47] P. Azzi, G. Busetto, P. Gatti, A. Ribon,
Histogram Tracking in the COT,
CDF/DOC/TACKING/CDFR/5562
- [48] C. Hays, P. Tamburello, A. Kotwal, P.Wittich and R. Snider,
The COT Pattern Recognition Algorithm and Offline Code
2004, **CDF/DOC/TRACKING/CDFR/6992**
- [49] A. Mukherjee,
CTC and VTX Tracking,
CDF/ANAL/TRACKING/PUBLIC/5490
- [50] W.-M. Yao, K. Bloom,
"Outside-In" Silicon Tracking at CDF
CDF/TRACKING/DOC/CDFR/CDF5591
- [51] C. Hays, S. Menzemer, K. Rinnert, C. Lecci, M. Herndon and R. Snider,
Inside-out Tracking at CDF, 2004
NIMA 42855 Vol 538/1-3 pp 249-254

- [52] C. Lecci, S. Menzemer, K. Rinnert, M. Feindt,
Pre-Tracking PVz Finder,
CDF/DOC/TRACKING/PUBLIC/5988
- [53] B.Cooper, M.D'Onofrio, B.Heinemann, P.Murat,
Z-Vertex Finder,2004
/CDF/DOC/TRACKING/CDFR/7227
- [54] J.-F. Arguin, B. Heinemann, A. Yagil,
The z-Vertex Algorithm in Run II,2002
/CDF/ANAL/TRACKING/CDFR/6238
- [55] D. Saltzberg, M.Shochet,
Run-II Trigger Table and Datasets Plan
/CDF/PHYS/TRIGGER/CDFR/4718
- [56] B. Knuteson, M. Shochet,
Datasets and Raw Datastreams for Run II
/CDF/DOC/TRIGGER/CDFR/5565
- [57] D. Hare, E. Halkiadakis, T. Spreitzer,
Electron ID Efficiency and Scale Factors for Winter 2007 Analyses
/CDF/DOC/ELECTRON/CDFR/8614
- [58] C.Issever, B.Wagner, A.Robson, C. Mills,
Plug Electron Baseline Cuts
/CDF/DOC/ELECTRON/CDFR/6789
- [59] U. Grundler, L. Lovas, A. Taffard
High-Pt muons recommended cuts and efficiencies for Winter 2007
/CDF/ANAL/TOP/CDFR/8618
- [60] T. Nelson, R. Snider, D. Stuart,
Forward Electron Tracking with the Phoenix-Mods Package
/CDF/DOC/TRACKING/PUBLIC/6278

Acknowledgements

This thesis would not have been possible without the advice, help and support of many people. It is impossible to name them all and those who are not mentioned are not forgotten.

- I wish to sincerely thank my supervisor Prof. Dr. Michael Feindt for offering me both guidance and freedom in my work throughout the time I spent at the *Institut für Experimentelle Kernphysik*.
- I would also like to thank Prof. Dr. Günter Quast for co-supervising this thesis.
- I thank Dr. Stephanie Menzemer and Dr. Kurt Rinnert for introducing me to the track reconstruction software packages and for the many fruitful discussions and their support.
- I am also deeply indebted to the tracking conveners Prof. Dr. Matthew Herndon and Prof. Dr. Rainer Wallny for their support and help.
- I would also like to thank Joachim Heuser, Dr. Yves Kemp, Dr. Dominic Hirschbühl, Dr. Marcel Stanitzki and Dr. Thomas Kuhr for carefully reading parts of this manuscript.
- Special thanks to my office mates Dr. Christian Haag, Dr. Ulrich Kerzel and Michael Milnik for the nice time we had sharing an office and the the encouraging atmosphere.
- I would like to express my gratitude to the admins for keeping the computer cluster running at all times. Special thanks to Dr. Levin Jungermann, Dr. Yves Kemp and Dr. Marcel Stanitzki for the great experience during the software porting to 64bit.
- I would also like to thank my colleagues at the *Institut für Experimentelle Kernphysik* in Karlsruhe and the members of the CDF Collaboration in Chicago for the nice time we had.
- This work was supported by scholarships of the Land of Baden-Württemberg and the “Graduiertenkolleg Hochenergiephysik und Teilchenastrophysik”. I thank them for my scholarship.
- Finally I wish to thank my family for their love and support over all the years.

